Firn Properties Relevant to Passive Microwave Remote Sensing

Lora S. Koenig

A dissertation
submitted in partial fulfillment of the
requirements for the degree of

Doctor of Philosophy

University of Washington

2008

Program Authorized to Offer Degree:
Department of Earth and Space Sciences

University of Washington
Graduate School

This is to certify that I have examined this copy of a doctoral dissertation by

Lora S. Koenig

and have found that it is complete and satisfactory in all respects,
and that any and all revisions required by the final
examining committee have been made.

Chair of the Supervisory Committee:

_____
Eric Steig

Reading Committee:

_____
Eric Steig

_____
Mary Albert

_____
Dale Winebrenner

Date: _____

In presenting this dissertation in partial fulfillment of the requirements for the doctoral degree at the University of Washington, I agree that the Library shall make its copies freely available for inspection. I further agree that extensive copying of the dissertation is allowable only for scholarly purposes, consistent with "fair use" as prescribed in the U.S. Copyright Law. Requests for copying or reproduction of this dissertation may be referred to ProQuest Information and Learning, 300 North Zeeb Road, Ann Arbor, MI 48106-1346, 1-800-521-0600, or to the author.

Signature _____

Date _____

University of Washington

Abstract

Firn Properties Relevant to Passive Microwave Remote Sensing

Lora S. Koenig

Chair of the Supervisory Committee:
Professor Eric Steig
Department of Earth and Space Sciences

Passive microwave remote sensing has the capabilities to monitor changes in firn properties and firn temperature from 1978 to today. The relatively long time series of information from passive microwave sensors and their abilities to penetrate polar darkness and cloud cover make them premier candidates for monitoring climate on the ice sheets. Passive microwave remote sensing is limited, however, because the interaction of the microwave emission with firn microstructure is poorly understood. This study furthers passive microwave remote sensing by investigating relevant firn properties and exploring the use of the extinction-diffusion time model for microwave emission. The time scale of this model, the extinction diffusion time, is shown to vary with accumulation rate in West Antarctica. The extinction-diffusion time is comprised of the microwave extinction length and the thermal diffusivity of the firn. Field measurements were taken of both, microwave extinction length and thermal diffusivities at sites in Greenland and Antarctica with different accumulation rates. Extinction length measurements were taken using radiometers and radars operating near 37 GHz. Measured extinction lengths are shown to be less sensitive to grain size

changes than modeled extinction lengths from strong fluctuation theory. Thermal diffusivities were calculated by taking measurements of thermal conductivity, density and temperature. Thermal diffusivity is shown to decrease with increased accumulation at 3 dry-snow-zone field sites as the extinction-diffusion time predicts. Additional extinction length data is needed to confirm the relationship between extinction length and accumulation rate but initial estimates suggest and increase in extinction length with increased accumulation. Field measured values of the extinction-diffusion time are larger in magnitude than the satellite modeled extinction-diffusion times but the measured values follow a similar trend and simulate emission well. Variations in the extinction-diffusion time appears to be driven by changes in extinction length when extinction length is short and driven by changes in both thermal diffusivity and extinction length when extinction length is long and thermal diffusivity is low. The extinction-diffusion time model is an improved model for microwave emission and appears to be a viable tool for monitoring accumulation rate in the specific ice sheets regions.

TABLE OF CONTENTS

LIST OF FIGURES

LIST OF TABLES

ACKNOWLEDGEMENTS

So many people contributed to my academic journey. First and foremost I have to thank my family, Joel, Mom, Dad and Jeff. You have been with me since the beginning with encouragement and support. To Joel, especially, for his understanding and patients during our time apart.

Special thanks to my advisor and committee. To Eric Steig my advisor, who always let me explore ideas as well as the world around me. To Mary Albert, for sharing her expertise and data, teaching me new techniques, and her wisdom. To Dale Winebrenner, for spending time teaching and helping me through the physics. To Tom Grenfell, for teaching me to use radiometers and trusting me with his instruments. To Cecilia Bitz, for her support and encouragement.

Science is a collaborative effort, and I have many people to thank who have answered questioned, reviewed work and helped generate ideas. I want to thank Rick Forster for always being there to answer questions from my masters to my PhD. Thanks to Prasad Gogineni and all the people at CReSIS for the use of their radar and training as well as HP Marshall for his insights to FMCW radars. Thanks to Zoe Courville for all her help and data. Also I want to thank Koni Steffen for teaching me solid field techniques and allowing me to visit Swiss Camp.

I have to thank the NASA Jenkins' Predoctoral Fellowship program for their funding and for making every fellow feel unique and appreciated. Dr. Jenkins will

always be an inspiration to me and I hope to pass on her spirit to the next generation of explorers.

I want to thank all the graduate students at the University of Washington, especially my officemates, Wendy, Guy, Sanjoy, Wes, Twila, and Scooter, and my colleagues in the glaciology group, especially Joe, Ginny, Michelle, Twit, Al and Ed. Joe Mac deserves special thanks for understanding, support and always knowing the correct Matlab command.

And last but not least all my peeps from the field. Some froze in pits with me while others would just make me laugh at the end of the day. Special thanks to Joe Flaherty for experiencing the great white South with me, couldn't have made it without ya, the domino effect is in effect. Here is the long list of all those who helped and supported me in the field, a very big thank you: Joe, Kevin, Justin, Jay, Koni, Luey, Robin, Lance, Steve, Jake, Robin, Mr. Mike, Dan, Paul, Gordon, Steve, Dan, Brian, Rick, Josh, Kathy, Peter, Bob, Steve, Bella, Cathy, Ginny, Tom, everyone at Raytheon and Veco and the 109th guys, who know how to fly.

DEDICATION

To my family, especially Joel

Chapter 1

INTRODUCTION

1.1 Motivation and Background

Global climate monitoring is especially important today when policy makers require information on how warming temperatures will affect the Earth's biological, ecological, hydrological and cyrospheric systems. Scientists need to provide accurate climate data, so that policy decisions made on the basis of global warming projections are grounded as much as possible in reality.

1.1.1 Climate change

The Intergovernmental Panel on Climate Change (IPCC) reports global warming of 0.7° C in the past 100 years with an addition projected temperature increase of 1.8 to 4° C in the next 100 years [*IPCC*, 2007]. The expression of this warming on the ice sheets of Greenland and Antarctica will contribute to raising global sea level but the rate at which this will occur remains an open question. Greenland and Antarctica both hold massive stores of ice, equivalent to 7.3 and 56.6 meters of sea level rise respectively, if they were to melt completely. Current observational estimates show that both ice sheets contribute 0.55 to 1.82 mm of sea level rise per decade [*IPCC*, 2007], but these numbers are highly uncertain. The uncertainties arise from two primary areas: ice sheet models are currently unable to capture observed acceleration in outlet glaciers, and observational data of key climate

controls on ice sheet mass balance, for example temperature and precipitation, are not adequately constraining these models. This dissertation aims to contribute to the quality of observational climate data over ice sheets.

1.1.2 Ground-based observations of climate over polar ice sheets

Ground-based sources of climate data on ice sheets, including ice cores, ice penetrating radar, and weather stations, are largely incomplete due to spatial and temporal limitations. Ice cores provide the longest records of ice sheet temperature and accumulation, yet they only exist at a few point locations and are subject to significant uncertainties. Ice cores records of accumulation, coupled with ice penetrating radar surveys, can be used to interpolate accumulation data between point locations, providing better spatial coverage. Climate-monitoring weather stations on ice sheets, including automatic weather stations and accumulation stake measurements, are also spatially sparse and temporally short. As a consequence, there is significant disagreement among different studies as to the sign and spatial distribution of accumulation and temperature trends, particularly in Antarctica [*King*, 1994; *Doran, et al.*, 2002; *Vaughan, et al.*, 2003; *van den Broeke and van Lipzig*, 2004; *Schneider*, 2005; *Monaghan et al.*, 2005; *Monaghan et al.,*2006; *Monaghan et al.*, 2008; *Chapman and Walsh*, 2007].

1.1.3 Satellite monitoring of climate

Space-borne satellites sensors are the leading tools for monitoring large scale climate variables with spatial and temporal consistency. Over ice sheets, satellite

sensors collect spatially distributed data of temperature, surface height, snow properties and melt [*Bindschadler*, 1998]. Infrared satellites sensors have been used for 26 years to monitor the spatial and temporal trends in the Arctic and Antarctic climates [*Comiso*, 2000; 2003]. Passive microwave sensors, which started recording emission continuously in 1978, provide a leading tool for retrieving spatially extensive records of firn properties and climate over the ice sheets.

Passive microwave sensors, such as the Scanning Multichannel Microwave Radiometer (SMMR), the Special Sensor Microwave/Imager (SSM/I), and the Advanced Microwave Scanning Radiometer (AMSR-E), have been used in numerous ice sheet studies. Natural passive microwave emission is suited for polar studies because it operates independently of solar illumination and the long-wavelength emission is essentially unaffected by the dry polar atmosphere.

Previous passive microwave studies have used radiative transfer theory to monitor snow-grain growth, temperature changes and accumulation rates over ice sheets [*Zwally*, 1977; *Matzler*, 1987; *Shuman and Alley*, 1993; *Zwally and Giovinetto*, 1995; *Shuman and Stearns*, 2001; *Shuman and Comiso*, 2002]. Temperature-dependant radiation is emitted from deep within the firn in the microwave part of the spectrum. As the radiation travels towards the satellite sensor it is both scattered and absorbed. The extent to which microwave emission is scattered or absorbed contains information about the material the radiation is traveling through. In polar firn, the

amount of the emitted radiation that is scattered or absorbed contains information about firn properties, such as temperature, grain-size, water content and density.

1.2 Statement of research problem and goals

Analysis of passive microwave emission has the potential to provide important information on firn properties, because, depending on the frequency used, it is emitted over a significant range of depths within the firn. For example, the effective depth over which 37 GHz emission occurs is about one meter. Lower frequencies can be used to look deeper into the firn, potentially providing climate information further into the past. Complete understanding of passive microwave signals from firn, however, remains elusive due to the complex relationships among firn physical properties and microwave absorption and scattering. Valuable decadal or multi-decadal-length climate information can potentially be gleaned from the wealth of existing satellite data, if the relationships between relevant firn properties, temperature, and extinction length can be better quantified.

The goal of this work is to increase our ability to monitor climate over ice sheets using space-borne passive microwave sensors. Specifically, this work provides an improved understanding of the relationship among microwave extinction length, thermal diffusivity of firn, and snow accumulation rate at a single microwave frequency. Emphasis is placed on field measurements of microwave extinction length and firn physical properties, including thermal conductivity and microstructure.

1.3 Outline of dissertation

This dissertation serves two purposes: to investigate the relationship between firn properties and passive microwave remote sensing and to provide additional, detailed firn microstructure data that can be used in future studies. Chapter 2 and 3 in this dissertation are written as stand alone articles. Chapter 2 was published in the *Journal of Geophysical Research-Earth Surface* and establishes a link between a passive microwave model parameter and accumulation rate. Chapter 3 is prepared for submission to the *Journal of Geophysical Research-Earth Surface* and presents microwave extinction length measurements and modeling work. Chapter 4 presents radar profile data collected in Greenland and Antarctica and Chapter 5 presents field thermal conductivity measurements gathered during this research. Chapter 6 updates ideas presented in the published Chapter 2 with additional field data. Appendix A-C present the firn microstructure information gathered in this research. These data will be useful to numerous other applications in glaciology, such as remote sensing studies that require grain size measurements and studies on near surface firn processes with implications for ice core analysis.

1.4 Synopsis

Chapter 2 presents a new model for microwave emission from polar firn, and compares the results with observations of accumulation rate in Antarctica. The time scale of this model, referred to as the extinction-diffusion time, is shown to vary

linearly with accumulation rate over a large portion of West Antarctica. Physically the extinction-diffusion time is the microwave extinction length of the firn squared divided by the thermal diffusivity of the firn. The link between accumulation rate, thermal diffusivity and extinction length motivates the following chapters which gather measurements of relevant parameters at field sites. Chapter 3 develops methodologies for taking microwave extinction length measurements near 37 GHz using both a radiometer and a radar at Swiss Camp and Summit, Greenland. Additionally Chapter 3 compares the measured extinction lengths to modeled extinction lengths from a strong fluctuation theory (SFT) model, and shows that the model performs poorly given the field-measured grain sizes. Chapter 4 presents a method to determine extinction lengths from very-high-frequency radar profile data. This estimation method is compared to the direct measurements presented in Chapter 3 at Summit, Greenland. Chapter 5 focuses on measurements of the thermal diffusivity in the top meter of firn at sites with different accumulation rates, contributing significantly to the small existing data base of thermal conductivity from ice sheets. Chapter 6 revisits questions posed in Chapter 2 by calculating field-measured extinction-diffusion times at field sites with varying accumulation. Chapter 6 gives field data that does not contradict findings in the published Chapter 2 that microwave extinction length and firn thermal diffusivity are linked to accumulation. Chapter 7 summarizes the dissertation work and recommends future work from questions raised by the results of this research.

Chapter 2

A LINK BETWEEN MICROWAVE EXTINCTION LENGTH, FIRN THERMAL DIFFUSIVITY AND ACCUMULATION RATE IN WEST ANTARCTICA

This chapter was published under the same title in Journal of Geophysical Research-Earth Surface112(F3) with co-authors Eric J. Steig, Dale P. Winebrenner and Christopher Shuman. The specific contributions of the co-authors were: Eric J Steig had the idea to investigate changes in the extinction-diffusion time in the West Antarctic Region. Dale Winebrenner developed the microwave brightness temperature modeled and guided my use of the model. Christopher Shuman provided passive microwave data for the investigation.

2.1 Summary

The relationship between time-series of physical surface temperature and microwave brightness temperature of polar firn depends both on the physical properties of the firn and the surface temperature history. In perennially dry firn, this relationship is well characterized by a timescale, referred to as the extinction-diffusion time, which is the ratio of the microwave extinction length squared, adjusted for the incident angle of the satellite, to the firn thermal diffusivity. The extinction-diffusion time is calculated over Antarctica from 1982 to 1999 by comparing thermal infrared observations of physical surface temperature from the Advanced Very High Resolution Radiometer (AVHRR) with passive microwave brightness temperatures

measured by the Scanning Multichannel Microwave Radiometer (SMMR) and Special Sensor Microwave Imager (SSM/I). Independent estimates of accumulation rate are derived from both ice cores and spatially extensive ground and airborne radar echo sounding lines. The extinction-diffusion time is found to vary linearly with accumulation rate from approximately 10 to 50 cm/yr ice equivalent over a large area in West Antarctica. Although this simple relationship does not appear to hold at very low or very high accumulation rates, these results suggest that the extinction-diffusion time holds promise as a viable proxy for accumulation rate variability on polar ice sheets. Additional regions where the extinction-diffusion time is a viable proxy for accumulation rate may be identified with a better understanding of the firn properties controlling microwave emission.

2.2 Introduction

Polar-orbiting satellites provide the leading tool for monitoring the Antarctic and Greenland ice sheets. Satellite sensors collect spatially distributed data sets that can be used to derive temperature, surface height, surface velocity, snow properties and melt on ice sheets [*Bindschadler*, 1998]. Snow accumulation rate measurements are of particular interest on ice sheets, both for studies of polar climate variability and for assessments of ice sheet mass balance. Ground-based measurements of accumulation from snow pits, firn cores and AWS sites, though numerous, are sporadic in space and time [*Vaughan et al.*, 1999]. Satellite based measurements of

accumulation rate can be derived from laser altimetry data, after correction for firn densification and ice dynamics. These altimetry data, although very precise, are limited by short operation time. Broad ice sheet coverage by laser altimetry with sub-annual resolution started in 2003 [*Shuman et al*., 2006]. In contrast to ground-based measurements and altimetry data, space-borne passive microwave sensors provide data that are spatially and temporally extensive with operations since 1978 covering both the Greenland and Antarctic ice sheets. The length and continuity of these data give considerable motivation for developing techniques for determining accumulation from passive microwave sensors.

Satellite data from passive microwave emission are well-suited for polar studies in the dry snow zone. Emission at frequencies of 37 GHz and lower are unaffected by the dry polar atmosphere. As discussed in numerous texts (e.g., *Hall and Martinec,* 1985), microwave emission in firn emerges over some characteristic depth, or extinction length. Typical microwave extinction lengths in perennially dry polar firn range from fractions of a meter to tens of meters, depending on frequency. The microwave emission observed from space is most sensitive to firn properties at depths less than the extinction length. The importance of the firn properties to the passive microwave signal increases non-linearly towards the snow-air interface. Relevant firn properties include temperature, grain size, density, layering and grain shape [*Hall*, 1987; *Mätzler*, 1987; *Surdyk*, 2002; *Zwally*, 1977]. Because these same

firn properties are sensitive to accumulation rate changes, it is expected that there will be some relationship between passive microwave emission and accumulation rate. Previous attempts to relate microwave emission to accumulation rate have relied on estimates of an effective emissivity or the polarization of emission from polar firn [*Vaughan et al*., 1999; *Winebrenner et al.*, 2001; *Zwally and Giovinetto*, 1995; *Zwally*, 1977]. These efforts have suffered from various problems including poor correlation with the available ground-based accumulation rate.

In this paper, we revisit the relationship between accumulation rate and microwave emission using a more complete model of firn emission properties, following *Winebrenner et al.* [2004]. The model simulates passive microwave emission over dry-snow regions on ice sheets by solving the radiative transfer equation, neglecting the multiple scattering term, while using surface temperatures to force the heat diffusion equation, which establishes a temperature profile in the firn and supplies the needed temperature in the radiative transfer equation. We take advantage of infrared satellite data to provide an independent estimate of the surface temperature forcing covering the entire ice sheet. The surface temperature forcing is used in the *Winebrenner et al.* [2004] model (see Background) to simulate microwave brightness temperatures, which are compared to observed microwave brightness temperatures. Using both observed and calculated microwave brightness temperature and observed surface temperature forcing provides a means to directly calculate the ratio of the microwave extinction length squared, adjusted for the satellite incident

angle, to the firn thermal diffusivity. Spatial variations in this ratio are found to vary linearly with variations in accumulation rates over a large region of West Antarctica, and over a broad range of values (10 to 50 cm/yr ice equivalent).

2.3Background

Thermal microwave emission from dry firn consists of contributions from a range of depths below the surface [*Zwally*, 1977]. Emitted intensity, therefore, depends on the vertical temperature profile in the ice sheet over that range as well as the firn characteristics. The vertical temperature profile is determined by past surface temperature forcing [*Paterson*, 1994]. An observation of the microwave brightness temperature at any given moment thus depends not only on the surface temperature at that moment, but also on past surface temperature forcing as well as the thermal and microwave extinction properties of the firn [*Winebrenner et al*., 2004].

If surface temperature, *T(t)*, remained constant at some value, $\overline{T}$, for long enough to make the firn isothermal over the entire depth range pertinent to microwave emission, then the brightness temperature, $T_B(t)$, would also be constant in time at some value $\overline{T}_B$. $\overline{T}_B$ would then relate to the firn temperature as

$$\overline{T}_B = \varepsilon \overline{T}, \qquad (2.1)$$

where ε is the emissivity. In equation 2.1 the assumption is made that the Rayleigh-Jeans approximation holds for microwave frequencies and ice-sheet temperatures.

Equation 2.1 remains valid when $\overline{T}$ and $\overline{T}_B$ are long-term means of the time-varying surface and brightness temperatures, provided that the mean of the temperature profile in the firn is constant with depth. For annual averages, equation 2.1 closely approximates microwave observations [*Zwally*, 1977]. On shorter time scales, *Shuman et al.* [1995; 2001; 2002] and *Surdyk* [2002] showed that surface and brightness temperature means over periods approximately a month or longer can be related by a modified version of equation 2.1:

$$\overline{T}_B(t) = \varepsilon(t)\overline{T}(t). \qquad (2.2)$$

In equation 2.2, $\overline{T}(t)$ and $\overline{T}_B(t)$ are means on approximately monthly or longer time scales. The emissivity, $\varepsilon(t)$, is allowed to vary in time to account for the changing contributions to emission from various depths as the temperature profile changes during the year.

Equation 2.2 fails to accurately approximate means over time scales shorter than the time needed for surface temperature forcing to propagate to all depths that contribute to observed emission. In fact, strictly speaking, no instantaneous relationship such as equation 2.2 can explain emission at time t in terms of a surface temperature at time t alone. The instantaneous relationship must fail because temperature profiles cannot respond instantaneously to changes at the surface [*Paterson*, 1994]. Rather, emission at the present time, t, must depend on the physical memory at depth of past surface temperatures and on the weighting of emission contributions from those depths. After modest simplifying assumptions, the result is

a weighted sum over surface temperature forcing, or a convolution [*Winebrenner* et al., 2004, equation 9]:

$$T_B(t) = \varepsilon\overline{T} + \varepsilon\int_0^{\frac{t}{\tau_0}} T_f(t-\tau_0\tau')G(\tau')d\tau', \qquad (2.3)$$

where $\overline{T}$ is the long-term (annual or longer) mean of surface temperature, ε is the time invariant emissivity defined by equation 2.1, $T_f(t)=T(t)-\overline{T}$ is the fluctuating part of the surface temperature, G is the convolution kernel:

$$G(\tau') = \frac{1}{\sqrt{\pi\tau'}} - \exp(\tau')\mathrm{erfc}(\sqrt{\tau'}), \qquad (2.4)$$

erfc is the complimentary error function, and τ_0 is the characteristic time-scale of averaging over past surface temperature variations. τ_0 is referred to as the extinction-diffusion time:

$$\tau_0 = \frac{L_\theta^{\,2}}{K} \qquad (2.5)$$

where K is the thermal diffusivity of firn at depths commensurate with L_θ, the extinction length adjusted for the satellite incident angle (also called the penetration depth) defined as:

$$L_\theta = \frac{\cos\theta}{k_e} \qquad (2.6)$$

where θ is the angle of transmission of the electromagnetic wave in the snow, using Snell's law, given the satellite incident angle from Nadir and k_e is the total extinction coefficient.

Spatial and temporal variation in the extinction-diffusion time is expected to correlate with changes in firn properties that control firn thermal diffusivity and the microwave extinction length. Thermal diffusivity is controlled by changes in thermal conductivity and density, while extinction length in dry snow is controlled by changes in grain size, layering, and density. *Courville et al.* [2007] took measurements of thermal conductivity in a megadunes region near Vostok, East Antarctica, and show a decrease in thermal conductivity with increased accumulation at sites with very low accumulation rates. Extinction length should also to be correlated with accumulation due to the influence of density and grain size variations [*Surdyk*, 2002]. Snow grains at lower accumulation sites sit at the snow-air interface for longer periods of time relative to high accumulation sites. The low accumulation snow grains are exposed to larger temperature gradients at the snow-air interface, leading to constructive metamorphosis and hence larger snow grains. In general, extinction length will decrease as snow grain size increases; thus, extinction length should increase with accumulation rate. We therefore expect the extinction-diffusion time (the ratio of extinction length squared adjusted for the incident angle of the satellite and the thermal diffusivity) to increase with accumulation rate.

2.4 Data and Methods

To investigate changes in the extinction-diffusion time (τ_0) over space and time, we compare simulated passive microwave data with observed passive

microwave data. The simulated data are calculated using equation 2.3 and surface temperature time series data sets discussed further below. The Defense Meteorological Satellite Program (DMSP) data sets from the Scanning Multichannel Microwave Radiometer (SMMR) and the Special Sensor Microwave Imager (SSM/I) provide the observed passive microwave (T_B) measurements on daily and monthly scales [*Gloerson et al., 1990; Maslanik and Stroeve*, 1990]. We use T_B's from both the 18/19 and 37 GHz vertically polarized channels, abbreviated 19V and 37V respectively, because they provide the longest record of consistently acquired data and are less affected by surface roughness than horizontally polarized channels. While we have chosen to use the long time series provided by the SMMR and SMM/I datasets for this work, it is noted that the Advanced Microwave Scanning Radiometer (AMSR-E) dataset can work equally well.

Two surface temperature (T_S) data sets were used as model inputs: near-surface (~1 m-screen height) Automatic Weather Station (AWS) data from the Antarctic AWS Project [*University of Wisconsin*, http://uwamrc.ssec.wisc.edu/aws.html] and thermal infrared surface skin-temperature observations from the Advanced Very High Resolution Radiometer (AVHRR) [*Comiso*, 2000]. These two complimentary data sets were used because AWS time series provides daily resolution, but only at isolated points, whereas the AVHRR data provides broad spatial coverage, but with reduced temperature fidelity. AWS data were used only if there were two or more consecutive years of data with no more than

two consecutive missing days; the mean value of adjacent days was used to fill missing days. AVHRR temperatures provide spatially distributed T_S data on monthly time scales from 1982 to 1999 [*Comiso*, 2000]. The AVHRR data are monthly averaged because surface measurements are valid only on cloud free days. There were no missing monthly data points but not all months are comprised of the same number of daily observations. The 5 by 5 km AVHRR surface temperatures were re-sampled to the 25 by 25 km SSM/I grid, for comparison with the microwave T_B data.

To determine the extinction-diffusion time, τ_0, the surface-temperature data are used to simulate passive microwave brightness temperature data for a large range of τ_0 values (see equation 2.3). The τ_0 value is determined by optimizing the fit between simulated and observed T_B. The best fit is defined as the single minimum of the squared residuals between the fractional variation in the observed and simulated T_B's, following *Winebrenner et al.* [2004]. Figure 2.1 shows the fit curve for τ_0 on the left and the daily fractional variation of AWS simulated T_B's compared to the satellite observed T_B's on the right, for four representative locations over several years. Plots similar to Figure 2.1 can be derived at any AWS site with two or more consecutive years of data in the dry snow zone. Uncertainty in the estimate of τ_0 is calculated by adding normally distributed random noise to the satellite T_B time series with a standard deviation of 2 K, based on the SSM/I sensor sensitivity [*Hollinger, et al.*, 1990].

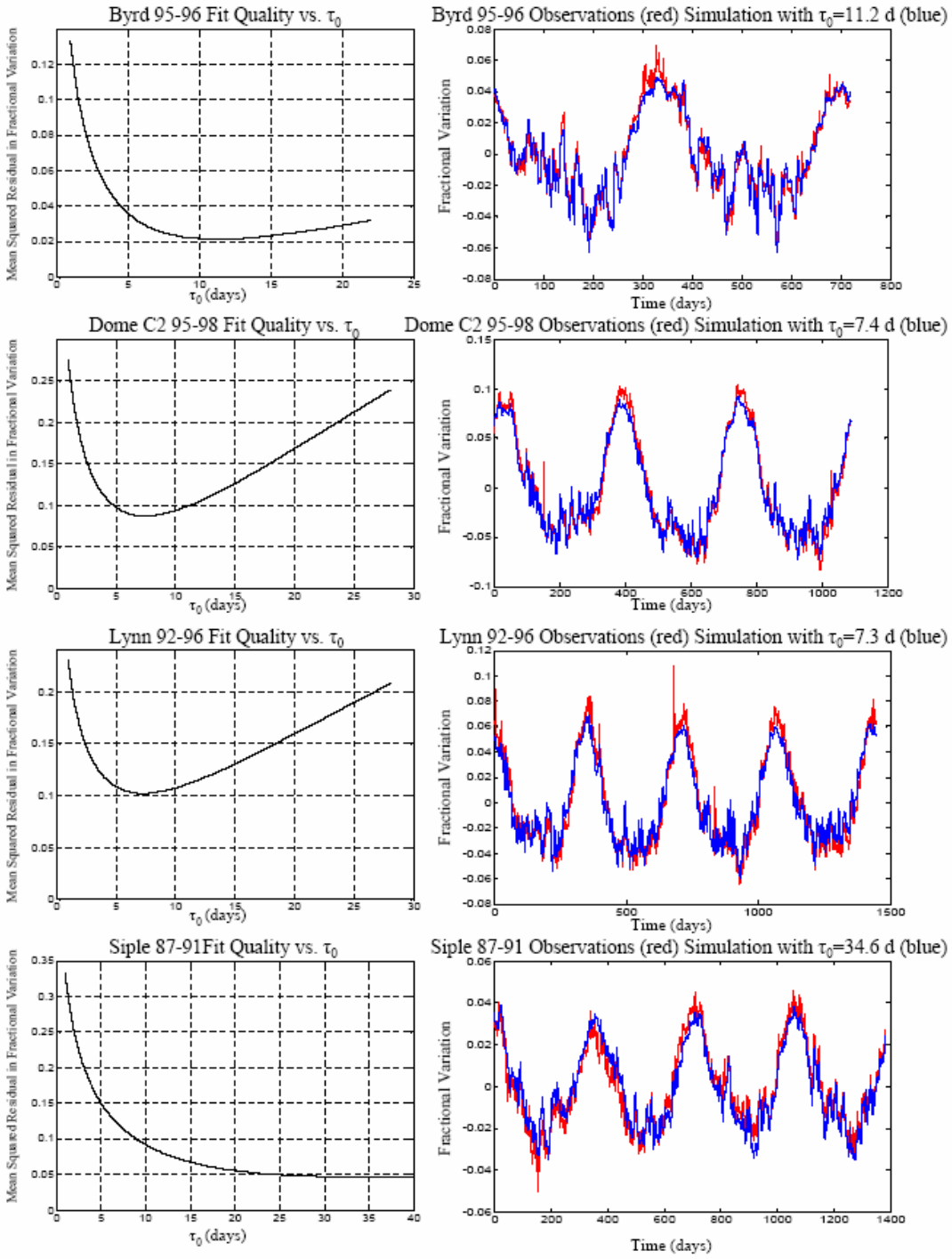

Figure 2.1 Plots of root-mean-square-difference (RMSD) with simulated and observed brightness temperature.(left column) Plots of the RMSD between simulated

and observed time-series of the fractional variation in brightness temperature, versus the value of the extinction-diffusion time-scale, τ_0, used for simulation, at 4 AWS sites. (Fractional variation in a brightness temperature, $T_B(t)$, is defined as $[T_B(t)-\overline{T}]/\overline{T}$, where $\overline{T}$ is the long-term mean value of $T_B(t)$.) Values of τ_0 at which the rmsd is minimized are defined as the best-fit values. (right column) Simulated (blue) and observed (red) fractional variations in vertically polarized, 37 GHz brightness temperatures for SSM/I pixels containing the 4 AWS sites, for the best-fit value of τ_0 at that site as indicated by the plot in the left column. Note the range in values of best-fit τ_0 and the agreement between simulations and data on times scales ranging from years to a few days. The 4 AWS sites represent a wide variety of Antarctic conditions. (Dome C isa low accumulation site in East Antarctica; Lynn is in a katabatic wind region near the ice sheet edge; Siple is in a high accumulation area near the base of the Antarctic Peninsula ; and Byrd is near an ice sheet divide in West Antarctica.) Locations of AWS sites are shown in Figure 2.2.

Typical error values are +/- 1 day.

Best-fit values of τ_0 were calculated from both daily AWS and monthly mean IR T_S data. Daily averaged T_B's were used to determine τ_0 in pixels with AWS stations while monthly averaged T_B's were used to determine τ_0 at pixels with AVHRR data. At pixels where both AWS and AVHRR data are available, there is little discrepancy. Table 2.1 compares the best-fit τ_0 calculated from the longest AWS time series available at representative sites to the best-fit τ_0 calculated from the AVHRR data set from 1982 to 1999. Directly comparing the τ_0's calculated from AWS data and AVHRR data over simultaneous time periods is difficult because the AWS data are sporadic; however, as shown in Table 2.1, at most sites the AWS τ_0's are comparable to the AVHRR τ_0's.

Point source measurements limit accuracy when looking at spatial phenomena, like temperature and accumulation, so we use the AVHRR spatial fields to look at variations in τ_0 over space. The monthly AVHRR T_S data set was used to simulate monthly averaged T_B's over all of Antarctica (equation 2.3). The simulated T_B's were then compared to the monthly averaged SMMR or SSM/I T_B data sets to best-fit τ_0's over the dry snow zone of Antarctica (Figure 2.2).

The spatial τ_0 fields were compared to accumulation measurements. We compiled accumulation data sets from ice-penetrating radar and shallow ice cores. Point source accumulation rates were derived from 14 shallow ice cores obtained by

Table 2.1 Comparison of best fit τ_0 derived from AWS and AVHRR surface temperature data. The locations of the AWS stations is shown in Figure 2.2.

Station	AWS T_S Dates	τ_0 AWS (months)	AVHRR T_S Dates	τ_0 AVHRR (months)
Byrd	1981-88	.56	1982-99	.53
Dome C	1984-95	.51	1982-99	.60
Dome C II	1995-98	.25	1982-99	.31
Siple	1987-91	1.15	1982-99	.88

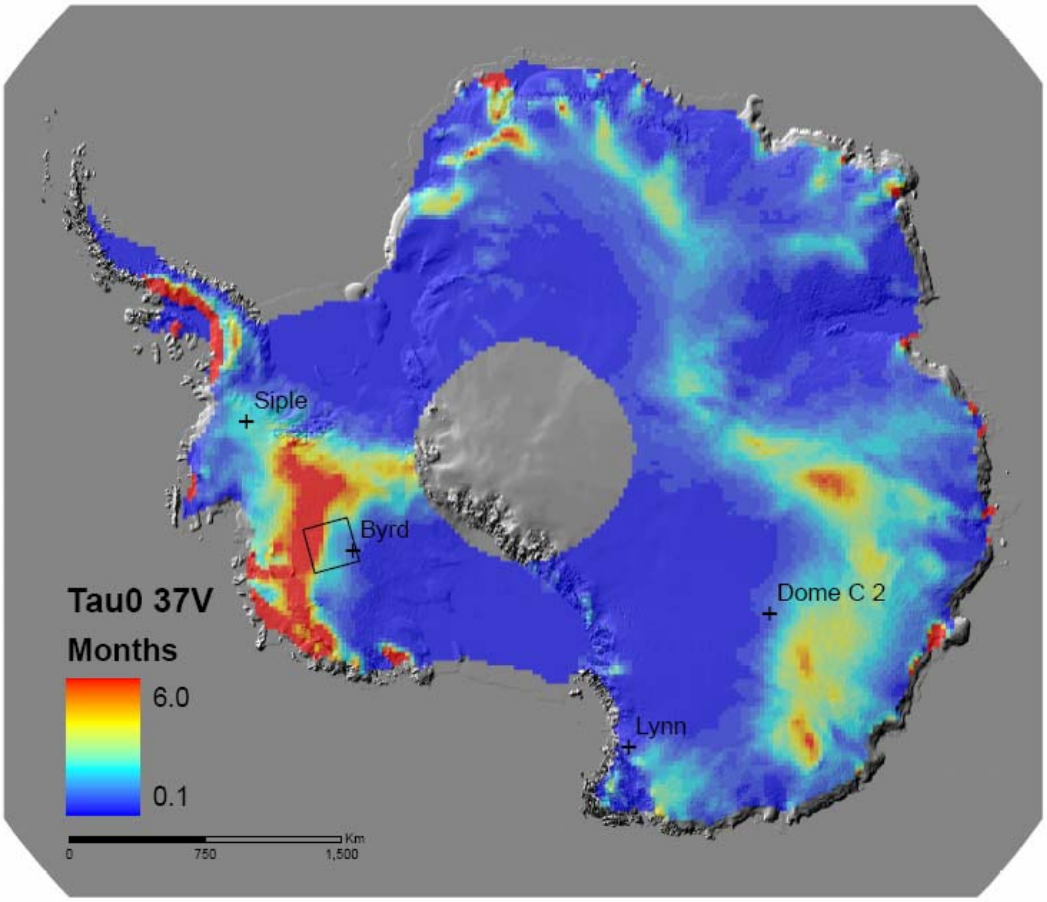

Figure 2.2 Spatial variability in best-fit values of τ_0 on the Antarctic continent as observed using SSMR/SSM/I, excluding areas that melt seasonally. τ_0 is calculated using the entire time series from 1982 to 1999. Variability in East Antarctica appears to be associated with ice divides, and does not obviously correspond with known variability in accumulation rates. Variability near the West Antarctic Divide, however, does correspond with known accumulation rate variability. The box shows the location of the radar generated accumulation dataset used in Figures 2.4 and 2.5. + denotes locations of AWS stations.

the US ITASE program [*Kaspari et al*., 2004]. A spatial grid of accumulation rates was generated from numerous ice-penetrating radar flights near Byrd Station, Antarctica [*Morse et al.*, 2002]. Accumulation rate was determined from the depth of continuous radar horizons that intersected the Byrd ice core. The radar-based accumulation rates represent an average over the past 2500 years; the depth penetrated far exceeds the expected extinction length of passive microwave sensors, but this data set is the best spatial estimate of accumulation patterns currently available. An additional accumulation data set is derived from a single ground-based radar transect between US ITASE shallow ice cores [*Spikes et al.*, 2004]. The US ITASE radar-based accumulation data represent an average from 1966 to 2000.

Spatial variations in τ_0 and comparison to accumulation were calculated using both 19V and 37V passive microwave brightness temperatures. The results at each frequency are nearly identical, so we show only the 37 GHz results here.

2.5 Results and Discussion

The extinction-diffusion time, τ_0, varies spatially and temporally. Figure 2.2 shows calculated τ_0 for Antarctica at all pixels north of 85°S (the limit of SMMR coverage), using the AVHRR surface temperature data to simulate microwave data that were compared to the SMMR/SSM/I 37V microwave data, from 1982-1999, with those pixels removed where surface melting may be significant [*Schneider and Steig*, 2002; *Schneider et al*., 2004]. To examine temporal variability, the 37 V τ_0 was

calculated from the AVHRR time series broken into six three-year sections. Figure 2.3 shows the six anomaly maps produced by subtracting each three-year τ_0 estimate from the 1982 to 1999 τ_0 estimate. We note that the mean of the six three-year τ_0's is nearly identical to the eighteen-year (1982-1999) τ_0 at all pixels across Antarctica. The precision of the τ_0 estimates is thus fairly insensitive to the length of the record used to calculate it.

Over the whole of Antarctica, no single relationship between τ_0 and accumulation would be expected on evidence of Figure 2.2; rather, the spatial pattern of τ_0 correlates with ice divides and perhaps other topographic features. Still, for a large region near Byrd Station in West Antarctica, a strong relationship is evident. A subsection of the 37V τ_0 map near Byrd Station, extending to both sides of the main West Antarctic ice divide, was extracted to compare with radar-generated accumulation rates (Figure 2.4) and US ITASE ice-core accumulation rates (Figure 2.5). The results show a strong linear relationship between τ_0 and accumulation rate (Figure 2.6) for both the radar data and the ice core data, up to accumulation rates of about 50 cm/yr ice equivalent. Three of the ITASE cores, located towards the Antarctic Peninsula, and having generally higher accumulation rates, appear as outliers. The outliers are not entirely surprising because of the differences in climate between the West Antarctic divide and the three ice core sites. The different regional climates produce different firn structures and fabrics that correspond to changes in

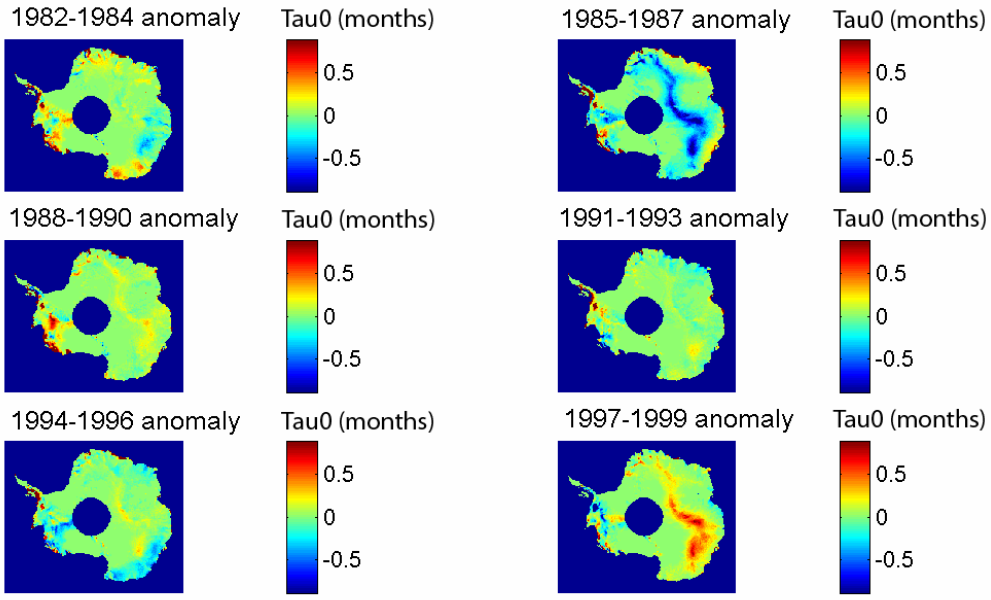

Figure 2.3 Temporal variability in best-fit values of τ_0, as estimated from 3-year blocks of observations. The means of 3-year values of τ_0 agree with τ_0 values inferred from the full 18-year data set taken as a whole.

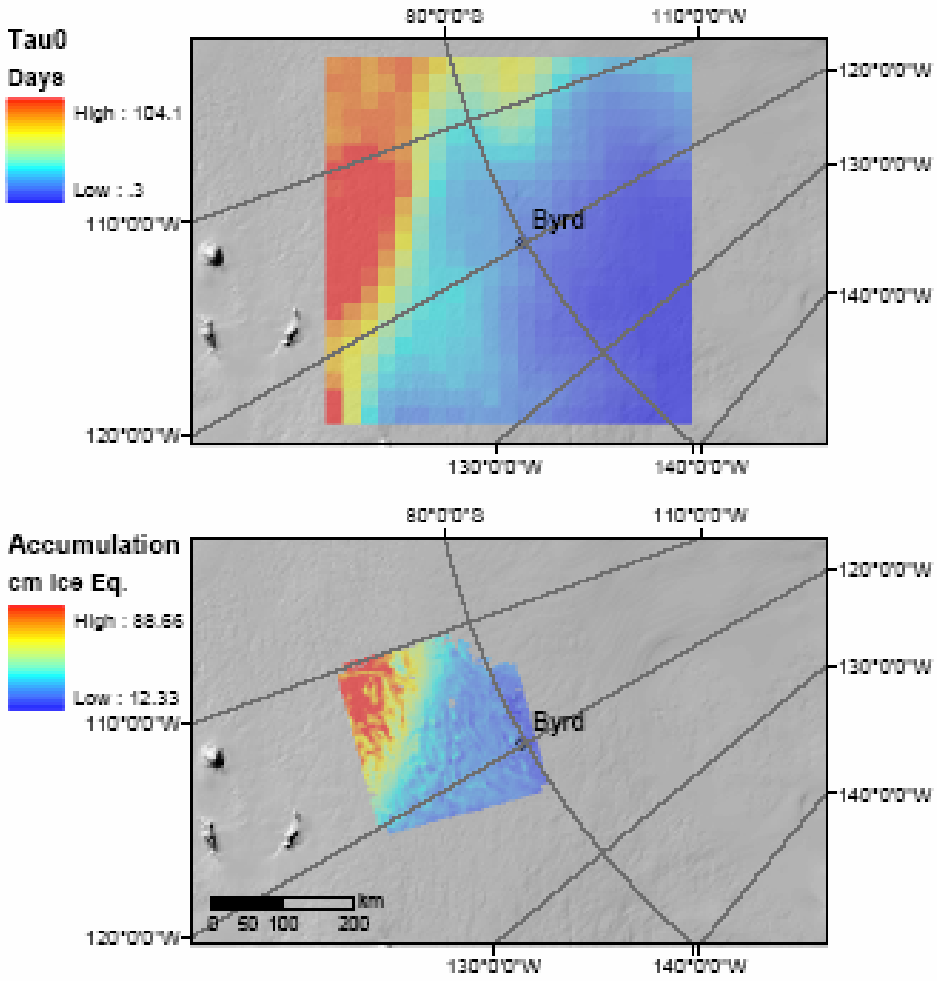

Figure 2.4 (top) Map of the extinction-diffusion time-scale, τ_0, near Byrd Station. (bottom) Map of millennial-time-scale accumulation rate near Byrd Station [*Morse et al.*, 2002] derived from depth variations of ice-core dated layers observed in airborne ice-penetrating radar data.

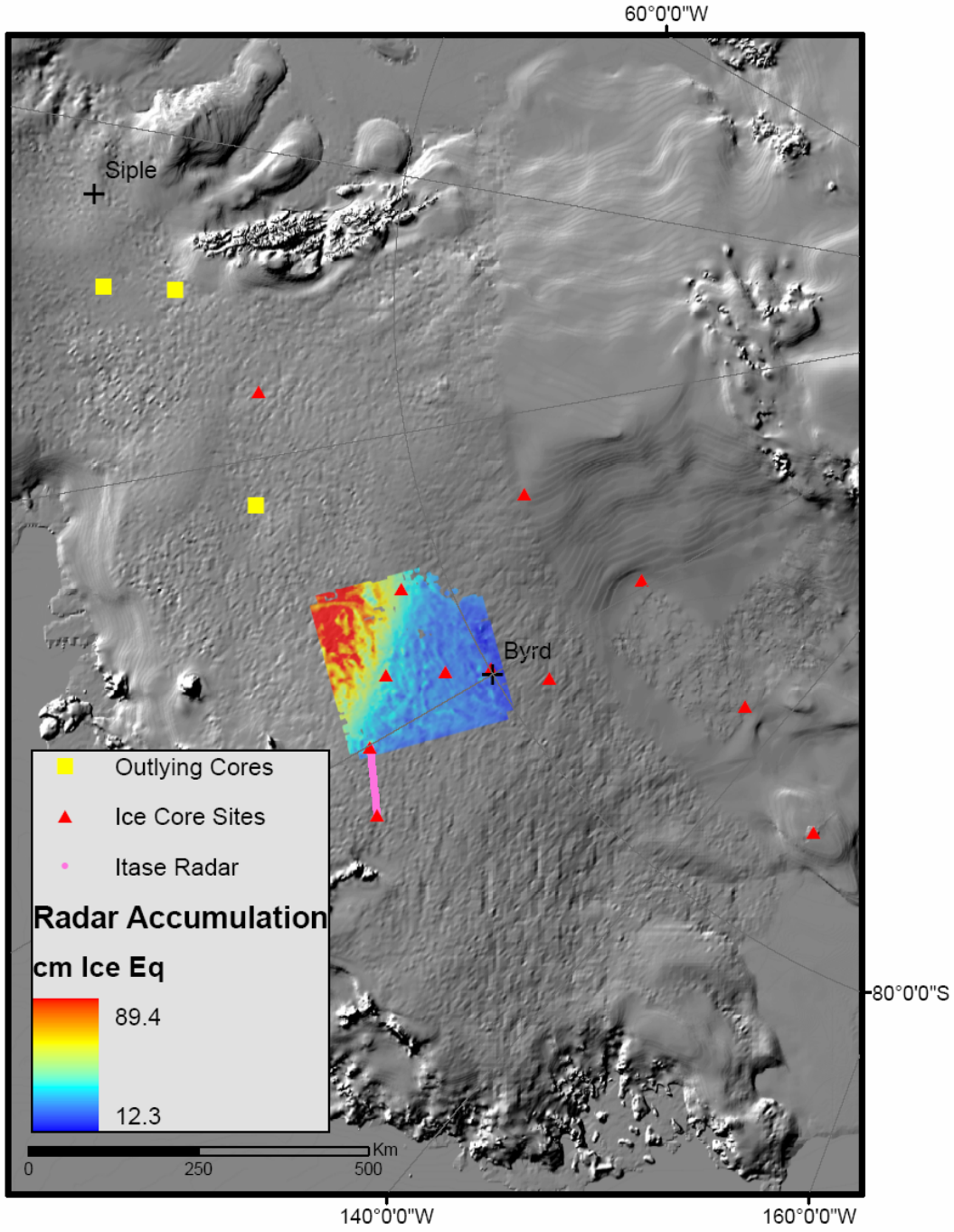

Figure 2.5 Locations of ice-core- and radar- derived accumulation rate data. Ice-core-derived accumulation data are averages over periods of decades to centuries. Cores with data that agree with the accumulation-rate/τ_0 relationship derived from radar data are shown in red, whereas cores which disagree are shown in yellow.

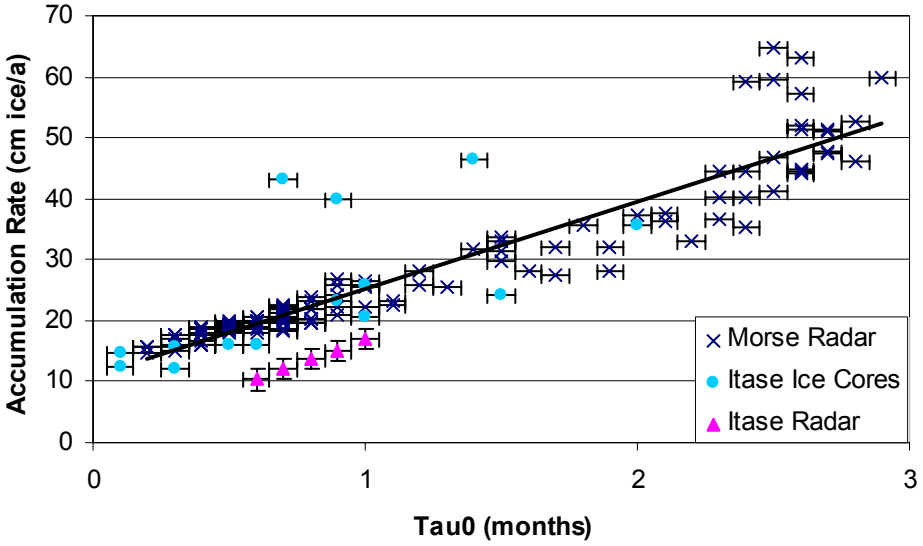

Figure 2.6 Observed correlation between accumulation rates derived from radar layers and ice cores and the extinction-diffusion time, τ_0, for the region near Byrd Station, extending across the West Antarctic Divide. The ITASE radar line, which appears slightly lower than the other data, is probably explained by the temporal difference in the averages. The Morse radar is averaged over the past 2500 years while the ITASE radar is averaged over the past 34 years.

microwave extinction length and thermal diffusivity, suggesting the possibility of different relationships between τ_0 and accumulation of different snow facies. Nevertheless, the linear correlation for the rest of the data suggests that τ_0 could be used to estimate accumulation rates in specific geographic areas.

The observed correlation between τ_0 and accumulation rate near Byrd could be driven by changes in thermal diffusivity, in extinction length, or both, as described in the Background material, above. Without additional field measurements of extinction length over the region, we cannot distinguish whether changes in thermal diffusivity or extinction length dominate changes in τ_0. We can, however, use independently modeled extinction length and existing field thermal conductivity measurements, to determine whether variations in τ_0 are consistent with existing data and theory.

2.6 Sensitivity analysis

A few field measurements of thermal diffusivity provide an independent check on our calculations of τ_0. *Courville et al.* [2007] obtained thermal conductivity and density measurements at two sites in East Antarctica, one with "high" accumulation (4.1 cm weq/yr) and the second with "low" accumulation site (3.0 cm weq/yr). The thermal conductivity and density data at each site were used to calculate the thermal diffusivity. At these two sites the thermal diffusivity decreased from the low accumulation site to the high accumulation site, consistent with the observed relationship between accumulation and τ_0. Given the field thermal diffusivity

measurements and τ_0, equation 2.5 was used to determine the expected extinction lengths at 37 GHz of 0.27±0.03 cm and 0.31±0.03 m for the low and high accumulation sites respectively. These results are very similar to *Surdyk's* [2002] modeled extinction lengths of 0.2-0.3 m at 37 GHz for similar firn conditions, suggesting that τ_0 can be used to determine extinction lengths.

Clearly, the relationship between τ_0 and accumulation is more complicated than the linear relationship near Byrd Station. Preliminary investigation of accumulation rates in East Antarctica suggests that for the very lowest accumulation rates, the τ_0-accumulation relationship is more highly scattered than observed in our West Antarctic test region. We note, though, that accumulation data for East Antarctica are often sparser and very difficult to measure. The linear relationship also appears to fail for the highest accumulation rates, as observed in the "outlier" cores noted in Figure 2.5 and the increased scatter in the data in Figure 2.6 at accumulation rates greater than 50 cm/yr ice equivalent. It is likely that when accumulation rates cross this threshold, the extinction length is shallow compared to the annual accumulation, and snow properties become increasingly independent of accumulation rate. It is also likely that the amount of time, however short or long, the firn spends near the surface prior to burial will have some control on extinction length.

Finally, it is interesting to consider whether the temporal changes in τ_0, apparent in Figure 2.3, might be used to estimate temporal accumulation rate changes for those areas where the linear relationship appears to hold. While the strong

variability observed in East Antarctica is not readily explained in terms of accumulation rate, the variations observed in West Antarctica are at least suggestive of the observed accumulation rate variability. Notably, the largest recent El Niño events occurred in 1982/1983 and 1997/1998, corresponding to the three-year period with the greatest positive and negative τ_0 anomalies in West Antarctica. *Bromwich and Rogers* [2001] have noted previously that the West Antarctic accumulation-rate response to El Niño in these years was of opposite sign.

2.7 Conclusions

This work relates surface temperature to satellite brightness temperature through a convolution equation dependent on a characteristic time scale, the extinction-diffusion time, τ_0. This relationship describes how surface temperature changes that occurred in the past, still recorded in the firn, influence current brightness temperatures. τ_0 is dependent upon firn microstructure controlling the microwave extinction length and thermal conductivity.

The extinction-diffusion time varies in space and time over Antarctica. Near Byrd Station, Antarctica, where excellent ground-based accumulation rate data exist, τ_0 is linearly related to accumulation over a broad range from approximately 10 to 50 cm/yr ice equivalent. In East Antarctica, τ_0 is not simply related to accumulation rate, suggesting a more complex relationship between firn properties and accumulation rate, deserving of further investigation. Nevertheless, these results suggest the extinction-

diffusion time may be useful for deriving accumulation rate over specific large geographic regions on polar ice sheets.

Chapter 3

FIELD MEASUREMENTS OF MICROWAVE EXTINCTION LENGTH NEAR 37 GHZ FROM SUMMIT AND SWISS CAMP, GREENLAND

This chapter is in preparation for submission with co-authors Richard Forster, Thomas Grenfell and Eric J. Steig. The specific contributions of the co-authors were: Richard Forster helped develop field methodologies for the FMCW radar, as well as, provided expect advice on processing radar data. Thomas Grenfell provided the radiometer for this study and the methodology for processing the data. Eric Steig provided field logistics and guidance.

3.1 Summary

Microwave emission from ice sheets is related to both firn temperature and other firn properties, including density and grain size. To better understand the relationship between microwave emission, temperature and firn properties, it is important to know the extinction length of the emission. Here we present a method for collecting field measurements of microwave extinction lengths using a radiometer and a Frequency-Modulated Continuous-Wave (FMCW) radar. The field measurements are fitted with four radiative transfer equations taking into account the firn temperature profile. Our methods provide direct measurements of the microwave extinction length in undisturbed firn. In May and June of 2006, extinction lengths

were measured by radiometer at 5 pits within a 25-km radius of Summit, Greenland with recorded values ranging between 1.5–1.7 m at 37 GHz and at one pit at Swiss Camp, Greenland with an extinction length of 0.9 m at 37 GHz. In June of 2007, an extinction length was measured by FMCW radar at one pit at Summit, Greenland yielding a value of 1.0 m. Measurements are compared to a layered strong fluctuation theory (SFT) model that calculates the dielectric permittivity of the firn. The dielectric permittivity is used to calculate an extinction length. The model underestimates the measured extinction length values and is very sensitive to changes in grain size where as the measurements show negligible scattering at 37 GHz.

3.2 Introduction

In 1978 space-borne passive microwave sensors began gathering consistent records of microwave emission from Greenland and Antarctica, making it one of the longest climatic satellite records over the ice sheets. Microwave emission is related to the firn temperature and firn properties, including density and grain size, to a certain depth in the firn called the extinction length [*Surdyk*, 2002; *Zwally*, 1977]. Because emitted radiation emerges from depth, it can be conceptually illustrated by imagining that the emission samples firn structures in similar fashion to a shallow firn core. Theoretically, then, the microwave signal can be used to extract similar information as a firn/ice core record. The possibility of using the passive microwave signal in a similar fashion to ice cores motivates studies to understand the interactions of the

microwave emission with climate dependant firn structures, including grain size and density, to depth.

Most previous studies used the emissivity of polar firn to model the space-borne microwave brightness temperature and related changes in emissivity to accumulation rate changes [*Arthern, et al.*, 2006; *Winebrenner, et al.*, 2001; *Zwally and Giovinetto*, 1995; *Zwally*, 1977]. This study differs from previous studies in that it is motivated by the extinction-diffusion time model of microwave emission developed by *Winebrenner et al.* [2004]. *Winebrenner et al.* [2004] model microwave emission by using the heat diffusion equation to solve for a temperature profile in firn. This temperature profile is used in the radiative transfer equation in place of a singular daily or averaged temperature. Combining the heat diffusion equation with the radiative transfer equation produces a convolution equation with a characteristic time scale, called the extinction-diffusion time. The time scale is dependant on two physical properties in the firn, the thermal diffusivity of the firn and the microwave extinction length, which is defined as the e-folding depth of the microwave emission.

The extinction-diffusion time is linked to accumulation rate in West Antarctica [*Koenig, et al.*, 2007]. This result is reasonable because extinction length and thermal diffusivity are controlled by firn parameters that change given different accumulation regimes. A control on extinction length is the grain size which is influenced by accumulation rate, the longer the grain sits at the snow/air interface the larger the grain tends to be [*Surdyk*, 2002]. Thermal diffusivity is controlled by thermal conductivity,

density and temperature which also vary with accumulation rate. An investigation into thermal diffusivity changes with firn properties and accumulation rate is given in Chapters 5 and 6.

Investigating links between accumulation rates and extinction length motivated this study to develop a methodology to take field measurements of microwave extinction lengths near 37 GHz simultaneously with firn microstructure information in undisturbed firn. The 37 GHz channel was selected because it is common on space-borne sensors and modeled 37 GHz extinction lengths are similar to typical firn pit depths, approximately 0 to 2 m. Using 37 GHz allows for firn properties and stratigraphy information to be gathered in a simple pit, where as a higher frequency would penetrate beyond a reasonable pit depth requiring more sophisticated field logistics.

Here we describe two techniques for taking field-based extinction length measurements. In the future it is expected that these methods can be used at numerous sites with different accumulation rates. The first method uses a microwave radiometer and the second an FMCW radar. We briefly mention and compare methods for collecting the necessary firn microstructure data relevant to microwave radiation, using both visible measurements in the field and stereological measurements in the lab. Field-based extinction length measurements at Swiss Camp and Summit, Greenland are presented and compared with modeled extinction lengths from strong fluctuation theory (SFT).

3.3 Background

This section gives a brief overview of previous microwave extinction length measurements and extinction length modeling studies at similar frequencies to those used in this study. The extinction length or e-folding depth, L, with units of meters (m) is defined as the inverse of the extinction coefficient (described in more detail in Section 3.5). The extinction coefficient, k_e, has units of inverse meters (m^{-1}). In some previous studies the extinction coefficient is given in units of power loss per meter (dBm^{-1}) denoted N_e. The relationship between the extinction coefficients with different units is given by:

$$N_e = 10\log_{10}(e)k_e \approx 4.34k_e, \qquad (3.1)$$

[*Winebrenner et al.,* 2003].

Surdyk [2002] and *Surdyk and Fily* [1995] used an SFT model to determined extinction lengths given general firn properties, such as temperature, density and grain size, and for specific properties from a pit location. Modeled results show satellite penetration depths ranging from 0.1 to 1.4 m, which is an extinction length of 0.2 to 2.2 m after adjustment for satellite incidence angle of 50°, at 37 GHz over density, temperature and grain size ranges reasonable for polar ice sheets. A site specific extinction length of 0.5 m is given for Wilkes Land, Antarctica; this was the only continental ice sheet measurement at 37 GHz presented in their study. [*Surdyk*, 2002; *Surdyk and Fily*, 1995]. The measurement at Wilkes Land had firn densities of

approximately 370 to 470 kg/m^3, a temperature of -32.8 C and mean grain size of 0.3 mm. Additionally *Surdyk and Fujita* [1995] also used an SFT model to fit resonator data and calculate an extinction length of 1.44 ± 0.15 m for a snow sample with a density of 320 kg/ m^3 and a grain size of less than 0.3 mm.

Hallikainen et al. [1987] took laboratory measurement at a range of microwave frequencies for numerous different dry snow samples with densities ranging from 172 to 380 kg/m^3 and observed mean grain sizes ranging from 0.2 to 1.6 mm. At 35 GHz the extinction lengths ranged from a tiny fraction of a meter, for samples with high density and large grains, to approximately 4 m, for a sample with low density and small grain size. An extinction length of 0.24 m was measured for a snow sample with similar properties to polar firn, density 315 kg/m^3 and grain size 1.0 mm. This study also derived and empirical equation to calculate extinction length from the observed grain size. *Hallikanien et al.* [1987] study gave an additional result showing that the transmission of a wave, determined by the Fresnel power transmission coefficient, at 35 GHz through the air-snow interface is 1 which implies that reflection of the wave at the air-snow interface is negligible.

Rott [1989] and *Rott et al.* [1993] used two different field measurement techniques to calculate extinction lengths. In the first field experiment a radiometer monitored the firn brightness temperature at two sites in Antarctica, Mizuho and Plateau. Recorded brightness temperatures were used with a radiative transfer equation to semi-empirically determine extinction lengths of 1.2 m and 1.4 m for

Mizuho and Plateau, respectively [*Rott,* 1989]. Specific firn microstructure information was not given. The second field experiment measured extinction length by placing cut out firn blocks in front of a radiometer to measure transmittance and then calculating the extinction length from the transmittance [*Rott*, 1993]. This experiment measured extinction lengths at 5.2 and 10.3 GHz, not at 37 GHz. *Grenfell and Lohanick* [1985] used a similar technique measuring the extinction length in sea ice by placing differently sized blocks of ice in front of a radiometer. The change in brightness temperature versus material depth provides the necessary data to fit an extinction coefficient and then calculate an extinction length.

There are two potential faults with using the snow/ice block method when measuring extinction length. The first problem with this method is that snow is heavy to move, therefore the blocks are cut relatively small, 0.3 m, in comparison to the extinction length at 37 GHz, which models place around 1.0 m for common firn structures [*Rott*, 1989; *Surdyk*, 2002]. The second problem is that the smaller blocks are not optically thick and emitted radiation is more easily lost by scattering out the edges of a small block than in a larger block. The loss out the sides of the block should cause the measurements to underestimate the extinction length value. Methods presented here will attempt to eliminate these problems by digging a pit in the firn and placing the radiometer below a large column of firn reducing edge effects.

Cutting and removing firn blocks when measuring extinction length, also disrupts the firn microstructure. At 37 GHz, or a wavelength of 0.81 cm, the snow

grain size approaches the wavelength. Any grain changes introduced by cutting and moving the block, as well as, grain changes from removing the block from its original thermodynamic setting could introduce error in the calculations. The method presented here minimizes errors associated with snow grain changes by leaving the measured firn column intact and only exposing the front face of the column to thermodynamic changes, exposing it for only a few hours to the air temperature.

No previous extinction length measurements of firn were found where a 32 to 40 GHz FMCW radar was used to take the measurements.

3.4 Field methods

Two field methodologies were developed to measure microwave extinction lengths, one utilizes microwave radiometers and the second utilizes microwave radars. Extinction length is measured in relatively undistributed firn, meant to closely simulate what the space-borne sensors record. The goal of the methodology is to obtain brightness temperature measurements for the radiometer and backscattered power measurements for the FMCW radar, from multiple firn thicknesses. The firn thickness to brightness temperature or backscattered power is fitted for an extinction coefficient which determines an extinction length; the specific equations are presented in the section 3.5.1 and 3.5.2.

The first field method uses a 37 GHz passive microwave radiometer. *Grenfell and Lohanick* [1985] provide the technical specification of the radiometer used in this

study. First a two-meter pit is dug with an additional space, or tunnel, dug at the bottom of the pit into the pit wall (Figure 3.1). The radiometer is placed in the tunnel at the bottom of the pit allowing the horn to point skywards through the firn column (Figure 3.2). A firn brightness temperature measurement is taken at angles of 0, 10, 20 and 30 degrees off vertical. The measurement includes emission from the firn above the horn and sky. The emission from the sky is very small compared to the firn. Firn column length is measured, the first measurement is ~1.5 m. (1.5 m was chosen as a starting point because model predictions placed the satellite penetration depth at 37 GHz between 0.1 and 1.4 m [*Surdyk*, 2002]) A 0.1 m block of firn is cut out from the bottom of the firn column and is used as a base to set the radiometer on. This makes the column length 1.4 m and raises the radiometer to minimize multiple scattered radiation from entering the radiometer horns (Figure 3.1).

Another series of brightness temperature measurement is taken with the radiometer measuring the 1.4 m firn column. This process is repeated until the radiometer is looking through a firn column of approximately 0.1 m in length. This method provides multiple brightness temperatures through a firn column ranging from approximately 0.1 to 1.5 m. Sky and ecosorb brightness temperatures (a cold and warm target) are recorded between each firn measurement to calibrate the radiometer.

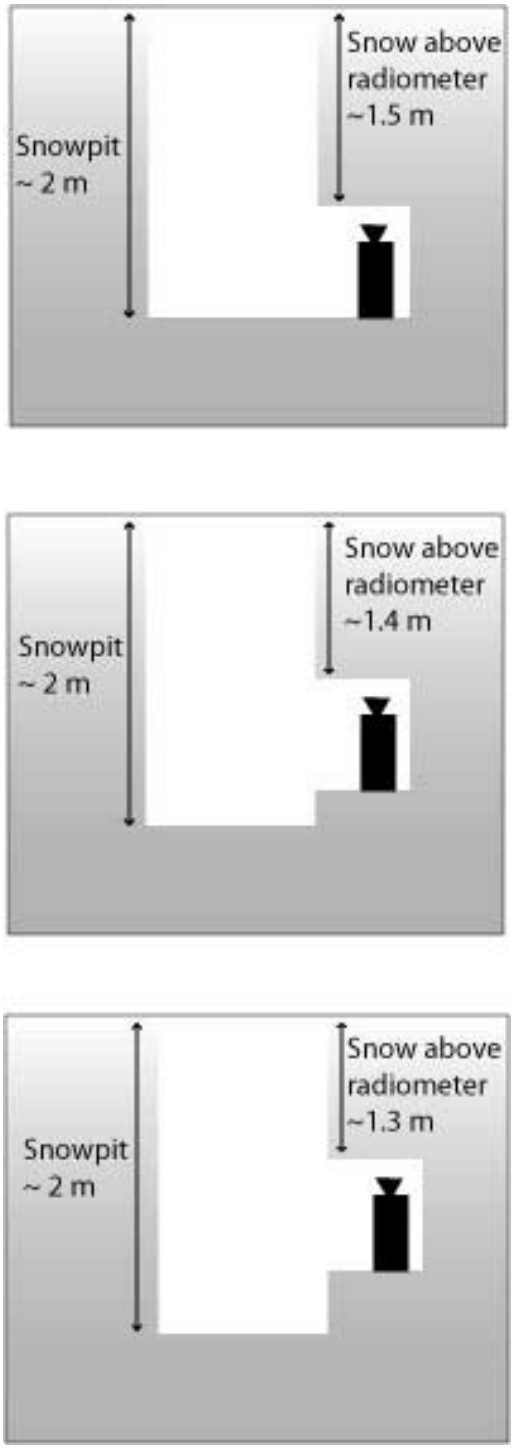

Figure 3.1 Cartoon illustrating three radiometer measurements in a pit. Each measurement records a brightness temperature through different firn thicknesses.

Figure 3.2 Picture of a typical pit with the radiometer positioned to take a measurement of the firn column

The second field method uses a radar that sweeps between 32 and 40 GHz. This radar was built by the Center for Remote Sensing of Ice Sheets (CReSIS) at the University of Kansas and the technical specification of the radar are given by *Legarsky* [1999]. The methodology for the radar is similar to that of the radiometer; designed to leave the firn intact and take measurements at 0.1 m firn increments. The main difference from the radiometer is that a retroreflector must be place below the radar.

The radar is mounted 1 m above the snow surface. A pit is dug below and to the side of the radar (Figure 3.3). A hole is dug into the pit wall directly below the radar. A Luneberg lens reflector, with known radar cross section, is placed below the radar horns. The Luneberg lens returns a stable reflectance over a wide range of radiation incident angles, +/- 30 degrees, making it an ideal retroreflector for field measurements where it is difficult to keep equipment in precise locations. The reflection for the Luneberg lens contrasts that of a metal plate reflector where the angle of incidence has a large effect on the power return to the radar. The Luneberg len's stability over incident angles allows for multiple field measurement to be taken with the assumption of consistent backscatter from multiple locations below the horn. All relative power loss, therefore, is caused by extinction, both absorption and scattering, in the firn and not loss from reflecting the radiation outside of the radar's antenna.

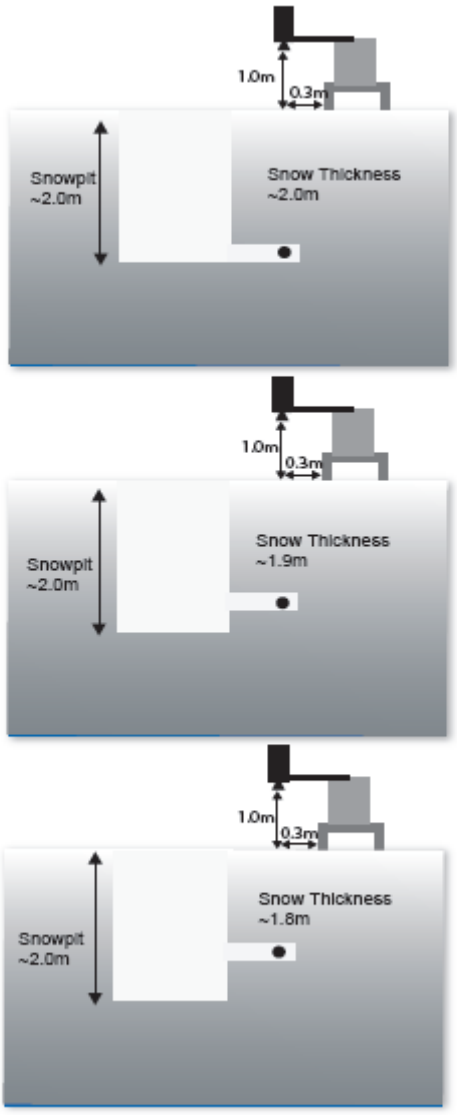

Figure 3.3 Cartoon illustrating how three FMCW radar measurements are taken in a pit. Each measurement gives a power return from the reflector, the Luneberg lens, through a different firn thickness.

It is necessary to obtain backscatter power from the Luneberg lens with different amounts of firn between the reflector and the radar to calculate extinction lengths. A hole is dug in the pit wall at approximately 1.5 m depth (Figure 3.3). The reflecting lens is placed in the hole. The radar is turned on and the lens is moved systematically over the radar footprint multiple times to insure that the peak backscatter is recorded. The antenna beam patterns of the radar has a strong directional dependence requiring movement of the lens to insure the peak backscatter is obtained from the peak location within the antenna beam pattern. The lens is moved to hit the exact center of the footprint thus eliminating any errors introduced from power lost at the sides of the standard gain horns used on the radar. Similar to the radiometer measurements, a 0.1 m block of firn is cut out of the bottom of the firn column. The lens is raised so there is 0.1 m less firn than the previous measurement. This process is repeated until measurements have been taken every 0.1 m from a thickness of approximately 1.5 m to the snow surface.

Sky calibrations are taken at the beginning and end of pit measurements to monitor the radar noise and stability. The sky is considered non-scattering at the frequency the radar operates at, therefore, the signal contained in the sky measurement is the radar's noise signal.

The relevant firn stratigraphy and microstructure data for modeling studies is gathered at each pit coincident with the radiometer and radar data. These data include density thermal conductivity and temperature measurements taken at 0.1 m intervals

and stratigraphy information on major layers which includes grain size and grain shape as determined from a macroscope in the field. Dimethyl phthalate casts of the firn were also collected at certain pits using the methods described by *Perla* [1982]. These casts provide a model of the firn microstructure and a more rigorous quantitative measurement of grain size and density. The firn microstructure data along with the field-based measurements of extinction length provide a complete data set for the construction and testing of microwave radiative transfer and SFT models on ice sheets.

3.5 Extinction length calculations

Extinction lengths are calculated from field measurements and compared with an SFT model. The field measurements are used to determine a firn extinction coefficient (k_e) by fitting a physically based equation (described below in the sections 3.5.1 and 3.5.2) to the measured data of brightness temperature or backscattered power as a function of firn thickness. k_e is related to the extinction length L by:

$$L = \frac{1}{k_e}. \qquad (3.2)$$

This section describes how the radar and radiometer data are processed and fitted to obtain extinction lengths. This section also describes the SFT model used to determine extinction lengths given site specific stratigraphy and firn microstructure.

3.5.1 Radiometer data

In practice the radiometers return a voltage measurement of the natural emission of a material. Brightness temperatures are retrieved by calibrating the radiometer between each measurement with a known warm and cold target. Ecosorb, a near black body material, at a known temperature is used for the warm calibration target while 4 sky measurement taken at angles of 0, 20 40 and 50 degrees off vertical are used for the cold calibration targets. The calibration targets are used to linearly extract brightness temperature measurements from the voltage measurements [*Grenfell and Lohanick*, 1985].

The radiometer measures transmittance of radiation flux through different amounts of firn. The brightness temperature recorded at the radiometer can be described to first order by the radiative transfer equation neglecting the multiple scattering term. Four different derivations of the radiative transfer equation were used to fit the data. The first derivation assumes a constant firn temperature with depth given by:

$$T_B(z) = (1-\sigma_R)^2 T_{B_{sky}} e^{-k_e \frac{z}{\cos\theta}} + (1-\sigma_R)\frac{k_a}{k_e} T_{s\_mean}(1-e^{-k_e \frac{z}{\cos\theta}}) \quad , (3.3)$$

where T_B is the brightness temperature measured at the radiometer looking skywards through a portion of firn, $T_{B_{sky}}$ is the mean brightness temperature of the sky between measurements, T_{s_mean} is the mean or effective thermodynamic temperature of the firn, θ is the angle of the wave traveling in the firn off of vertical and is calculated using

Snell's law, k_e is the total extinction coefficient which includes both scattering and absorption losses, z is the firn thickness and σ_R is the coefficient of surface reflection calculated using Fresnel's equation and is very small, 0.01 for the air-snow interface.

The second derivation of the radiative transfer equation takes into account a linear temperature gradient in the firn and is given by:

$$T_B(z) = (1-\sigma_R)^2 T_{B_{sky}} e^{-k_e \frac{z}{\cos\theta}} + (1-\sigma_R)\frac{k_a}{k_e} T_{surf}(1-e^{-k_e \frac{z}{\cos\theta}}) + (1-\sigma_R)\frac{k_a \cos\theta}{k_e^2}\frac{dT}{dz}[\frac{k_e z}{\cos\theta} - (1-e^{-k_e \frac{z}{\cos\theta}})] \quad , \quad (3.4)$$

where T_{surf} is the thermodynamic temperature at the surface of the firn and $\frac{dT}{dz}$ is the temperature gradient in the firn.

The final two derivation of the radiative transfer equation treat the firn as a layered medium and account for the temperature and temperature gradient across each layer. The third derivation of the radiative transfer equation assumes a constant temperature in each layer of the firn and is given by:

$$T_B(z) = (1-\sigma_R)^2 T_{B_{sky}i} e^{-k_e \frac{z}{\cos\theta}} + (1-\sigma_R)\frac{k_a}{k_e}\sum_{i=1}^{n} T_{si} e^{-k_e \frac{(z_n - z_{i+1})}{\cos\theta}}(1-e^{-k_e \frac{(z_{i+1}-z_i)}{\cos\theta}}) \quad , \quad (3.5)$$

where T_{si} is the thermodynamic temperature at each layer and $T_{B_{sky}i}$ is the sky brightness temperature measured before measuring each layer. The forth derivation takes into account at linear temperature gradient across each layer and is given by:

$$T_B(z) = (1-\sigma_R)^2 T_{B_{sky}i} e^{-k_e \frac{z}{\cos\theta}} + (1-\sigma_R)\frac{k_a}{k_e}\sum_{i=1}^{n} T_{si} e^{-k_e \frac{(z_n - z_{i+1})}{\cos\theta}} (1 - e^{-k_e \frac{(z_{i+1}-z_i)}{\cos\theta}}) + (1-\sigma_R)\frac{k_a \cos\theta}{k_e^2}\sum_{i=1}^{n} \frac{dT}{dz}_i e^{-k_e \frac{(z_n - z_{i+1})}{\cos\theta}} [k_e \frac{(z_{i+1}-z_i)}{\cos\theta} - (1 - e^{-k_e \frac{(z_{i+1}-z_i)}{\cos\theta}})] \quad (3.6)$$

Equations 3.3 through 3.6 are fitted to radiometer data at each pit determining a pit extinction length.

Extinction length is also determined, using equation 3.3, between consecutive pairs of radiometer measurement by solving for $k_e(\Delta z_i)$. This method has been used previously in block experiments [*Rott*, 1993]. Solving for $k_e(\Delta z_i)$ between points introduces more scatter in the extinction length calculation but allows extinction length changes to be assessed at each firn layer and compared to stratigraphy information.

3.5.2 Radar data

FMCW radar processing techniques have been described previously by *Stove* [1992] and for snow studies by *Marshall et al.* [2004]. Here only the essential aspects for using such a radar to determine extinction length are described.

With a reflector place in the firn, the backscattered power (P_T) is a summation of the power from the reflector (P_R) and the power from the internal layers of the firn (P_L) given by:

$$P_T = P_R + P_L . \quad (3.7)$$

Only P_R is needed for extinction length calculations, so P_L is subtracted out of the total power using the coherent noise reduction technique [*Beaven*, 1995]. P_L is measured immediately before the reflector is placed in the pit for each measurement and is considered noise in the case of measuring extinction lengths.

The reflector is placed in the firn and moved horizontally in a grid pattern under the radar antennas in order to hit the maximum power in the antennas beam pattern. Moving the reflector systematically in the beam pattern yields multiple peak returns and attempts to measure the maximum return. The five largest power returns from the reflector are picked and averaged in the extinction length calculation. Averaging the top five peaks reduces errors between different measurements where the exact same point in the beam pattern will most likely not be reached from one measurement to the next. Averaging allows for this error between measurements, where as the single maximum requires that the exact same point in the beam pattern be hit in each measurement, which is unrealistic.

Calculating extinction length using the FMCW radar and a known retroreflector, such as a Luneberg lens, starts with the radar equation, assuming backscattered power return from only the reflector:

$$P_R = \frac{P G^2 \lambda^2 \sigma}{(4\pi)^3 R^4} \tag{3.8}$$

where P is the power transmitted, G is the gain, λ is the wavelength, σ is the scattering cross section and R is the range to a point target. P is unknown in this

case because the radar is not calibrated. The assumption is made that P is constant between measurements, which is reasonable when the radar is temperature stable and the measurements are being made over a short period of time, about 2 hours. The power return from the Luneberg lens placed on the surface of the snow is determined by:

$$P_{surf} = \frac{P G^2 \lambda^2 \sigma}{(4\pi)^3 R_{surf}^4} \tag{3.9}$$

The power returned from the same lens placed some depth z in the firn is given by:

$$P_z = \frac{P G^2 \lambda^2 \sigma}{(4\pi)^3 R_z^4} e^{-k_e 2z}, \tag{3.10}$$

where k_e is the total extinction coefficient of the firn. The exponential term is included in the radar equation to calculate the addition power lost in the firn. P, G, λ and σ remain constant from one measurement to the next and cancel when the power return for the lens at the snow surface is compared to the power return at depth z. Taking the ratio of P_z to P_{surf} gives:

$$P_z R_z^4 = P_{surf} R_{surf}^4 e^{-k_e 2z}, \tag{3.11}$$

which is rewritten to show the change in power return as a function of depth:

$$P_z(z) = \frac{P_{surf} R_{surf}^4 e^{-k_e 2z}}{R_z^4}. \tag{3.12}$$

In this field work the Luneberg lens was operating in the near field of the radar for some of the field measurements. Multiple lab tests were conducted to determine at

what distance the spreading loss of the Luneberg lens in air followed a $1/R^4$ spreading loss that is expected of a point target. Lab tests determined that the Luneberg lens behaved as if it were in the far field at a distance of 1.5 m for the antenna horns, theory defined the far field as 2.5 m from the horns. Based on the lab test, only radar data that was more than 1.5 m from the horns is used to calculate the extinction coefficient. Placing this condition on the radar data eliminated data gathered in the top 0.5 m of firn. In future work the radar mounting device will be extending higher above the snow surface so the lens is operating in the far field for all measurements.

Note that in all equations, both radar and radiometer, k_e is the same, it is the total extinction coefficient of firn and is used to calculate extinction length using equation 3.2.

3.5.3 Extinction length model

The complex relative permittivity, $\varepsilon = \varepsilon' + i\varepsilon''$, is calculated using a strong fluctuation theory model for each layer of firn in a pit given the measured microstructure data. The model was developed by Grenfell (personal communication) and is based on strong fluctuation theory [*Stogryn*, 1986; *Stogryn*, 1974].

The model is driven by inputs of temperature, mean grain size and density at each layer. Because density and temperature information are recorded at equally spaced intervals in a pit, that rarely correspond with firn layers, the weighted average of the raw temperature and density measurements are used to calculate the temperature

and density for each model layer. Extinction coefficients are calculated from the model using the relative permittivity at each layer using:

$$k_e = \frac{4\pi}{\lambda}\sqrt{\varepsilon''} \qquad (3.13)$$

where λ is the wavelength in the medium. Equation 3.13 is a direct result of the solution to Maxwell's equations for a plane wave in an unbounded medium. A weighted average over all the layers was used to calculate ε_{total} for a pit as follows:

$$\varepsilon_{total} = \frac{1}{z_{total}} \sum \varepsilon_{layer} z_{layer} \; . \qquad (3.14)$$

ε_{total} was used to calculate the total pit extinction length using equation 3.13 and extinction length was calculate at individual layers using ε_{layer} .

3.6 Results and Discussion

Measurements were taken at 6 pits near Summit, Greenland and one pit near Swiss Camp, Greenland. Pit locations are shown in Figure 3.4. A radiometer was used at all pits, except Summit 07-1 where an FMCW radar was used.

3.6.1 Radiative transfer model fits

Four radiative transfer equations were derived to fit the radiometer data for an extinction length. The equations have two unknowns k_a and k_e. Previous measurements and model results for k_a on a variety of snow samples gives a range of

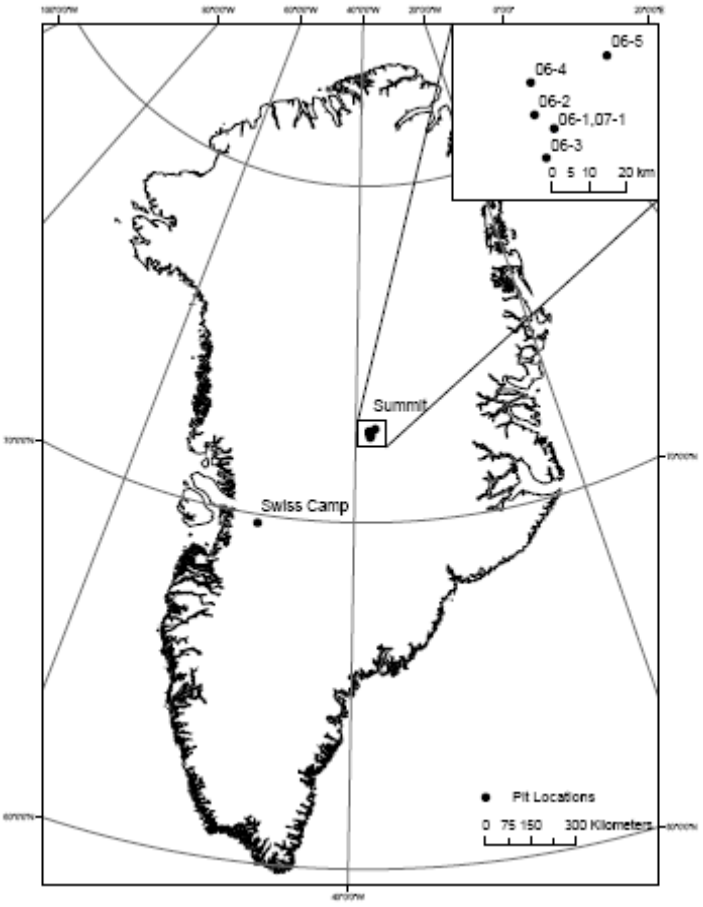

Figure 3.4 Map of pit locations.

values from approximately 0.2 to 0.6 m^{-1} with a few outliers as high as 1.79 m^{-1} [Wiesmann et al., 1998]. The published range was large so the SFT model was used to determine k_a for each pit. k_a can be determined from the SFT model by plotting the value of k_e verses grain size (Figure 3.5). $k_e = k_a + k_s$ where k_s is the scattering coefficient which is dependant on grain size. As grain size decreases, k_s also decreases until the grains are small enough that k_s goes to zero and $k_e = k_a$. This is shown in Figure 3.5. When the slope of the line goes to zero at small grain sizes $k_e = k_a$, thus k_a is determined. The SFT model predicted a k_a value of 0.3 m^{-1} for all Summit pits and 0.4 m-1 for the Swiss Camp pit. Figure 3.6 shows the root mean square error (RMSE) space determined by varying both k_a and k_e and comparing to the measured data to the modeled data from equation 3.3 (equations 3.3 through 3.6 produce almost identical RMSE error spaces so equation 3.3 is used as the representative equation). Figure 3.6 shows that the SFT modeled absorption coefficient of 0.3 m^{-1} lies outside of the RMSE minimum and, therefore, cannot best-fit the measured data.

The range in the measured k_a values and the fact that the SFT modeled values did not best-fit the measured data constituted that the absorption number term (k_a / k_e) in the radiative transfer equations be treated as single ratio varying between 0 and 1. (The absorption number can also be written as 1-α where α is the single-scattering albedo.) The RMSE space of the absorption number to k_e, Figure 3.7, shows the best-

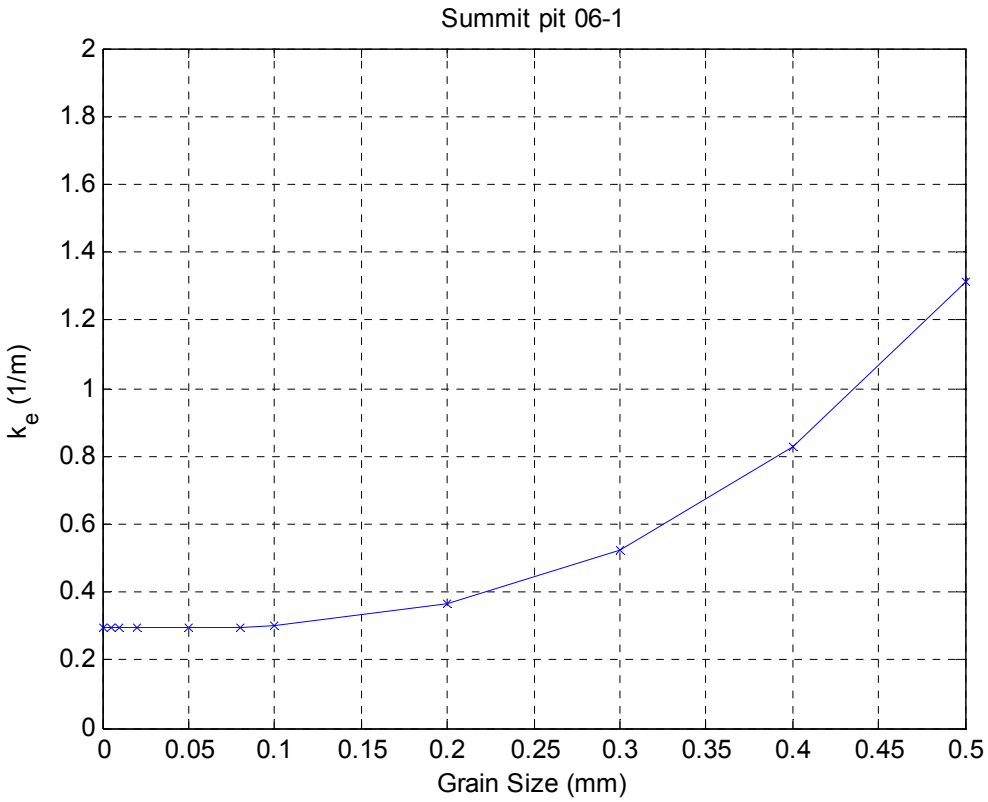

Figure 3.5 Plot of grain size versus extinction coefficient from the SFT model showing that when the slope of the curve goes to zero at small grain sizes the scattering coefficient goes to zero causing the extinction coefficient to equal the absorption coefficient. This plot models the absorption coefficient at 0.3 m^{-1} for Summit pit 06-1.

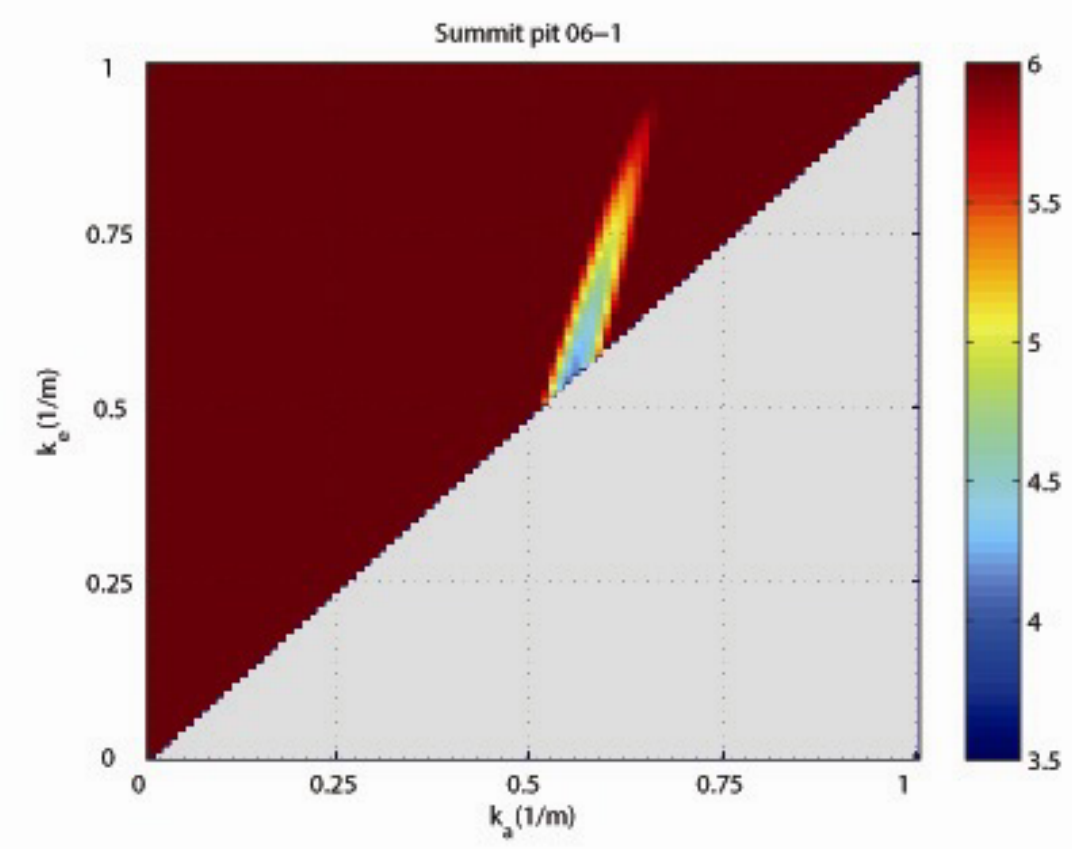

Figure 3.6 Plot of root mean square error (RMSE) space from fitting equation 3.3 to the measured data at Summit pit 06-1 using different values for the extinction and absorption coefficient. The RMSE space shows that the SFT modeled absorption coefficient of 0.3 m^{-1} lies outside of the RMSE minimum and, therefore, cannot best-fit the measured data.

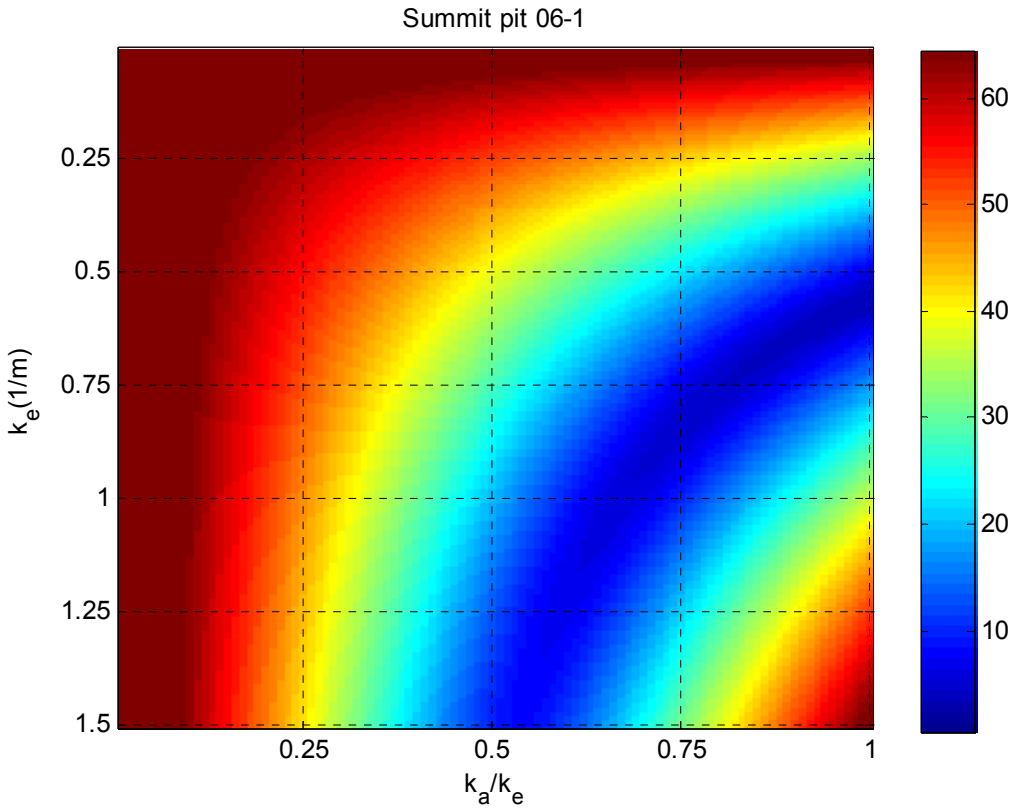

Figure 3.7 Root mean square error (RMSE) space from fitting equation 3.3 to the measured data at Summit pit 06-1 using different values for the extinction and the absorption number. The RMSE space shows that the measured data is best-fit when the absorption number equals 1and, therefore, scattering is negligible.

fit to the measured data is when the absorption number equals 1 (Figure 3.7 is the RMSE space for equation 3.3 at Summit pit 06-1 and is representative of the RMSE spaces for equation 3.4-3.6 at all pits). This result suggests that $k_a = k_e$, α=0 and the scattering coefficient is negligible at 37 GHz in the firn measured at Summit and Swiss Camp.

With the absorption number set equal to one, the 4 radiative transfer equations (equation 3.3-3.6) were fitted to the measured data, shown in Figure 3.8 for the representative pit Summit pit 06-1. Figure 3.9 shows the RMSE fit of the extinction coefficient at each pit. Each equation produced nearly identical fits to the measured T_B data and small variations in the fitted extinction coefficients. The largest deviation in equation fits is between the equations that use a mean sky T_B (equations 3.3 and 3.4) and the equations that use the sky T_B that was measured between each layer (equations 3.5 and 3.6). At Summit pit 06-1 there was an anomalous drop of 10 K in the sky T_B at a firn depth of 0.95 m which explains the split in the equation fits at this point. A similar drop in T_B is also detected in the firn measurements implying that the equation is reproducing the measurements. A large drop in sky T_B also occurred at one measurement at Summit pit 06-3 and explains the larger RMSE for the equations using the mean sky T_B in Figure 3.9, the equations could not adjust to the suddend change in sky T_B. There are only two points in the dataset where an anomalously

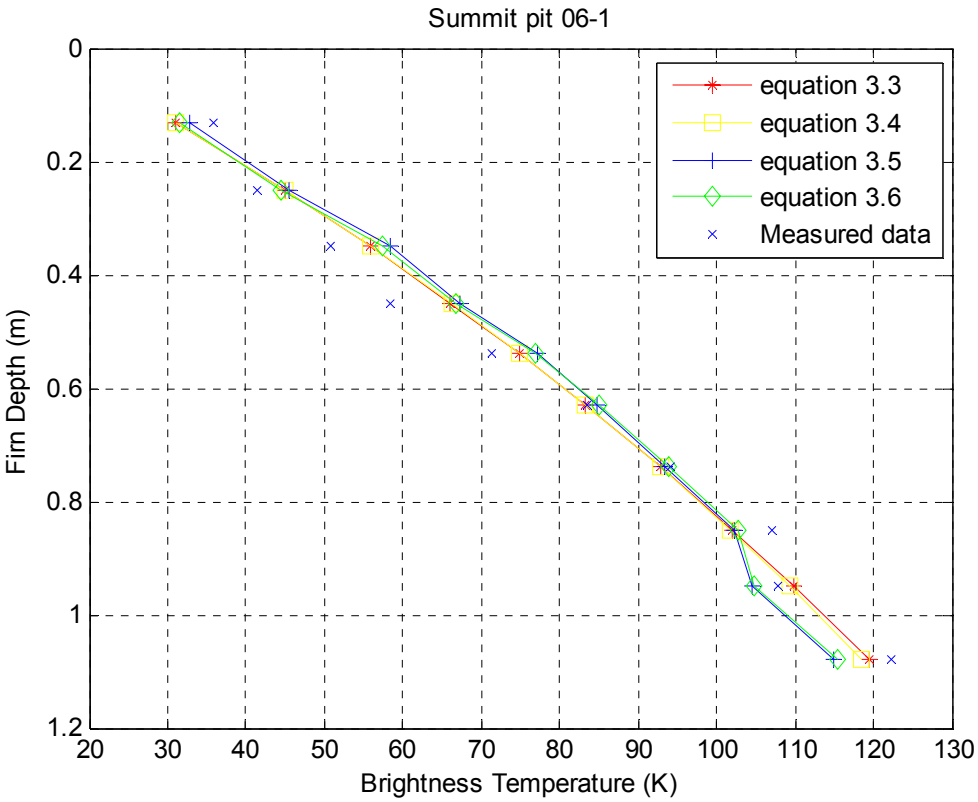

Figure 3.8 Radiative transfer equations fitted to the measured data showing that all of the radiative transfer equations fits are nearly identical.

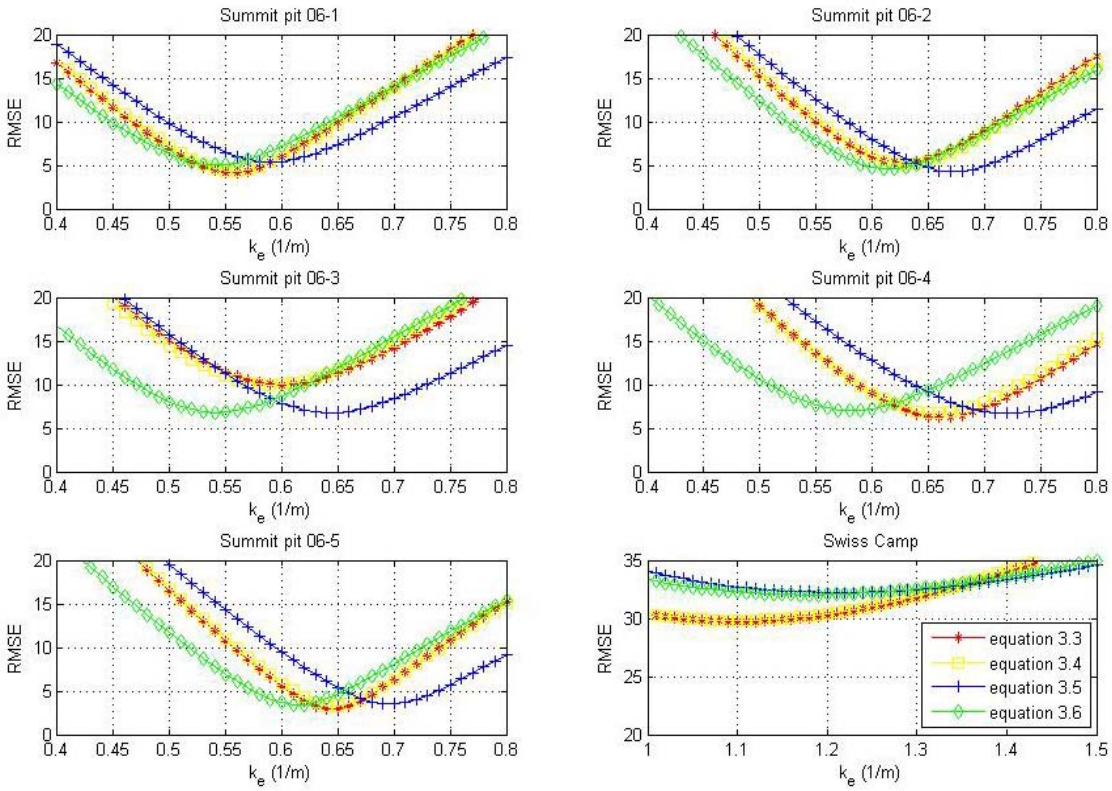

Figure 3.9 RMSE curve for the 4 radiative transfer equations showing a single minima and the variation in the fitted extinction coefficient at each pit.

low sky T_B and firn T_B were measured, one occurred on the first measurement of the day and one on the second. It is possible that the radiometer was not yet temperature stable and these error are do to the instrumentation and not an actual change in T_B. It is, however, unknown if the sky temperature cooled suddenly during these two measurements so they are left in the data set. In general the sky T_B varied smoothly over a range of about 10 K during radiometer measurements and in the normal situation the mean sky T_B is a good approximation. Equations 3.5 and 3.6 are more sensitive to changes in sky T_B and this explains the change in slope of fit lines compared to the smoother fits obtained by the other two equations

Overall equation 3.3 and 3.4 fitted the data with the lowest RMSE and equations 3.5 and 3.6 have higher RMSE values with the noticeable exception of Summit pit 06-3 where there was a large sky brightness temperature drop as explained above. Equation 3.3 and 3.4 are used to fit k_e, the fits are never more than 0.01 (m^{-1}) different, and error bars are placed on the measurement by using equations 3.5 as the upper error bar and 3.6 as the lower error bar. Fitted error bars are always larger than errors introduce but cutting and measuring the firn column in the field, which is estimated at 5 cm.

3.6.2 Measured extinction lengths

A summary of the measured extinction lengths for each pit is given in Table 3.1. Extinction lengths were measured by both radiometer and radar. The radiometer

Table 3.1 Field-based measurements of the extinction coefficient and extinction length for all pit locations and the SFT-modeled extinction length.

Name of Pit	Measuring Device	Measured Extinction Length at 37 GHz (m)	SFT-Modeled Extinction Length at 37 GHz (m)	Extinction Coefficient at 37 GHz (m^{-1})
Swiss Camp	Radiometer	$0.90 \pm^{?}_{0.08}$	0.18	$1.10 \pm^{0.11}_{?}$
Summit 06-1	Radiometer	$1.79 \pm^{0.07}_{0.09}$	0.17	$0.56 \pm^{0.03}_{0.02}$
Summit 06-2	Radiometer	$1.59 \pm^{0.03}_{0.09}$	0.15	$0.63 \pm^{0.04}_{0.01}$
Summit 06-3	Radiometer	$1.67 \pm^{0.19}_{0.10}$	0.17	$0.60 \pm^{0.04}_{0.06}$
Summit 06-4	Radiometer	$1.52 \pm^{0.08}_{0.13}$	0.17	$0.66 \pm^{0.06}_{0.08}$
Summit 06-5	Radiometer	$1.56 \pm^{0.09}_{0.13}$	0.08	$0.64 \pm^{0.06}_{0.03}$
Summit 07-1	FMCW Radar	$1.00 \pm^{?}_{0.42}$ *	Na	1.00*

* Denotes that the FMCW radar measurement is from 32 to 40 GHz

errors were explained above. Error is more difficult to assess for the radar measurements because there were only 5 reliable data points, deep within the pit. The error on the radar measurement was assessed by randomly removing one point and refitting. The standard deviation of the different fits was used as the error. If one point is randomly removed the extinction length varies from 1 m to 0.28 m. A large amount of uncertainly is expected in the fit because measurements are concentrated in one portion of the exponential curve and not evenly distributed through out the curve. Removing points always lowered the extinction length so only a negative error is assessed.

The Summit radiometer pits are dispersed over a 25 km radius around Summit Station (Figure 3.4) with a measured extinction length range from 1.52 to 1.79 m.

Figure 3.10 shows the brightness temperature to depth data collected by radiometer at each pit along with the fitted curve from equation 3.3 using radiometer data collected at 0, 10, 20 and 30 degrees to vertical. Table 3.2 summarizes the radiometer measured extinction lengths calculated for all zenith angles. In most cases extinction lengths measured off zenith agree within 0.1 m. The radiometer was oriented to measure the horizontal polarization for angled measurements. The measurements taken at 30 degrees have the shortest extinction length, which does suggests that at higher incident angles the effects of firn layers are causing the extinction length to shorten. This result, however is not conclusive because there is more scatter in the 30 degree measurements that can be explained by the difficulties in positioning the radiometer for the 30 degree measurement. In the future these measurements should be taken with the radiometer on a stable mount system to better address extinction length changes with incidence angle.

Figure 3.11 is a compilation of all the radiometer data at all angles for Summit. Using all the field data, an extinction length of 1.54 ± 0.1 m is calculated for the area around Summit using the 37 GHz Radiometer. Figure 3.12 is identical to Figure 3.11 but for Swiss Camp, Greenland where the extinction length is calculated to be 0.77 ± 0.13 m. Average error bars have been prescribed to the compilation extinction length measurements because the layered modeled cannot be run using the compilation data.

Figure 3.13 shows the FMCW radar data and the fitted curve calculated from equation 3.12. As shown in Table 3.1 the extinction length from the radar data is

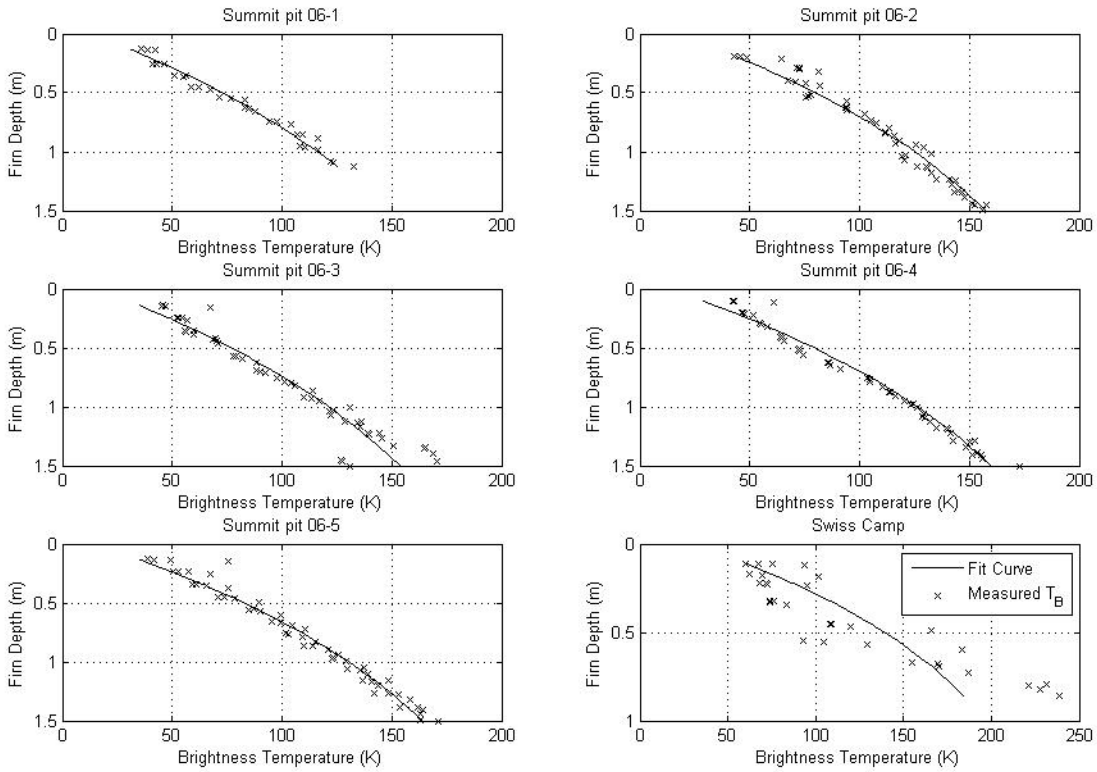

Figure 3.10 Changes in radiometer brightness temperature with depth shown for radiometer angles of 0, 10, 20 and 30 degrees off of vertical. The line is fitted using equation 3.3. Data was gathered in May and June, 2006. Exact pit locations are shown in figure 3.4.

Table 3.2 Field-based measurements of extinction length in meters given for each pit at each radiometer angle. The 10, 20, and 30 degree angles are measuring 37 GHz horizontally polarized emission. Most extinction lengths agree within 0.1 m.

Pit	0 deg	10 deg	20 deg	30 deg	All angles
Swiss Camp	0.91	0.87	0.80	0.67	0.77
Summit 06-1	1.79	1.72	1.61	na	1.69
Summit 06-2	1.59	1.56	1.54	1.43	1.54
Summit 06-3	1.67	1.64	1.64	1.54	1.61
Summit 06-4	1.52	1.49	1.52	1.49	1.49
Summit 06-5	1.56	1.45	1.39	1.30	1.41

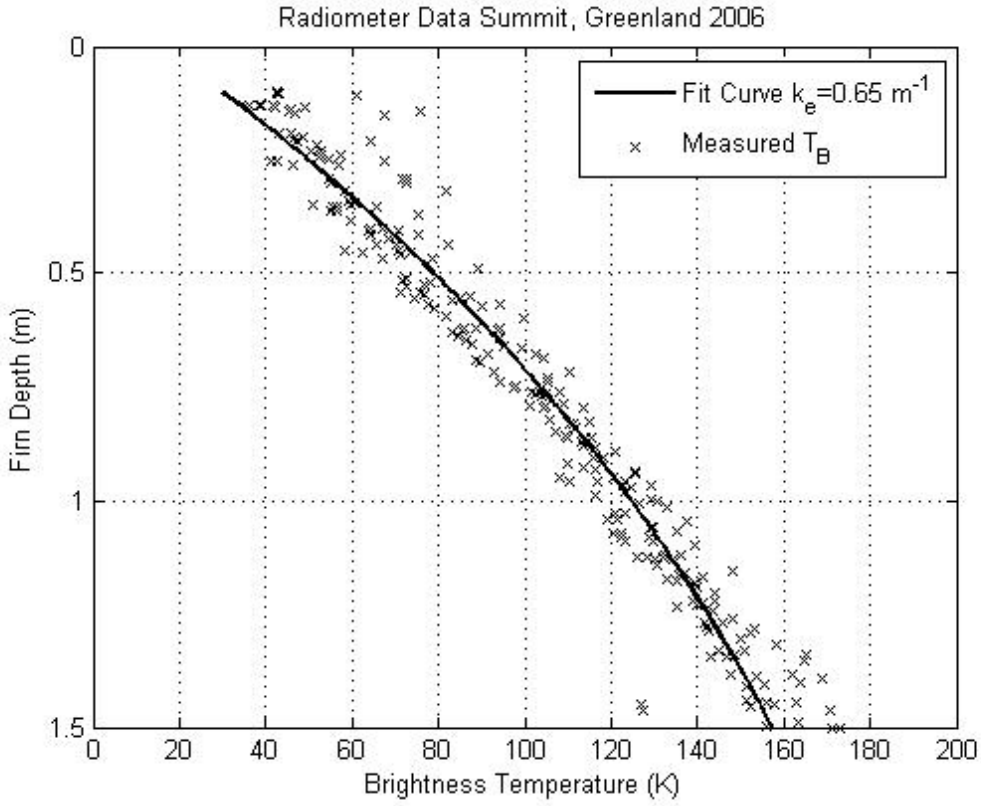

Figure 3.11 Changes in radiometer brightness temperature with depth adjusted for radiometer viewing angle for all data gathered at Summit. The black line is the best-fit to the data using equation 3.3 and gives an extinction length of 1.5 m.

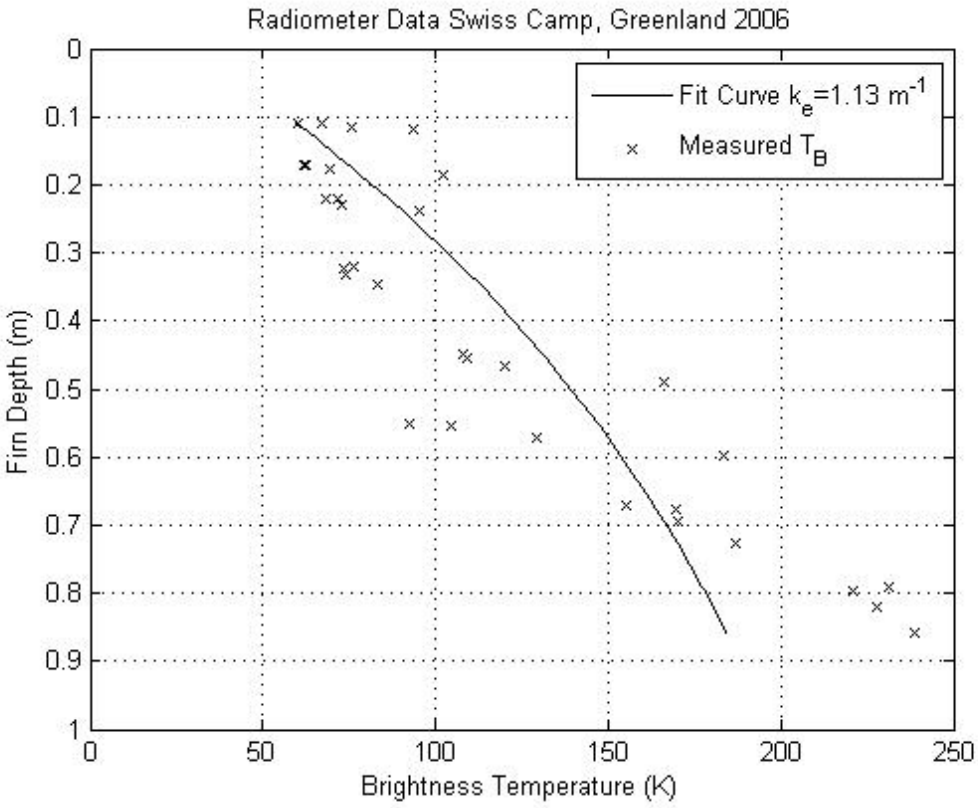

Figure 3.12 Changes in radiometer brightness temperature with depth adjusted for radiometer angle for all data gathered at Swiss Camp. The black line is the best-fit to the data using equation 3.3.

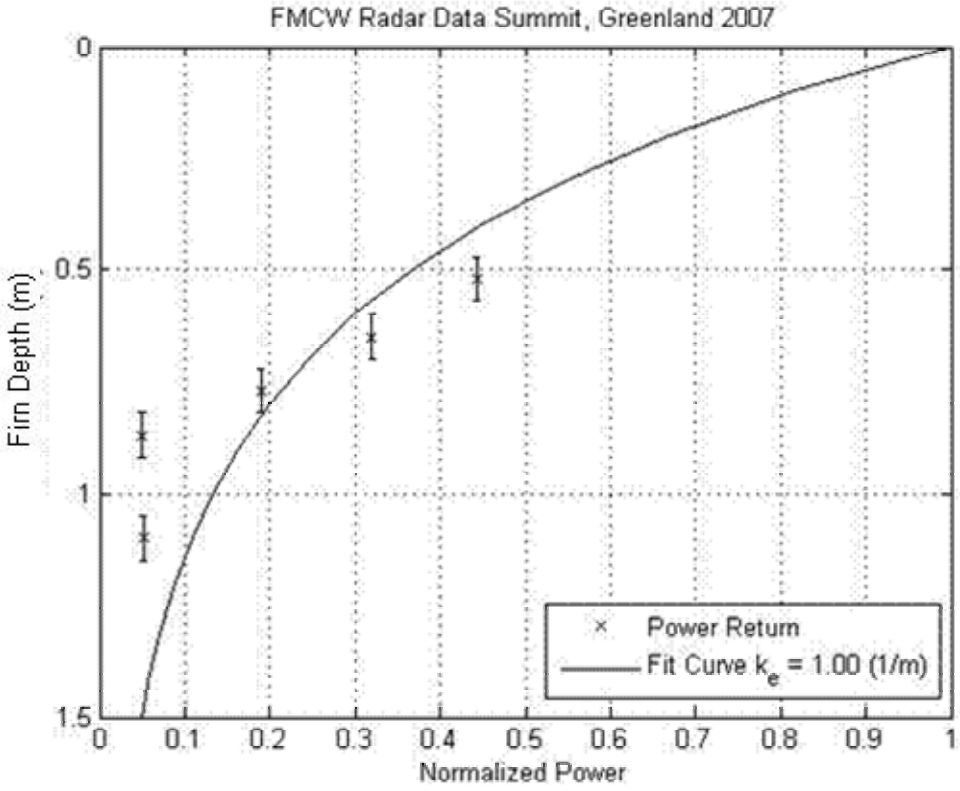

Figure 3.13 Radar data from Summit pit 07-1 at Summit, Greenland with the fitted line derived from equation 3.12. Note that firn depth is multiplied by two when calculating extinction lengths because of the two way travel of the radar wave.

calculated to be $1.00 \pm^{?}_{0.42}$ m at Summit. This has large errors in comparison to the radiometer data because the luneberg lens was operating in the near-field of the radar in the top portion of the pit. The FMCW extinction length is shorter by 0.5 m than the radiometer measurements averaged for the entire Summit area. The FMCW radar data was taken 1 year after the radiometer data which could account for the some of the difference in the measurements but the large error in the measurements likely explains most of the difference. A longer dataset is desired to look at expected temporal variations. The radar measurement is not as reliable as the radiometer measurements and there is a lack of confidence in the radar measurement explained by not having a full set of measurements to calculate the extinction length. Future work with the radar and methodology will produce better results and an extinction length measurement with smaller error bars.

3.6.3 SFT-modeled extinction lengths and stratigraphy

Table 3.1 shows the SFT-modeled extinction lengths for each radiometer pit using the stratigraphy and microstructure information summarized in Table 3.3. The modeled extinction lengths, calculated using the firn density and grain size range from 0.08 to 0.18 m, an order of magnitude shorter than the measured range of 1.52 to 1.79 m. Figures 3.14-3.19 compare the measured density and grain size at each layer to the measured and modeled extinction lengths at the each radiometer pits. Figures 3.14-3.19 show that modeled extinction lengths compare best with measured extinction length in the top few centimeters of the pits.

Table 3.3 The average stratigraphy information for each pit. Cast firn density and cast grain size were calculated in the lab using stereology measurements on the dimethyl phthalate casts of firn.

Pit	Firn Temp. (C)	Firn Density (kg/m3)	Cast Firn Density (kg/m3)	Mean Grain Size (Macroscope) (mm)	Mean Cast Intercept length (mm)	Hand Hardness
Swiss Camp	-11.5	357	Na	0.6	na	3.7
Summit 06-1	-27.7	309	178	0.8	0.26	3.1
Summit 06-2	-28.1	323	Na	0.8	na	3.1
Summit 06-3	-27.0	327	Na	0.8	na	3.4
Summit 06-4	-27.2	312	Na	0.8	na	2.7
Summit 06-5	-26.0	331	172	1.2	0.24	2.9
Summit 07-1	Na	310	Na	0.9	na	2.6

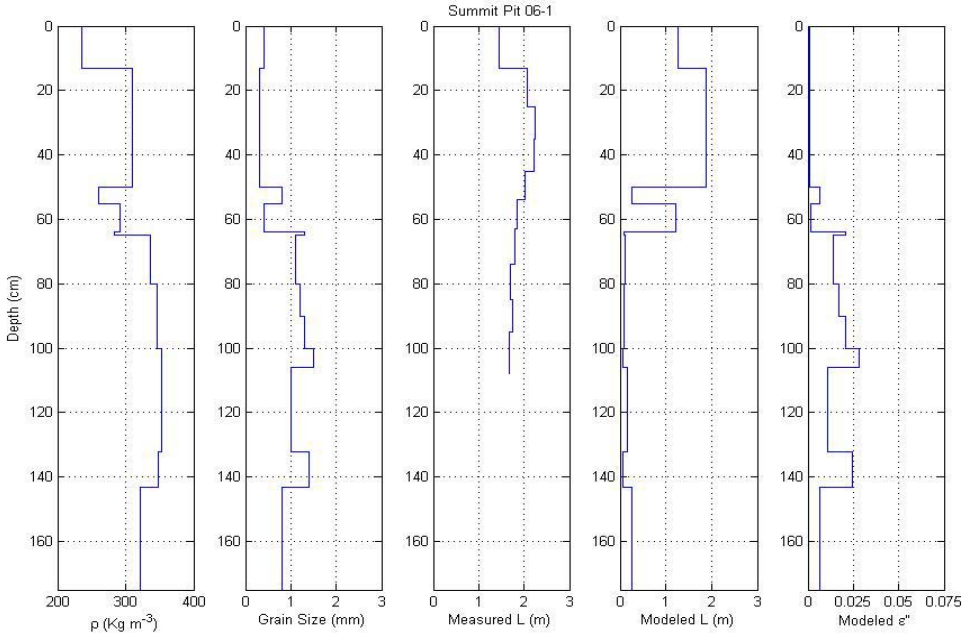

Figure 3.14 Plots of density, grain size, measured extinction length, modeled extinction length and the imaginary part of the complex relative permittivity for pit Summit 06-1.

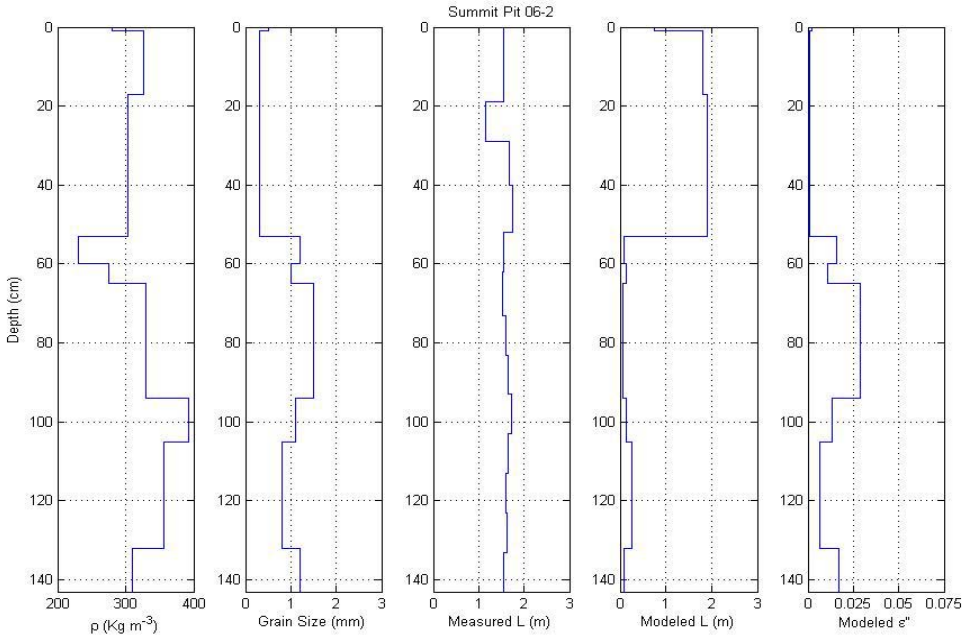

Figure 3.15 Plots of density, grain size, measured extinction length, modeled extinction length and the imaginary part of the complex relative permittivity for pit Summit 06-2.

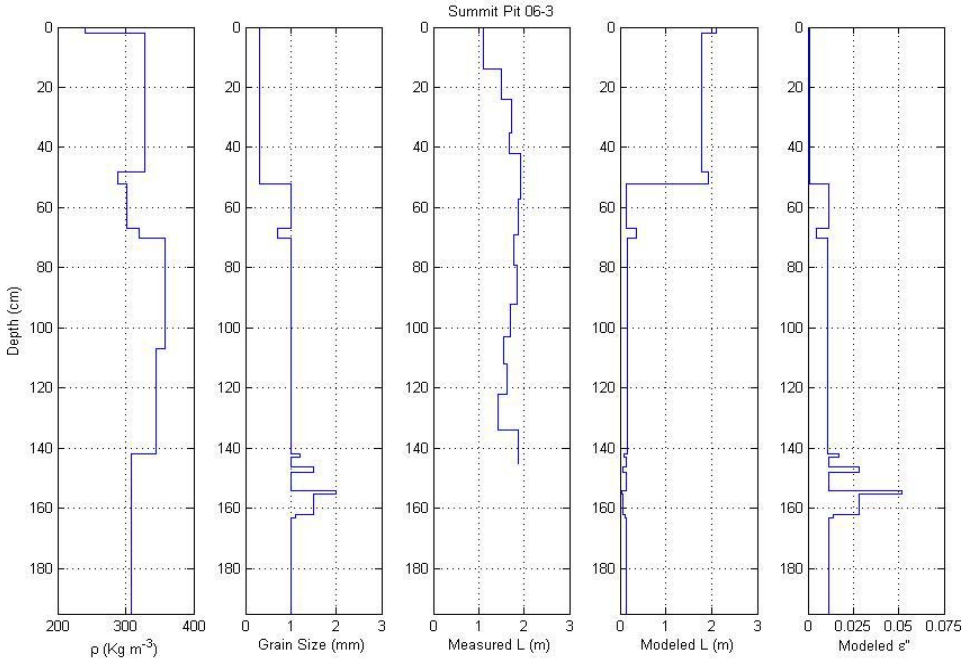

Figure 3.16 Plots of density, grain size, measured extinction length, modeled extinction length and the imaginary part of the complex relative permittivity for pit Summit 06-3.

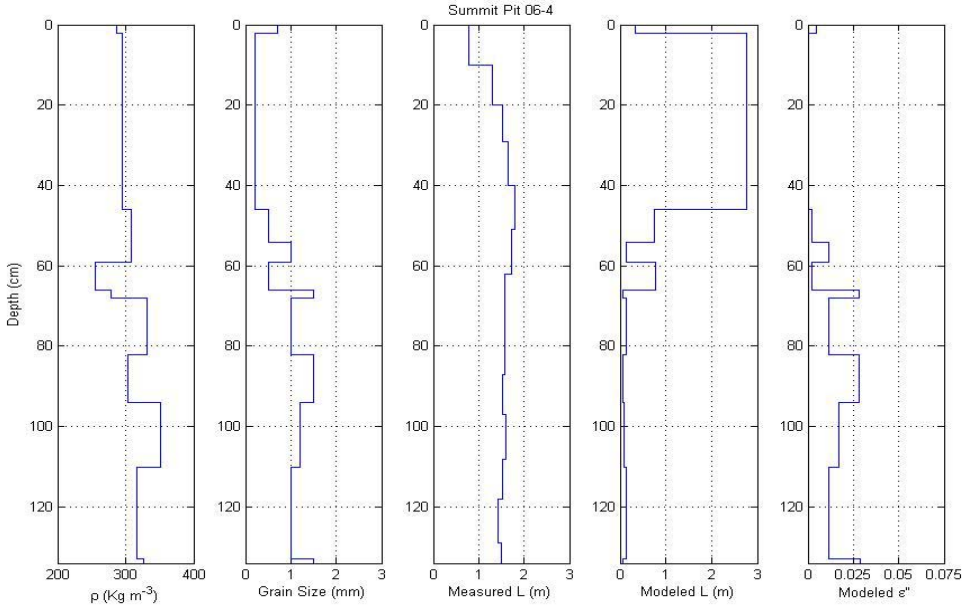

Figure 3.17 Plots of density, grain size, measured extinction length, modeled extinction length and the imaginary part of the complex relative permittivity for pit Summit 06-4.

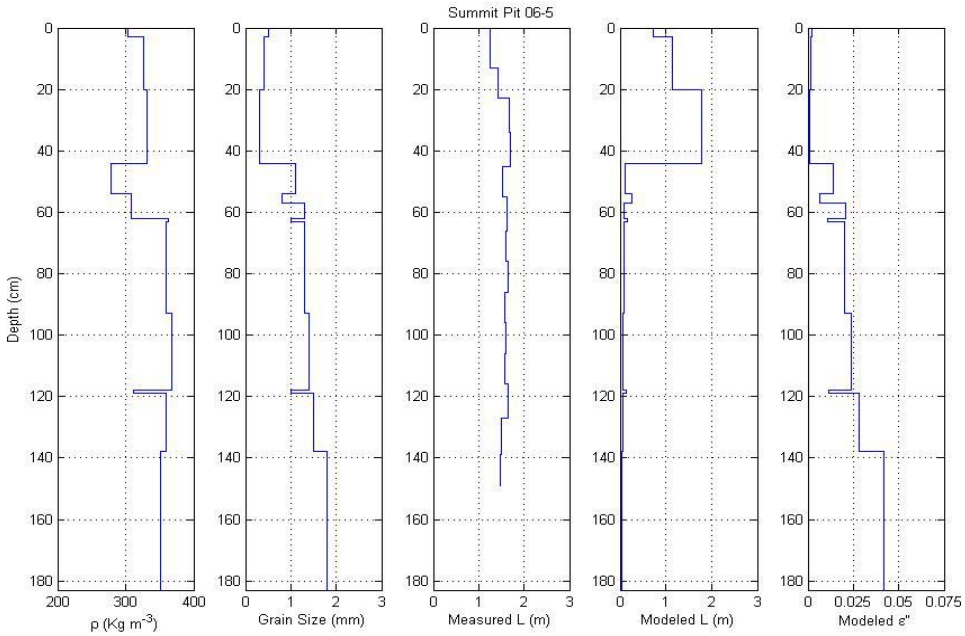

Figure 3.18 Plots of density, grain size, measured extinction length, modeled extinction length and the imaginary part of the complex relative permittivity for pit Summit 06-5.

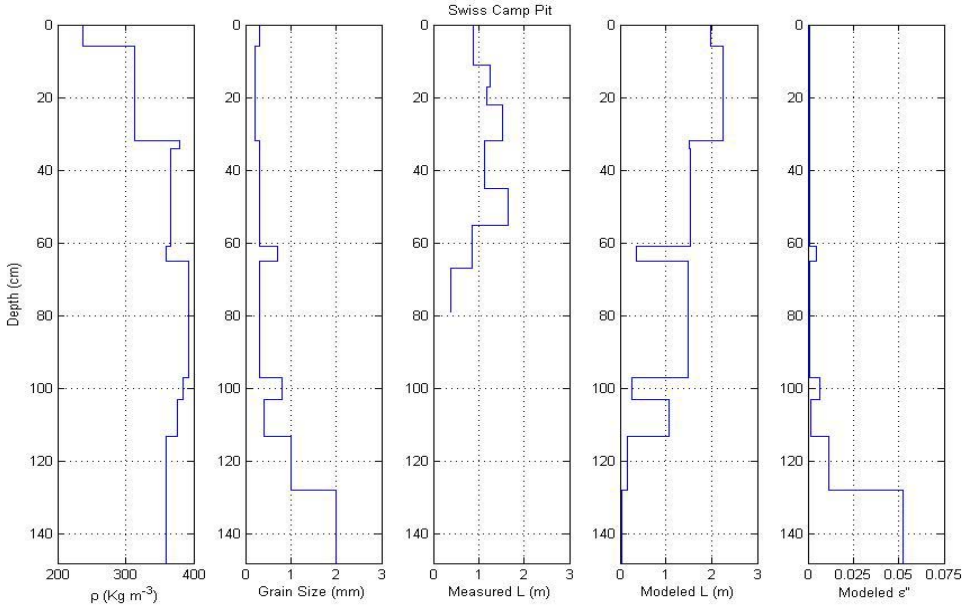

Figure 3.19 Plots of density, grain size, measured extinction length, modeled extinction length and the imaginary part of the complex relative permittivity for pit Swiss Camp.

In this region the grain size is smaller and the measured extinction lengths are more likely to underestimate because the firn column depth is small compared to the surface area of the column allowing emitted radiation to exit out of the edges as described for snow blocks in section 3.3. Figure 3.20 compares the measured extinction length at each firn depth for the all the Summit radiometer pits. The scatter at low firn depths illustrates that then firn columns, or blocks, are not sufficiently think to measure an accurate extinction length.

Figure 3.21 is a scatter plot of measured to modeled extinction lengths. The one to one line is shown for comparison. In general the model is underestimating the measured value. Figure 3.22 and 3.23 investigate further the controls on why the modeled value is underestimating. Figure 3.22 shows a scatter plot of density to extinction length grouped by modeled and measured values. Density changes do not have a strong effect on the modeled extinction length in contrast to the grain size. Figure 3.23 shows a scatter plot of grain size to extinction length grouped by modeled and measured values. The modeled values fall into an exponentially decreasing pattern as determined by the SFT model while the measured values show no strong decrease with grain size, further evidence that scattering is negligible at 37 GHz.

The SFT model does not reproduce measured values of extinction length. The SFT model can only reproduce measured values when grain size ranges from 0.3-0.4 mm. The SFT model is sensitive to grain size. This is in contrast to the radiometer

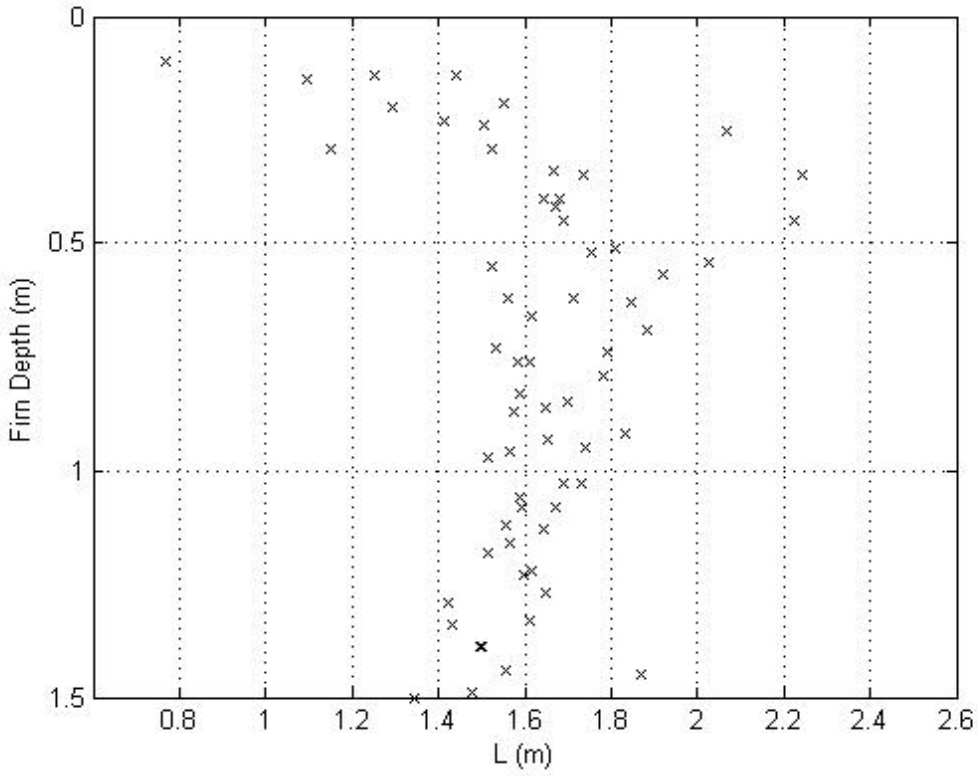

Figure 3.20 Measured extinction length compared to thickness of firn column used to calculate the extinction length. Scatter is evident when the firn thickness, or depth, is small compared to the extinction length.

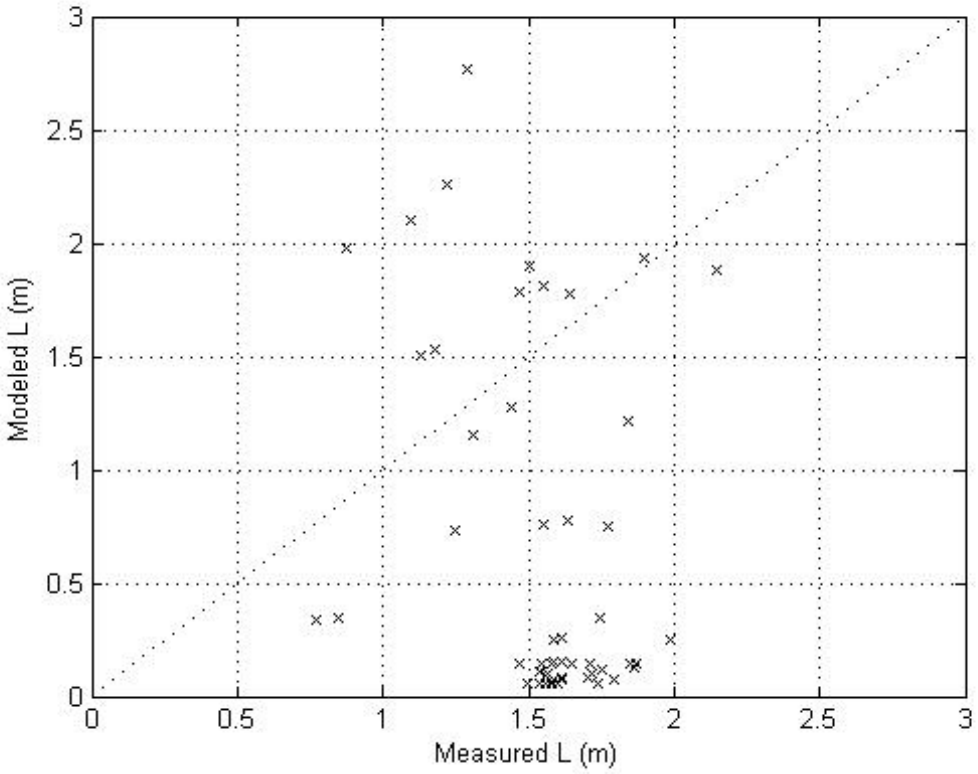

Figure 3.21 Scatter plot of measured verses modeled extinction length values. The modeled values are generally lower than the measured value.

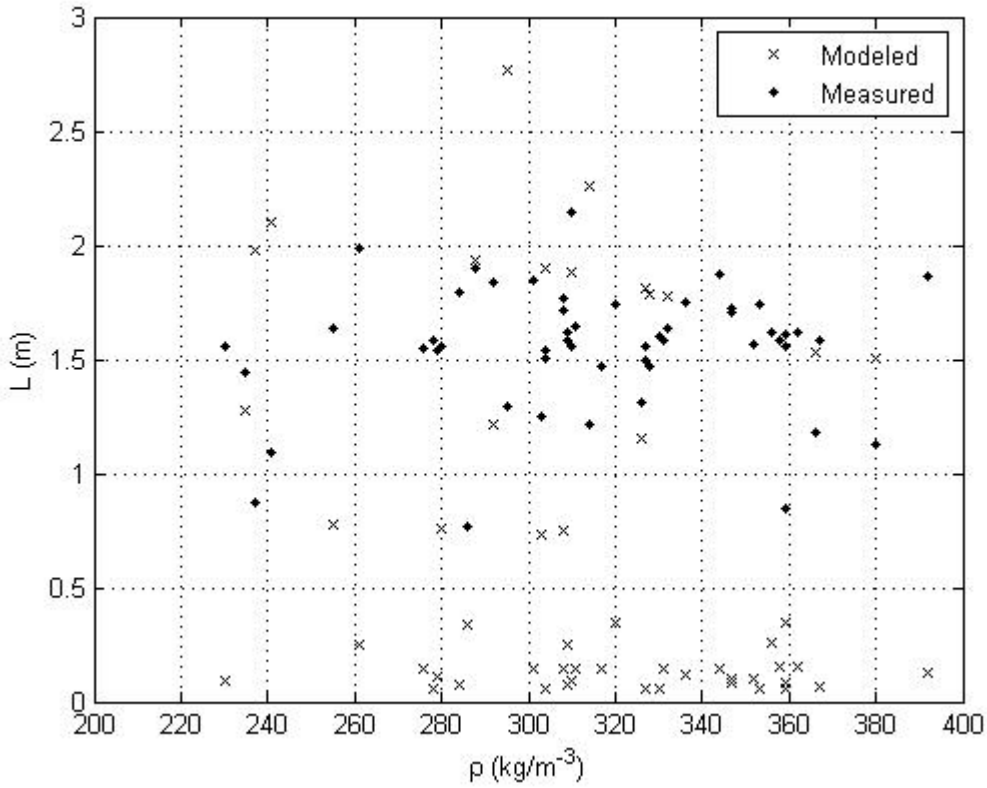

Figure 3.22 Scatter plot of density to extinction length (L) for both the modeled and measured values. There is no clear relationship between density and the extinction length.

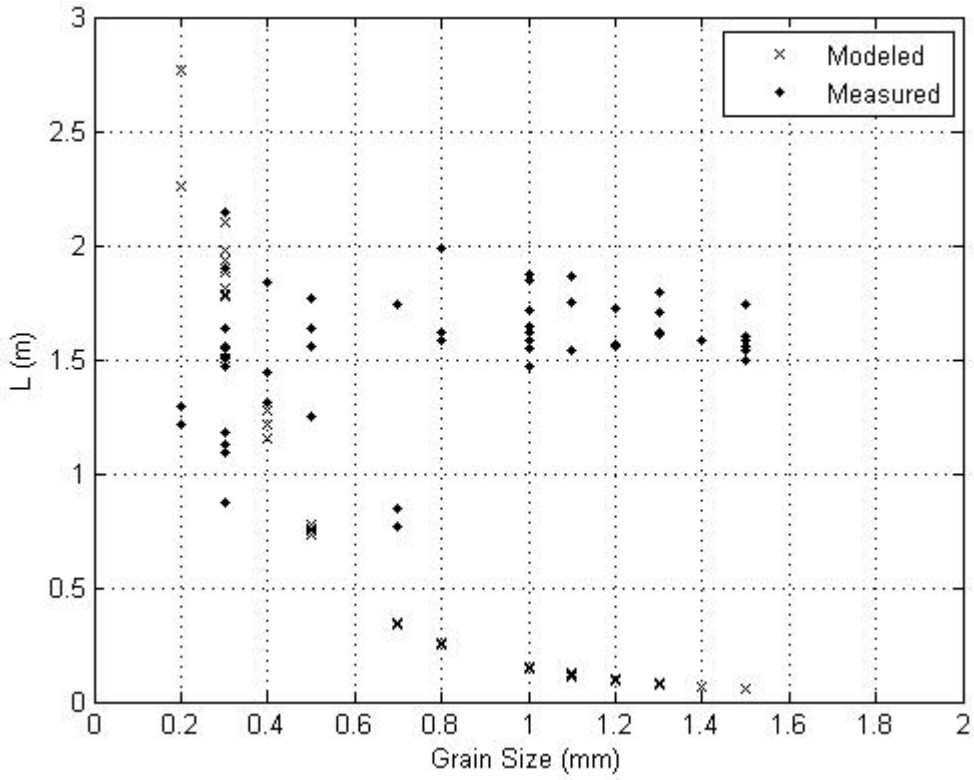

Figure 3.23 Scatter plot of grain size to extinction length (L) for modeled and measured values. The strong exponential decrease with grain size is shown for the model. The measured values do not show as strong of a decrease with grain size.

measurements which show no dependence on grain size (Figures3.23) and are only reproduced by radiative transfer equations with k_s=0. Remembering that $k_e = k_a + k_s$, Figure 3.5 shows the sensitivity of the SFT modeled k_e to scattering, the slope of the line at grain sizes larger than 0.1 mm represents an increase in k_s.

The SFT model's sensitivity to grain size merits an investigation of grain size measurements. Grain size measurements are not straight forward. *Mätzler* [2002] summarizes different methods that have been used to measure grain size. Three grain size measurements will be discussed here, field-measured grain size from a macroscope and, from stereology calculations on dimethyl phthalate casts of the firn, correlation length and volume to surface area ratios. The field-measured grain size is defined as the average grain width as viewed with a macroscope in the field on a crystal card. This method is biased by the observer and often over estimates the actual grain size because connected particles are often measured as a single grain; however, it is a simple measurement to take in the field and is commonly used. The intercept length, denoted cast grain size in Table 3.3, is the mean length of random line across grains calculated from a binary image of the dimethyl phthalate cast [*Davis et al.,* 1987].

A third measurement of grain size is the volume to surface area ratio, also called the optical grain size or the inverse of the specific surface area, and is a preferred measurement of grain size for electromagnetic modeling [*Davis et al.,* 1987; *Shi et al.,*1993; *Grenfell and Warren*, 1999*; Mätzler*, 2002]. The volume to surface

area ratio is defined as a cloud of spherical particles whose surface area and volume equal that of the irregularly shaped snow grain. Using multiple spheres provides a grain size with equal area, to model scattering of the wave, and equal volume, to model the absorption of the wave, to the original irregularly shaped grain. The volume to surface ratio has been shown to model radiation well in the ultra violet, visible, near IR and microwave range and can be calculated from stereology measurements [*Grenfell and Warren*, 1999; *Mätzler*, 2002; *Davis et al.,* 1987]. In the first runs of the SFT model, presented above, the grain width was used as the diameter of a perfect sphere. In reality grains are not perfect spheres, so the width grain size overestimates the volume of the sphere and increases scattering in the model, most likely causing the underestimation of the measured values of extinction length [*Grenfell and Warren*, 1999; *Mätzler*, 2002].

Intercept length and the volume to surface area ratio were input to the SFT model to calculate extinction lengths. Modeled extinction lengths from the grain intercept lengths are 2.25 and 2.27 m for Summit pit 06-1 and 06-5, which overestimate the measured values by 0.46 and 0.71 m respectively. Modeled extinction lengths from the volume to surface area ratio are 3.07 and 3.32 m for Summit pit 06-1 and 06-5, which overestimate measured values by 1.28 and 1.76 m.

None of the grain size measurements input to the model were able to reproduce the measured values. The field measured width underestimates the extinction lengths while the intercept length and volume to surface area measurements overestimate.

There are errors associated with the dimethyl phthalate cast measurements that should be addressed. Error is introduced by converting the original image to a binary image and with the filtering process causing a decrease in grain size. It has also been shown that the 2-D thick sections of snow can cause an underestimation of grain size of approximately 40% to the grain size from a 3-D micro-CT scan at Hercules Dome, Antarcitca [*Hörhold*, 2006]. Both of these errors decrease grain size and would produce larger errors in the SFT modeled extinction lengths. It is concluded that the SFT model is overly sensitive to grain size changes and that it cannot reproduce the measured values. Explaining why the SFT model cannot reproduce the extinction length measurements will be left for future work.

It is interesting to revisit Figure 3.5 knowing that the fit k_e's from the radiative transfer equations is ~0.6 for Summit and ~1.1 for Swiss Camp and that the radiative transfer equations required that $k_e = k_a$. The SFT modeled k_a's were 0.3 for Summit and 0.4 for Swiss Camp much lower than radiative transfer equations predict.

Impurities in the ice were investigated as a possible explanation of the discrepancy between the SFT modeled k_a and the radiative transfer fit k_a. Impurities in the ice, mainly from sodium chloride, cause an increase in the loss factor, imaginary part, of the dielectric constant of ice [*MacGregor et al.,* 2007; *Matsuoka et al.,* 1996; Mätzler and Wegmüller, 1987; Surdky and Fujita, 1995]. The sodium concentration taken from the GISP2 ice core is 5 ppb and gives an impurity measurement for Summit [*Mayewski et al.,* 1997]. Adjusting the SFT model for the dielectric constant

of impure ice, from that of pure ice, does not change the absorption coefficient within significant figures. No measurement of impurity concentration was available at Swiss Camp but it is expected to be small. *Surdyk and Fujita* [1995] report adjusting the loss factor by 3% for impurities in glacier ice. This small adjustment does not explain the large underestimation of k_a in the SFT modeled. Explaining why the SFT model is underestimation k_a requires an in-depth understanding of the model and will be left for future research.

The extinction lengths measured in this study are slightly longer than most previous studies done in the lab or with snow blocks. They do fall into the range of modeling work done by *Surdyk* [2002] at 37 GHz who was using a similar SFT model to the one used here. The measured extinction lengths fall in the same range as those measured by *Hallikainen et al.* [1987] for all snow types but could not be reproduced by his empirical equation using grain size. Grain size proves to be a difficult parameter to measure consistently and precisely and future work needs to be devoted to grain size measurements.

3.7 Conclusion

The field-measured microwave extinction length at 37 GHz for Summit, Greenland is approximately 1.6 m. The field-measured microwave extinction length at 37 GHz for Swiss Camp, Greenland is approximately 0.9 m. The microwave extinction lengths are determined by fitting radiative transfer equations to the field

data. The radiative transfer equations only fit the data when the scattering coefficient is set to zero, suggesting negligible scattering at 37 GHz. Simple radiative transfer equations using mean firn temperature values fit the field measurements better than the more complicated models. Extinction lengths measured with the FMCW radars are shorter than the radiometer measurements but this is partially explained by the small amount of measurements used to calculate the extinction length. The FMCW extinction length is not as reliable as the radiometer measurements but shows promise and will be improved upon in the future.

SFT-modeled extinction lengths greatly underestimate or overestimate the measured value depending on the grain size used. The SFT model used is overly sensitive to grain size changes and underestimates the extinction lengths by an order of magnitude given field grain size measurement. The SFT model overestimated extinction length using intercept lengths and volume to surface area ratios determined from stereology measurements for the grain size measurement. The SFT model is very sensitive to scattering from grains while the measured data shows negligible scattering at 37 GHz.

Reliable measurements of field-based extinction lengths can be taken using an FMCW radar and radiometer. The methods presented here can be deployed at additional ice sheet locations with varying accumulations rates. Determining how extinction length changes with firn microstructure and accumulation rate will further

the capabilities of space-borne passive microwave sensors to monitor changes in climate parameters over ice sheets.

Chapter 4

ESTIMATING MICROWAVE EXTINCTION LENGTH USING 32-40 GHZ FMCW RADAR PROFILES AT SUMMIT, GREENLAND AND TAYLOR DOME, EAST ANTARCTICA

4.1 Summary

Microwave extinction length in polar firn depends on firn properties such as grain size, temperature and density. Few direct measurements of both microwave extinction length and firn properties have been obtained in the field. A better understanding of the relationship between microwave extinction length and firn properties may enhance the utility of space-borne microwave sensors in determining temperature, accumulation rate, or other firn properties of interest on polar ice sheets. A method is presented for estimating microwave firn-extinction length from radar profiles. At Summit, Greenland, the radar-profile-derived extinction length (~0.8 m) underestimates the radiometer-measured extinction length (~1.6 m) by half. At Taylor Dome, East Antarctica the radar-profile-derived extinction length at 32–40 GHz is ~0.6 m. Radar-profile-derived extinction lengths provide a consistent way of comparing data at sites with different accumulation rates.

4.2 Introduction

Microwave extinction length is sensitive to firn properties that vary with accumulation rate. These firn properties include grain size, density and temperature. With a better understanding of the relationship between extinction length and accumulation rate [*Koenig et al.,* 2007], space-borne passive microwave sensors could potentially be used to measure ice sheet accumulation rates. However, little extinction length data exists; more data are needed, covering a wide range of accumulation rate.

Ideally, extinction lengths are measured in-situ using radars with retroreflectors placed at varying depth in the firn, or using a radiometer placed below large columns of firn with varying height (Chapter 3). These methods, however, are time consuming. On the other hand, there is a wealth of information already available from radar surveys collected in profile form, where the radar is pulled on a sled over some distance. The radar profiles record the received power, or backscatter, from the internal layers in the firn along the profile. Several previous studies have collected profile data at microwave frequencies on the Greenland Ice Sheet and the Devon Ice Cap [*Scott et al.,* 2006; *Legarsky,* 1999; *Marshall*, 2007]. Methods using radar profiles to estimate extinction lengths could significantly increase our understanding of the spatial and temporal variability in extinction lengths.

4.3 Background

Davis and Poznyak [1993] calculated microwave extinction length, at three sites in East Antarctica using a profile from a 10-GHz pulse radar. They estimated the minimum extinction length by first correcting the mean amplitude-versus-depth (A-scope) profile recorded by the radar for geometric spreading loss and the volume increase with range. Once corrected, the loss in the data represents attenuation in the firn from the total extinction coefficient including both scattering and absorption as:

$$P(z) = P_0 e^{-k_e 2z}, \tag{4.1}$$

where P is the power at firn depth z, P_0 is the initial power incident on the surface of the firn and k_e is the extinction coefficient of the firn. P is estimated by taking the total summed power, P_T, of the corrected A-scope data, A_{cor}, squared for power and subtracting the power received to depth z where:

$$P_T = \int A_{cor}(z')^2 \, dz', \tag{4.2}$$

and

$$P(z) \approx P_T - \int_0^z A_{cor}(z')^2 \, dz'. \tag{4.3}$$

The results from equation 4.3 were fitted with equation 4.1 to solve for the extinction coefficient. This method gives a minimum estimate of extinction length because the power transmitted to the firn that is not received at the radar is unaccounted for,

making P_T lower than the true value. Methods used by *Davis and Poznyak* [1993] will be used in this study to estimate extinction length at field sites with profile data.

4.4 Calculating extinction length

FMCW radar profiles are collected by mounting a 32–40 GHz FMCW radar on a sled with the antennas placed 1 m above the snow surface at nadir. The radar is pulled either by hand or by snowmobile. Profile length depended on snow surface conditions and sled maneuvering capabilities and varied from 30 to 320 m. Profiles aim to average out small scale (1 to 10 m) internal firn structures, such as buried sastrugi and other wind depositional features. The profile should be sufficiently long (>100 m an order of magnitude longer than firn structure length scales) to average out internal reflectors, such as layers, so that the received power at the radar represents the total extinction. In practice internal layers persist in the firn over long distances (>100 m), which limits the precision of this method [*Legarsky*, 1999]. There is not yet enough data to assess the precision of radar-profile-derived extinction lengths. Here we will be able to compare for the first time a radar-profile-derived extinction length at Summit, Greenland to a radiometer measurement to get an initial guess at the precision of the estimation method.

Radar profiles consist of multiple amplitude-versus-depth, A-scopes, recorded every 5 ms. Example profiles at and near Taylor Dome, Antarctica and at Summit, Greenland, are shown in Figures 4.1-4.4. In the example profiles the A-scope values

are squared and put on a log scale to report in the power units of decibels by convention. Both dominant firn layers that persist the entire distance of the profile and smaller-scale firn variability are visible. The individual A-scopes are averaged over the entire profile to construct a mean A-scope curve for each profile, again shown in units of power (Figure 4.5). Averaging these data significantly reduces backscatter peaks from small-scale firn structures and allows an estimate of the power extinction, or attenuation, in the firn. Major layers, however, do persist post-averaging, which remains a source of error.

The power backscattered and returned to the radar is given by the radar equation for a distributed source medium with a beam-limited system:

$$P_R = \frac{P_T G^2 \lambda^2 \sigma}{4\pi R^2} A_{ill}, \qquad (4.4)$$

where P_T is the power transmitted, G is the antenna gain, λ is the wavelength, σ is the scattering cross section and R is the range to a point target and A_{ill} is the illuminated area at nadir defined by:

$$A_{ill} = 2\pi(1-\cos\theta)R^2 \qquad (4.5)$$

where θ is the beam-width of the antenna [*Ulaby et al*., 1982; *Scott et al*., 2006].

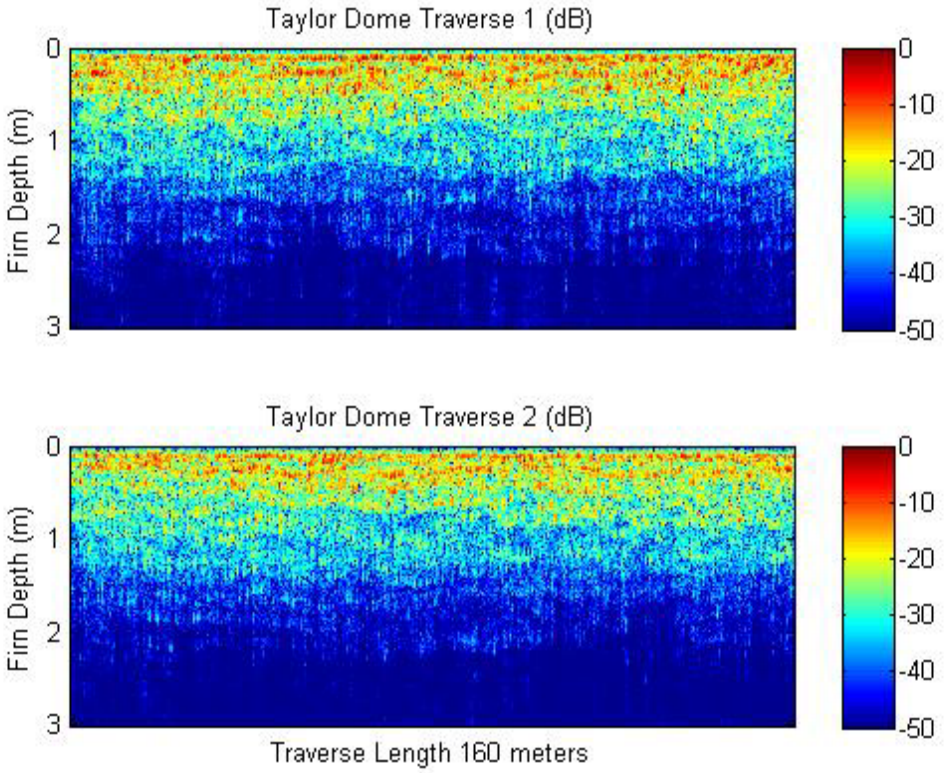

Figure 4.1 Radar echogram in dB of two 160 m profiles near pit AP0601 at Taylor Dome, Antarctica. These profiles are parallel to each other, approximately 1 m apart, and are oriented perpendicular to the dominant wind direction. The top profile is TD1 and the bottom TD2.

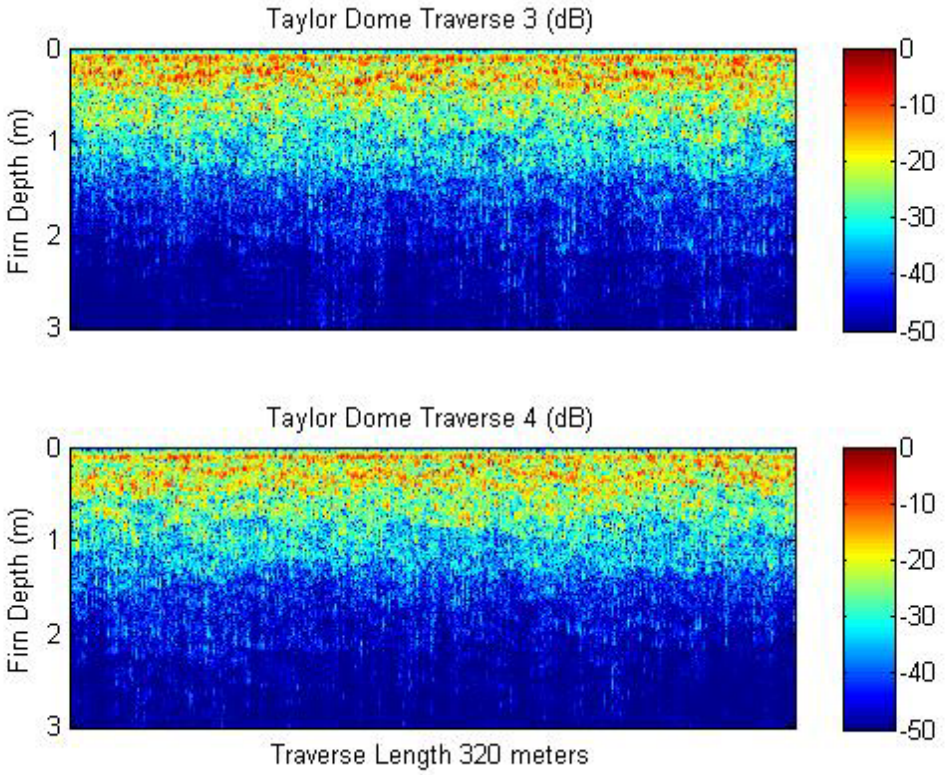

Figure 4.2 Radar echogram in dB of two 320 m profiles near pit AP0601 at Taylor Dome, Antarctica. Profiles are parallel to each other, approximately 1 m apart, and are oriented parallel to the dominate wind direction. The top profile is TD3 and the bottom profile TD4.

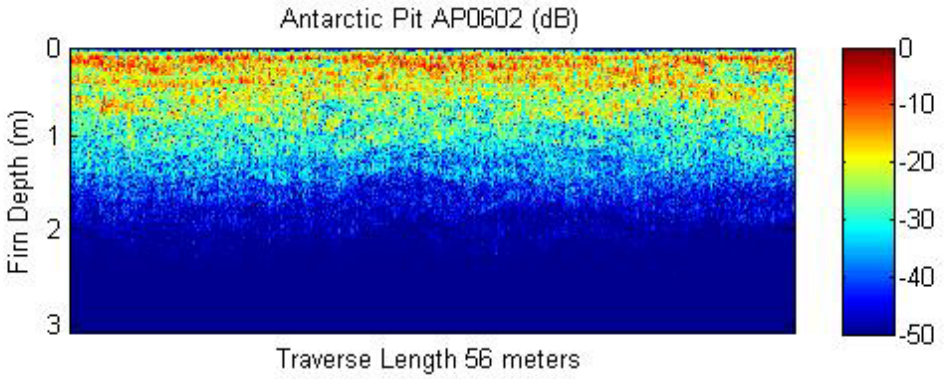

Figure 4.3 Radar echogram in dB of a 56 m profile near pit AP0602 in East Antarctica.

.

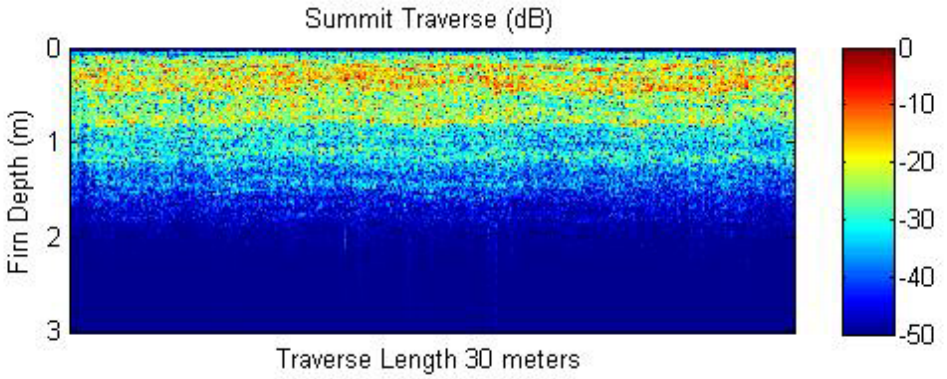

Figure 4.4 Radar echogram in dB of a 30 m profile near pit Summit pit 07-2 at Summit, Greenland.

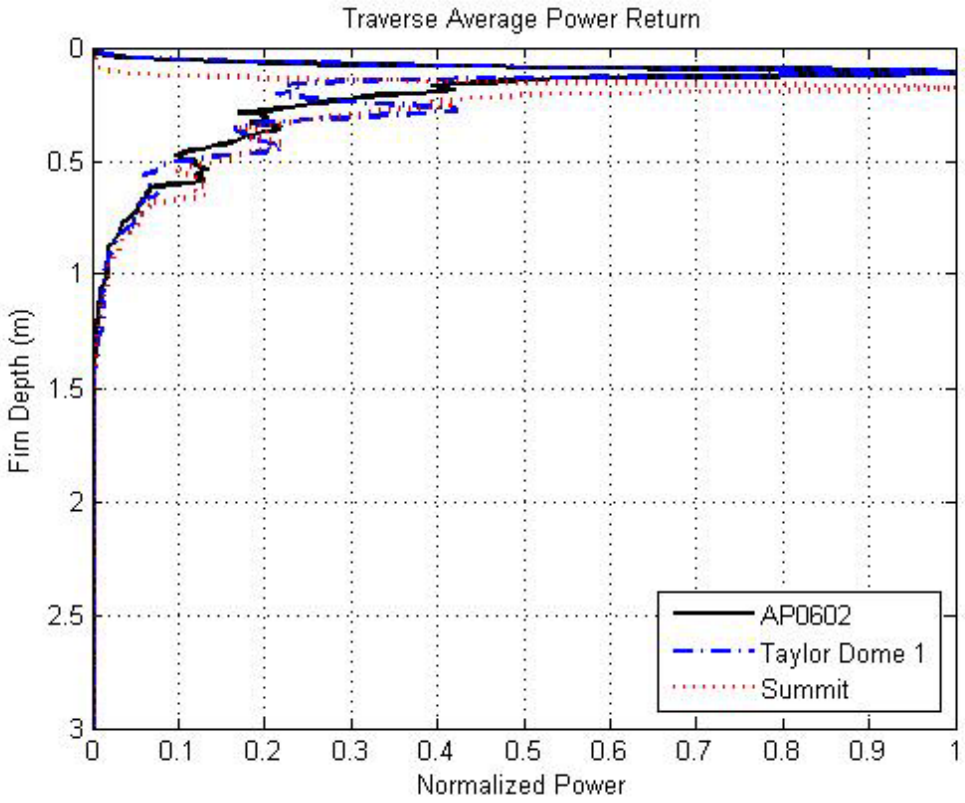

Figure 4.5 Mean power-versus-depth curves, corrected for illumination integral and spreading loss. Taylor Dome profile 1 is considered a representative curve for Taylor Dome. More power is returned at depth in the Summit, Greenland, implying that the firn has a longer extinction length there.

To estimate extinction due only to firn, the mean power-versus-depth curve for each radar profile is corrected for spreading loss and the illumination integral. The corrected power curve is then normalized to the peak power received. After correcting for the spreading and illumination integral, the corrected and normalized received power P_{cor} should display an exponential loss:

$$P_{cor} = P_0 e^{-k_e 2z}, \tag{4.6}$$

where k_e is the total extinction coefficient in the snow. P_0 is unknown so P_{cor} is estimated as a percent total power lost as shown in equation 4.3 and fitted with equation 4.6 to solve for k_e following *Davis and Poznyak* [1993]. Figure 4.6 shows the percent power loss curves. The extinction length L is:

$$L = \frac{1}{k_e}. \tag{4.7}$$

This method only estimates extinction length because the initial transmitted power is not known and the received backscattered power is from firn as opposed to a reflector with known radar cross section thus, there is no direct accounting for power attenuation. For this method to more accurately measure extinction length the power must be backscattered equally through all firn layers. If the latter condition were true, however, there would be no internal layers. Thus, this methodology can only estimate extinction lengths in a consistent way to use existing radar-profile data. These estimates allow relative but consistent comparisons of extinction lengths at locations with different accumulation rates.

4.5 Results and Discussion

Profiles were collected from one site at Summit, Greenland (Summit pit 07-2), four sites at Taylor Dome, Antarctica (TD1, TD2, TD3, and TD4) and at one site south of Taylor Dome (AP0602) (See Figures 5.1 and 5.2 for location maps). The Taylor Dome profiles were collected using a snowmobile and are the longest. The Summit and AP0602 profiles were collected by manually pulling the sled, so they are shorter. The mean power data from the Taylor Dome profiles, in theory, will have averaged out more of the small-scale firn stratigraphy and should be closer to measured extinction lengths.

Figures 4.1-4.4 show the firn stratigraphy in detail. It is evident from Figures 4.1-4.4 that the dominate backscatter in the Antarctic data comes from the top firn layers, whereas in Greenland, backscatter is returned more equally from layers deeper in the firn. The Greenland data (Figure 4.4) show a weak layer at ~ 1.2 m, while the Antarctic data is mostly noise at the same depth, which suggests a longer extinction length in Greenland.

Figure 4.5 shows the mean power curves corrected for spreading loss and illumination integral. To simplify the figure and because all the Taylor Dome power curves are similar, only the curves from AP0602, TD1 (Taylor Dome) and Summit pit 07-1 (Summit) are shown. Figure 4.5 shows the largest backscatter in the Greenland data is from ~ 0.25 m depth and more backscattered power is returned from deeper into the firn than in the Antarctic data. The Antarctic data backscatter peaks close to

the firn surface and very small returns come from larger depths, indicating shorter extinction lengths in East Antarctica than Greenland.

Site-specific firn characteristics can help explain the backscattered return. Figures 4.6-4.8 show the pit stratigraphy recorded near each radar profile. The Greenland pit shows a soft firn layer in the top 0.5 meters, which is contrasted to the much harder firn in the Antarctic pit data. The Antarctic firn had a wind-blown crust, whereas the Greenland firn consisted of soft new snow deposited from summer storms. Peak backscatter returns occur at larger depths in Greenland because the softer snow has less backscatter and more penetration than in Antarctica, where the shallow hard layers backscatter a large portion of the energy.

Figure 4.9 shows the percent-power-loss curves used to estimate the extinction coefficient. Figure 4.9 shows the Greenland profile containing a higher percentage of the total power deeper into the firn. Figures 4.10-4.12 show the fitted extinction-coefficient curves for TD1, AP0602 and Summit pit 07-2 compared to the mean power-curve data. The fit could be improved if the peak return came from the firn surface and by knowing the initial power transmitted by the radar on the surface of the firn. Because the initial power is not known, these values are expected to under estimate of extinction length.

Table 4.1 summarizes the extinction lengths derived from each radar transect, along with the extinction coefficient and the rms error of the fitted curve to the

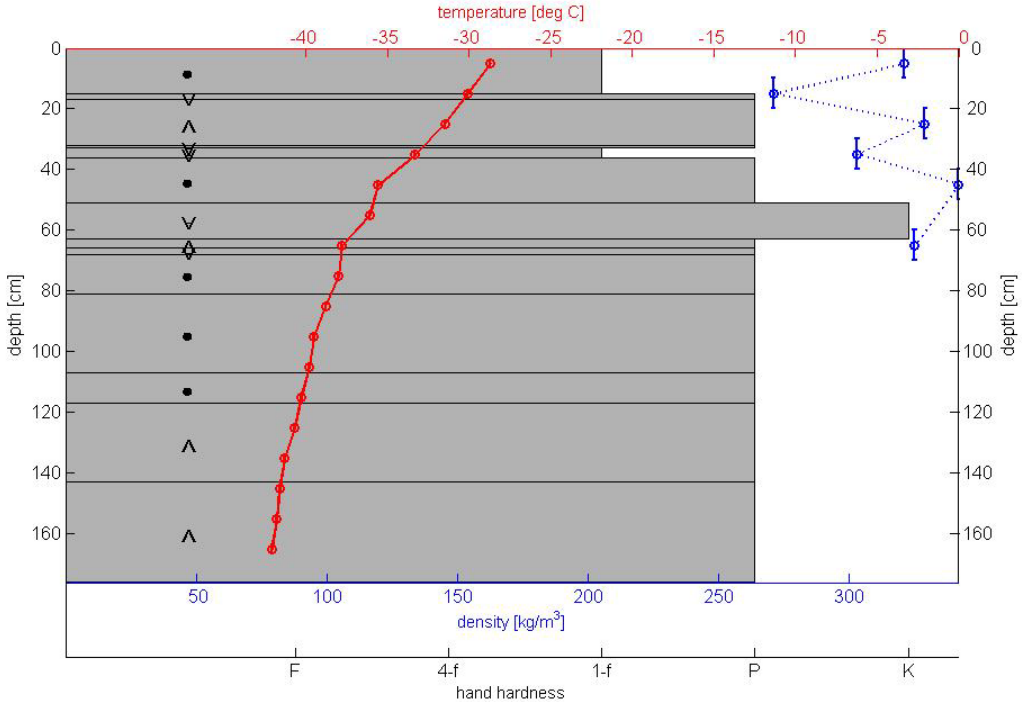

Figure 4.6 Snow pit profile of AP0601 at Taylor Dome, Antarctica, showing firn stratigraphy at one point near the TD1, TD2, TD3 and TD4 radar profiles. The solid line is the temperature corresponding to the top x-axis and the dash line is the density corresponding to the bottom x-axis. The height of the gray rectangle represents the layer thickness and depth given on the y-axis and the length represents the hand hardness of the layer given on the bottom x-axis. The symbols represent the grain type as defined by the international classification of seasonal snow [*Colbeck et al.,* 1990].

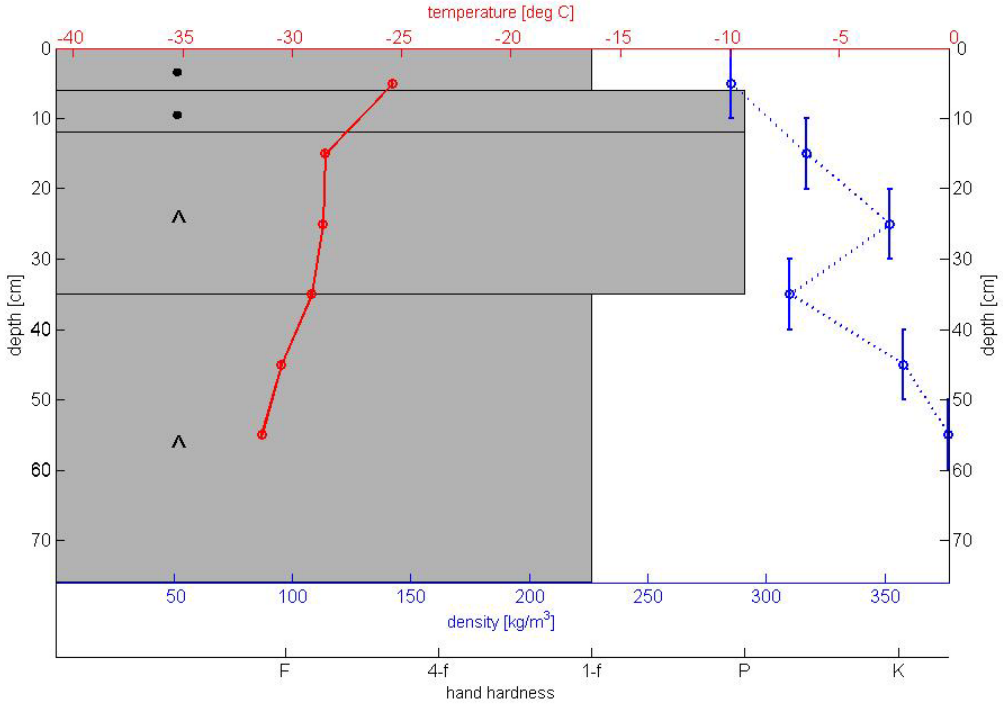

Figure 4.7 Snow pit profile of AP0602 in East Antarctica, showing firn stratigraphy at one point near the AP0602 radar profile. The solid line is the temperature corresponding to the top x-axis and the dash line is the density corresponding to the bottom x-axis. The height of the gray rectangle represents the layer thickness and depth given on the y-axis and the length represents the hand hardness of the layer given on the bottom x-axis. The symbols represent the grain type as defined by the international classification of seasonal snow [*Colbeck et al.,* 1990].

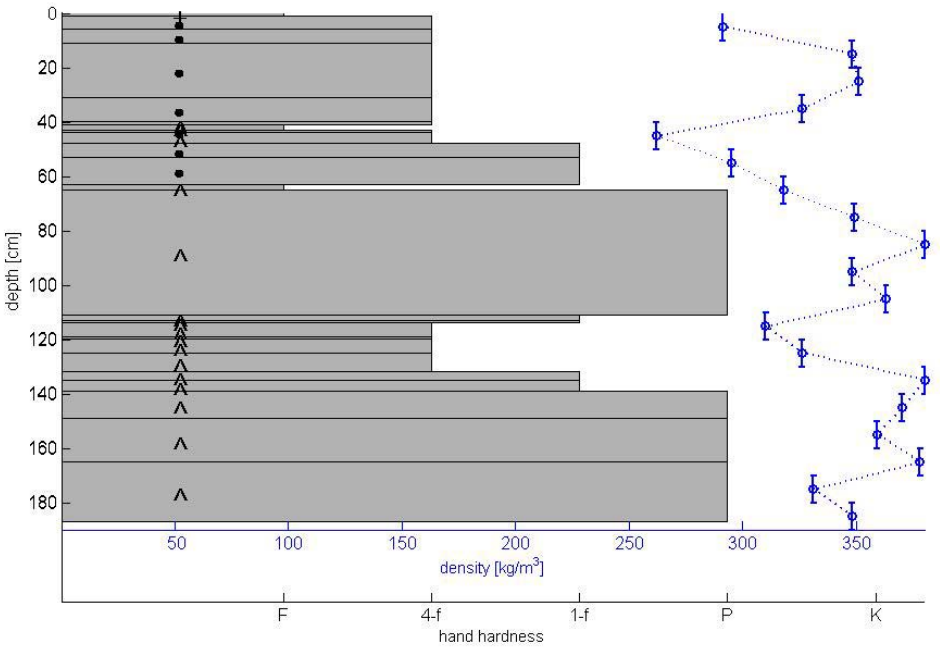

Figure 4.8 Snow pit profile of Summit pit 07-2 showing firn stratigraphy at one point near the Summit pit 07-2 radar profile. The solid line is the temperature corresponding to the top x-axis and the dash line is the density corresponding to the bottom x-axis. The height of the gray rectangle represents the layer thickness and depth given on the y-axis and the length represents the hand hardness of the layer given on the bottom x-axis. The symbols represent the grain type as defined by the international classification of seasonal snow [*Colbeck et al.*, 1990].

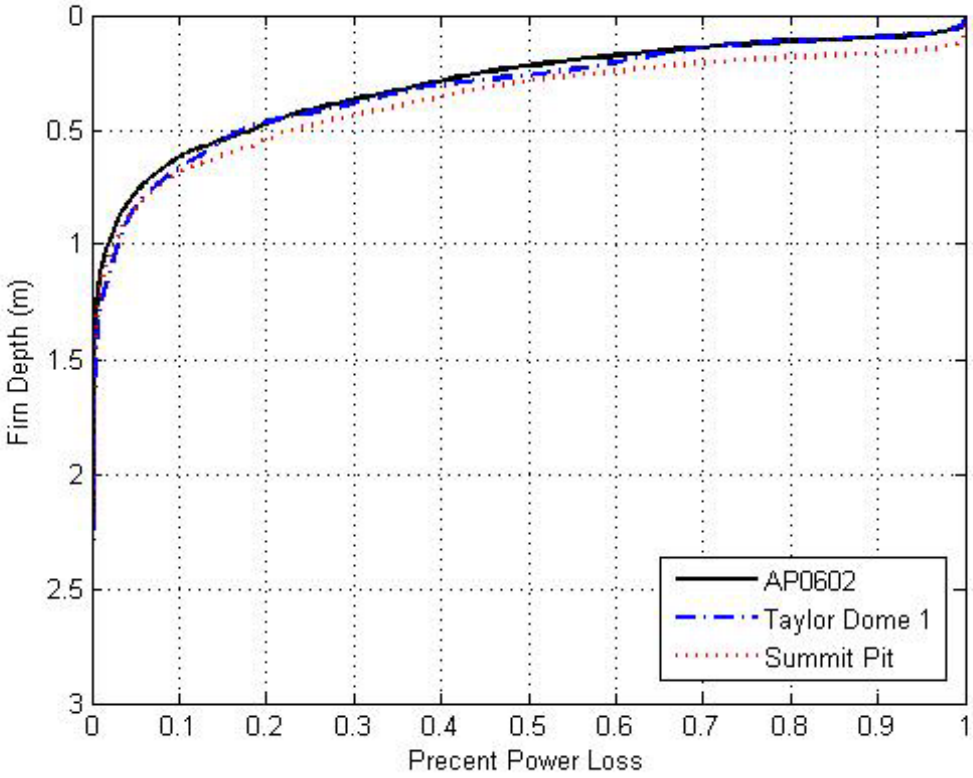

Figure 4.9 Curves of percent power loss used to estimate the extinction coefficient at each field site.

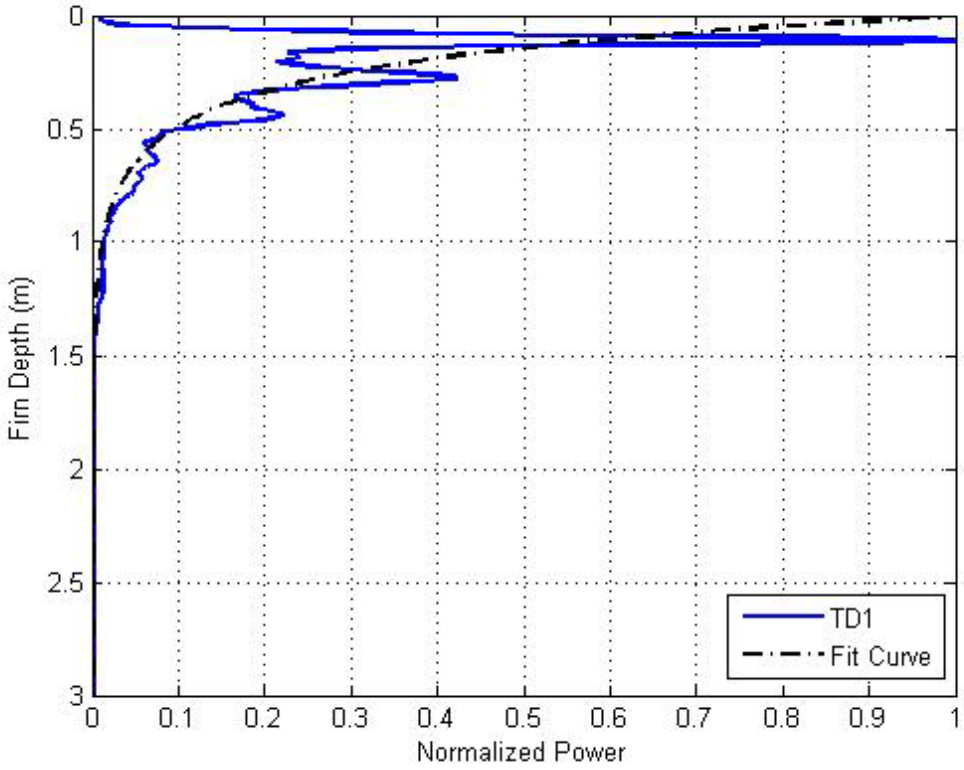

Figure 4.10 Fitted-extinction-coefficient curve for TD1 profile.

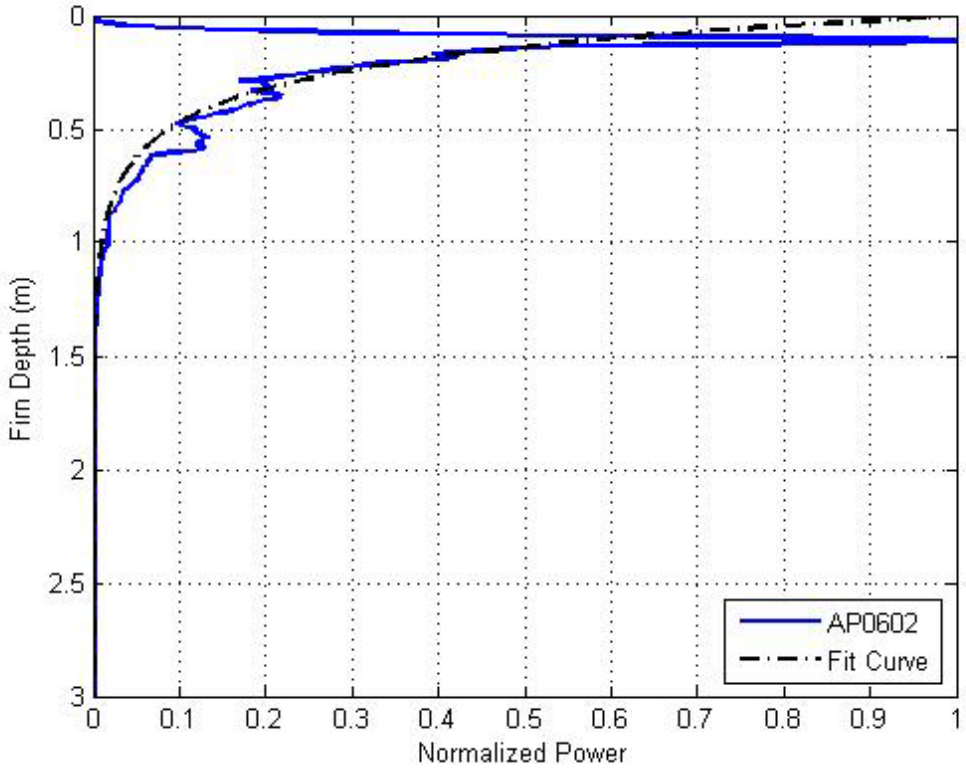

Figure 4.11 Fitted-extinction-coefficient curve for AP0602 profile

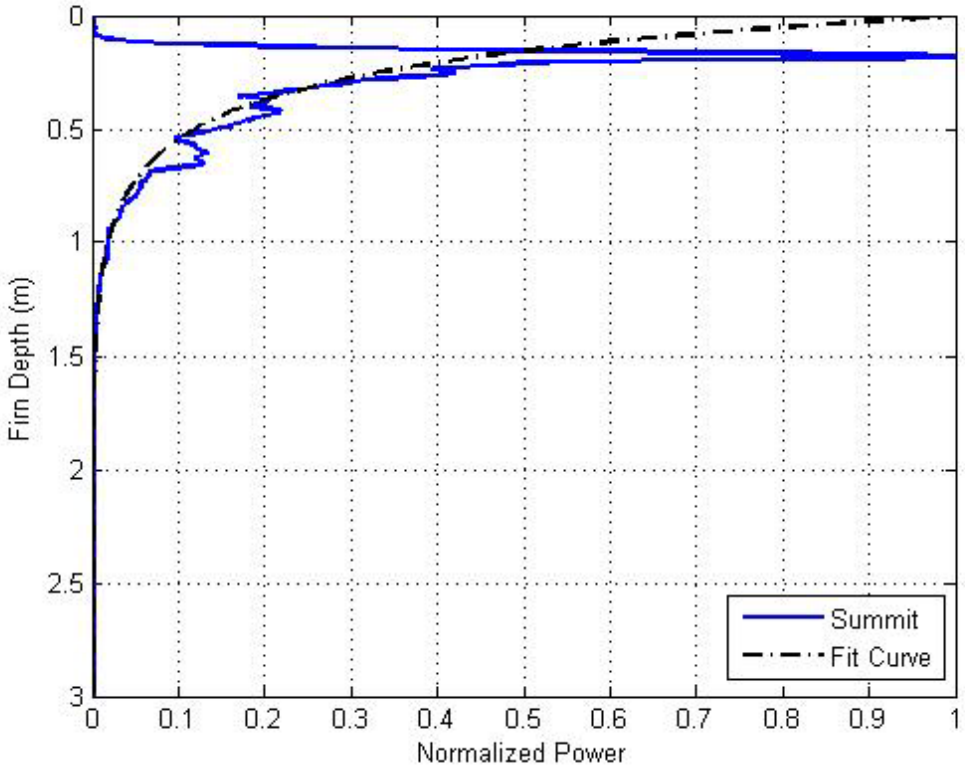

Figure 4.12 Fitted-extinction-coefficient curve for Summit pit 07-2 profile

Table 4.1 Summary of the extinction coefficient, extinction length, root mean square error of the fitted curve to the mean percent-power curve, length of profile and the accumulation rate at each site .

Profile	k_e (1/m)	L (m)	RMSE	Length (m)	Accumulation (cm weq/yr)
AP0602	1.64	0.61	0.01	56	~7-9[1]
TD1	1.55	0.64	0.02	160	7-9[2]
TD2	1.53	0.65	0.02	160	7-9
TD3	1.49	0.67	0.02	320	7-9
TD4	1.48	0.68	0.02	320	7-9
Summit pit 07-2	1.33	0.75	0.03	30	25[3]

1 *Vaughan et al.,* 1999
2 Morse et al., 1999
3 *Dibb and Fahnestock,* 2004

percent-power-loss curves. Better fits are obtained with the Antarctic data, where the peak return is closer to the surface.

These results allow comparisons of extinction lengths at sites where only radar-profile data are available. The estimated extinction length at Taylor Dome is 0.66 m, at AP0602 it is 0.61 m and at Summit, Greenland it is 0.75 m. East Antarctic extinction lengths are ~ 15% shorter than those measured at Summit.

The radar-profile-derived extinction length at Summit in 2007 is 0.75 m, which is about half the length of that measured by radiometer in 2006 (~1.6 m). As expected, the radar-profile method underestimates the extinction length, most likely because the initial power transmitted to the surface of the firn is unknown and all attenuation is not accounted for.

4.6 Conclusions

A method was presented to estimate microwave extinction lengths from radar profiles. This method is not ideal because the initial power transmitted to the firn surface is unknown, which appears to underestimate the extinction length by half of direct measurement methods. It also assumes that, over long profiles, the backscatter from individual layers is averaged out, which is not always true because firn layers can persist over the entire profile. Despite these limitations, these extinction-length estimates are useful in expanding our understanding of extinction lengths on ice sheets by giving a relative measure of extinction length that can be compared at locations where profile data already exists. Extinction lengths are ~ 15% shorter at two sites in East Antarctica than at Summit Greenland. The extinction lengths from profile data at Summit, Greenland are ~50% shorter than more reliably-measured values. Extinction-length estimation should be used at additional ice-sheet sites where only radar profiles exist to gain a better understanding of how extinction lengths vary with firn microstructure, stratigraphy and accumulation rate.

Chapter 5

THERMAL CONDUCTIVITY MEASUREMENTS OF POLAR FIRN

5.1 Summary

The extinction-diffusion time model for microwave emission established a link between microwave extinction length, firn thermal diffusivity and accumulation rate. Here, firn thermal diffusivity calculations are presented from measurements of thermal conductivity, density and temperature at ice sheet locations with different accumulation rates. Firn thermal diffusivity is a function of the thermal conductivity, density and specific heat, which is dependent on temperature. The relative dearth of thermal conductivity measurements, both in general and with firn depth, motivated the acquisition of a new thermal conductivity data set of polar firn. 118 new thermal conductivities were measured in total at 9 locations in Greenland and 4 locations in East Antarctica. The measurements were taken in the top two meters of firn. Thermal conductivity measurements show no correlation with depth in the top ~2 meters of firn; they are minimally correlated with density and more strongly correlated with a qualitative measurement of grain bonding, the hand hardness test. Thermal conductivities ranged from 0.044 to 0.342 W/mK.

5.2 Introduction

The extinction-diffusion time model for microwave emission is an improved model for simulating passive microwave brightness temperatures and may provide a tool to monitor accumulation rates on the polar ice sheets [*Winebrenner et al.,* 2004*; Koenig et al.,* 2007]. To investigate the utility of the extinction-diffusion time model, variations in the model time scale are compared to field measurements. The characteristic time scale, the extinction-diffusion time, is defined as the microwave extinction length squared divided by the thermal diffusivity of the firn. Methods and results for field measurements of the microwave extinction length are presented in Chapter 3 and 4. This chapter investigates the second component of the extinction-diffusion time by calculating firn thermal diffusivities at sites with different accumulation rates which are used to investigate variation between thermal diffusivities and accumulation rate in Chapter 6.

A thermal diffusivity measurement involves taking field measurements of the firn's thermal conductivity, density and temperature. Thermal conductivity measurements, in general and with depth in the firn, are scarce on ice sheets and additional measurements are needed to understand variations in thermal diffusivity with accumulation. Comparing variations in thermal diffusivity to passive microwave remote sensing requires that the thermal conductivity measurements be made to a depth in the firn commensurate with the microwave extinction length. For the 37 GHz

passive microwave channel it is necessary to measure thermal conductivity to a depth of approximately 1.5 m.

5.3 Background

Firn is not an isothermal material; it has a temperature profile which records information about past temperatures. The temperature profile in firn controls the initial microwave radiation emitted, before it is scattered and absorbed. Field investigations were conducted to better characterize the transfer of heat from air surface temperatures into the firn temperature profile to characterize emitted microwave radiation. The vertical temperature profile in polar firn, to first order, is determined by the heat diffusion equation:

$$\frac{\partial T}{\partial t} = K \frac{\partial^2 T}{\partial z^2}, \tag{5.1}$$

where T is the temperature, t is time, z is the depth into the firn and K is the thermal diffusivity. Heat can also be transferred into the top few meters of polar firn by advection (which includes wind pumping) and radiation, however, these are secondary effects to conduction with accounts for 92% of heat transfer in polar firn, as shown by *Brant and Warren* [1993; 1997] at the South Pole. The transfer of heat from radiation and advection are not included in the extinction-diffusion time model for microwave emission and will be neglected here in the heat transfer equations. Thermal diffusivity is defined as:

$$K = \frac{k}{\rho c}, \qquad (5.2)$$

where k is the thermal conductivity, ρ is the density and c is the specific heat.

The specific heat of firn is determined by using the density of the firn to determine the percentage of ice and air in the firn. The specific heat of the firn is calculated by the summation of the specific heat of ice multiplied by the percentage of ice with the specific heat of air multiplied by the percentage of air in the firn. The specific heat of air is not temperature dependant at ice sheet temperature and is taken to be 1005 J/kgK. The specific heat of ice is temperature dependant at ice sheet temperatures and given by the empirically derived formula:

$$c_{ice} = 152.5 + 7.122\ T \qquad (5.3)$$

[*Paterson*, 1994].

The effective thermal conductivity of snow k_{eff} is related to the heat flux by:

$$F = -k_{eff}\frac{dT}{dz}, \qquad (5.4)$$

where F is the vertical heat flux, T is the temperature and z is the depth.

5.3.1 Previous measurements

Thermal conductivity measurements in snow and firn have been conducted using a variety of techniques and instruments summarized by *Sturm* [1997; *Sturm et al.* 2002]. Needle probes have been used for 30 years and are commonly used today to measure thermal conductivity in firn and soils. Needle probes have been shown to

be one of the best methods for measuring thermal conductivities in granular materials with low conductivities [*Jackson and Taylor,* 1986; *Sturm and Johnson*, 1992; *Sturm,* 1997; *Sturm et al.,* 2002]. A heated needle probe will be used in this study to measure thermal conductivities (see section 5.4 for specific details of probe).

Thermal conductivity measurements in firn are less common than measurements in seasonal snow. *Sturm et al.* [1997] compiled a comprehensive review of thermal conductivity measurements and only 33 of the 354 measurements were taken in firn. No thermal conductivity measurements in *Sturm et al.*'s compilation were related to firn depth. Table 5.1 summarizes thermal conductivity measurements from ice sheets.

Table 5.1 Summary of thermal conductivity measurements on Ice Sheets

Study	Location	# of Obs.	Mean Thermal Conductivity (W/mK)
Weller and Schwerdtfeger, 1971	Antarctica Plateau	2	0.81
Lange, 1985	Flichner-Ronne Ice Shelf	31	0.33
Brandt and Warren,1997	South Pole, Antarctica	Numerous	0.28
Courville et al., 2007	Megadunes, Antarctica	36	0.24
Courville and Albert, personal communication	Summit, Greenland	10	0.09
This Study	Swiss Camp, Greenland	32	0.19
This Study	Summit, Greenland	62	0.11
This Study	Antarctica	24	0.12

Brandt and Warren [1997] conducted a thorough experiment on heat fluxes in the firn at South Pole Station, Antarctica. In *Brandt and Warren*'s study they placed 10 thermistors horizontally in the firn from the surface to a depth of 3 meters. They recorded temperatures continuously over a 10 month period. These temperatures were compared with finite difference temperature models to calculate the thermal conductivity. Their study also investigated heat transfer by means other than conduction, mainly advection by wind pumping and solar radiative heating. The study found that 92% of the vertical and horizontal temperature record was due to conduction at the South Pole. Thermal conductivity was calculated at 4 different snow depths in this study. Thermal conductivity at the 4 points increased with depth. [*Brandt and Warren*, 1997]. Density was the only firn property measurements given in this study and was measured once in January and then again in December, 1992. The linear density fit in the top 2 meters of firn increased from 340 kg/m^3 at the surface to 390 kg/m^3at 2 meters. The location of the South Pole study is unfortunate for satellite remote sensing because it falls in the satellite polar hole, outside the swath width of most satellite sensors.

Courville et al. [2007] and *Courville and Albert* [personal communication] measured thermal conductivity at two snow pit locations in the megadunes region of East Antarctica and at a pit at Summit, Greenland, respectively. These studies used a heated needle probe to measure the thermal conductivity in firn cores that were extracted from pits and placed in an insulated box, thus removing the firn from the

wind and insuring that no heat transfer took place due to advection or wind pumping. Wind pumping or advection of heat away from the needle probe during a measurement could cause an error in thermal conductivity measurement that would result in a lower measured value. (The needle probe technique and errors are described in more detail in section 5.4.)

The *Courville et al.* [2007] study compared firn properties at a wind scoured face (less accumulation) to a wind depositional face (more accumulation) in the megadunes region. Thermal conductivity was shown to be higher at the site with less accumulation than at the site with more accumulation, though both sites had extremely low accumulation rates.

Thermal conductivity was measured with depth in the *Courville et al.* [2007] and *Courville and Albert* [personal communication] studies. In East Antarctica measurements were taken to a depth of approximately 3.5 m and at Summit, Greenland to a depth of 2 m. There was no apparent correlation between thermal conductivity and depth in this high resolution data, with measurements taken approximately every 15 cm, which is in contrast to the coarser resolution *Brandt and Warren* data that suggested an increase in thermal conductivity with depth.

5.4 Methods

The following methods were employed to acquire a thermal conductivity data set with the depth range and spatial extent necessary for comparison with satellite

data. Thermal conductivity measurements were taken every 10 cm in numerous snow pits in Antarctica and Greenland with a heated needle thermal conductivity probe. The University of Washington's thermal conductivity probe was constructed by Thermal Logic in Pullman, Washington. The probe length is 200 mm. The heating element in the probe is 60 mm and is located at the end of the probe; therefore the distal 60 mm of the probe are heated. One of the heater wires is connected to a precision reference resistor which is used to measure the heating current. The power input and temperature rise during a 2 minute heating cycle are used to calculate the thermal conductivity. The effective thermal conductivity is calculated using:

$$k_{eff} \approx \frac{q_n}{4\pi\Delta T} \ln(\Delta t), \qquad (5.5)$$

where ΔT is the change in temperature, Δt is the change in time, q_n is the heat produced in the needle per unit length and unit time which is equal to $V^2 / L_n r$ where V is the input voltage for the heating cycle, L_n is the length of the heated needle and r is the heater wire resistance per unit length [*Jackson and Taylor,* 1986; *Sturm et al.* 2002].

The probe measures the temperature rise in the firn with a Type E, constantan-chromel, thermocouple located 30 mm from the end of the probe in the center of the heating element. The probe measures conductivity in approximately a 5 cm sphere surrounding the probe.

The thermal conductivity probe is inserted into a pit wall starting 5 cm from the top of the pit and measurements are taken every 10 cm from the top of the pit to the bottom. Two thermocouples are inserted 10 cm away from the probe, one on each side of the probe, forming a horizontal line. The thermocouples are used to monitor temperature and heat flow not related to the thermal conductivity probe. Stable temperatures at the thermocouples are required for a good measurement. The temperature rise and power input data are fitted using equation 5.5 to calculate the thermal conductivity. If the root mean square error (RMSE) of the fit of equation 5.5 to the data is beyond a certain threshold the measurement is considered bad and thrown out following methods of *Albert* [personal communication].

In addition, approximately 10 valid thermal conductivity measurements were eliminated from the data set analyzed in this chapter because the corresponding density, temperature or grain size measurement was missing. For example, if a valid thermal conductivity measurement was made but no corresponding density measurement was available, the conductivity measurement was not used in the analysis of the thermal conductivity data set. All valid measurements are, however, included in individual pit averages and thermal diffusivity calculations, leading to small differences when comparing pit averages containing all valid measurements to pit averages derived from the more exclusive thermal conductivity data set. (The differences are small and evident when comparing Table 5.3 to 5.5.)

The measurements in this study were taken in an open snow pit face, therefore, the measurements are exposed to natural wind pumping, or advection of heat, that occurs within firn. Because the measurements are taken directly in the pit, as opposed to removing the samples and isolating them from the wind in a lab or box, they are subject to the errors associated with the advection of heat away from the needle probe that is not accounted for in the conduction calculations. This additional heat loss would result in an underestimation of the thermal conductivity value. A comparison of open pit thermal conductivity measurements from this study to wind isolated measurements is preformed in the results section of this chapter (section 5.5) to quantify the errors associated with open pit measurements. It is also noted that measurements are not taken on extremely windy days because the instrument electronics cannot be used when there is blowing snow, which should minimize errors associated with wind pumping.

Temperature and density are additionally needed in order to calculate the thermal diffusivity using equations 5.2 and 5.3. Temperature was measured in the firn using a thermocouple and density was measured using a standard 1000 cm^3 wedge density cuter. Typical errors on densities using a wedge cutter are estimated a 10% [*Conway and Wilbur,* 1999; *Perla*, 1978].

Measurements were made at multiple pits at two locations on the Greenland Ice Sheet, Swiss Camp and Summit (Figure 5.1), as well as 4 sites in East Antarctica (Figure 5.2). The sites in East Antarctica follow the US ITASE traverse route. See

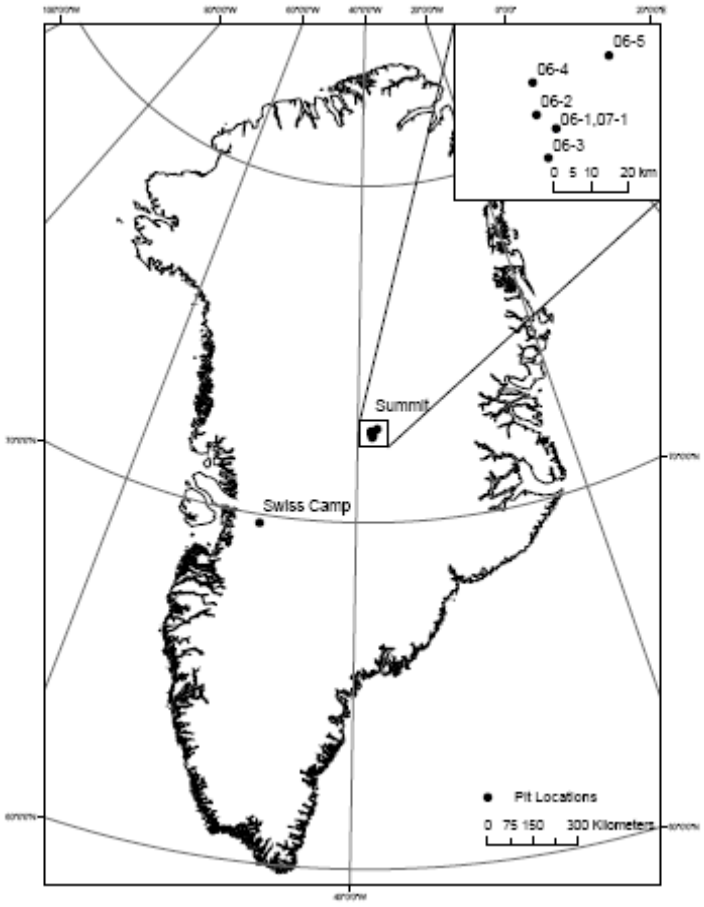

Figure 5.1 Locations of Greenland pits

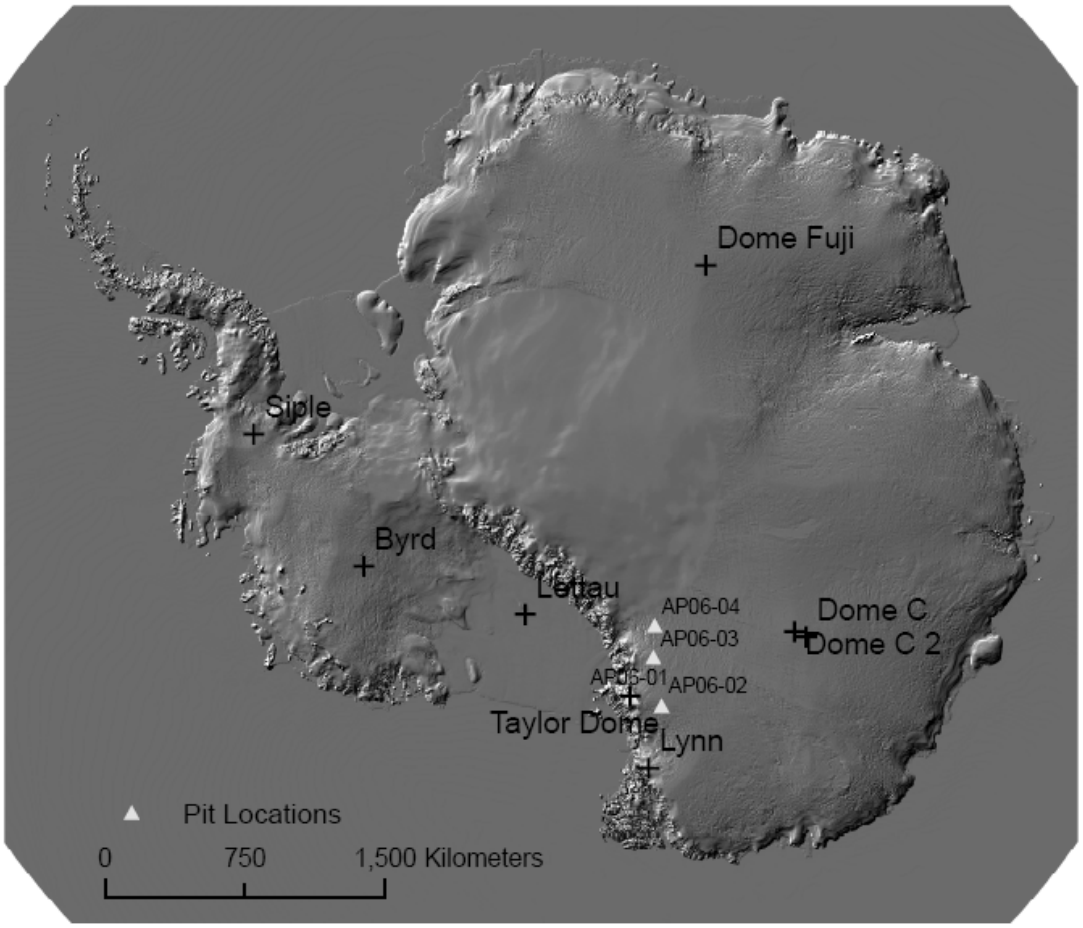

Figure 5.2 Locations of Antarctic pits.

Appendix A-C for exact pit locations and the specific thermal conductivity and microstructure data at each pit.

5.5 Results and Discussion

Figure 5.3 shows a scatter plot of thermal conductivity measurements and density demarcated by location. The measurements taken at Swiss Camp, where the mean density is higher than other sites as shown in Table 5.2, clusters above the other measurements. Swiss Camp is located at the equilibrium line of the Greenland ice sheet where snow experiences melt. The measurements from Summit, Greenland, labeled Summit, and the East Antarctic Plateau, labeled Antarctica, cluster together with similar thermal conductivities and density ranges. The Summit and Antarctica measurements were taken in the dry-snow zone where no melting occurs. One outlier in the Antarctic data set stands out as much higher than the rest. This measurement is most likely explained by the hard snow layer that the measurement was taken in, which signifies well bonded snow, shown in Figures C.1 and C.2 in Appendix C.

5.5.1 Regression equations

The thermal conductivity data was analyzed to fit with a regression equation. Inspection of the scatter plot (Figure 5.3) suggests a linear fit for the Summit and Antarctica datasets and a quadratic fit for the Swiss Camp dataset. Upon calculating linear correlation coefficients it was found that only the Summit thermal conductivity

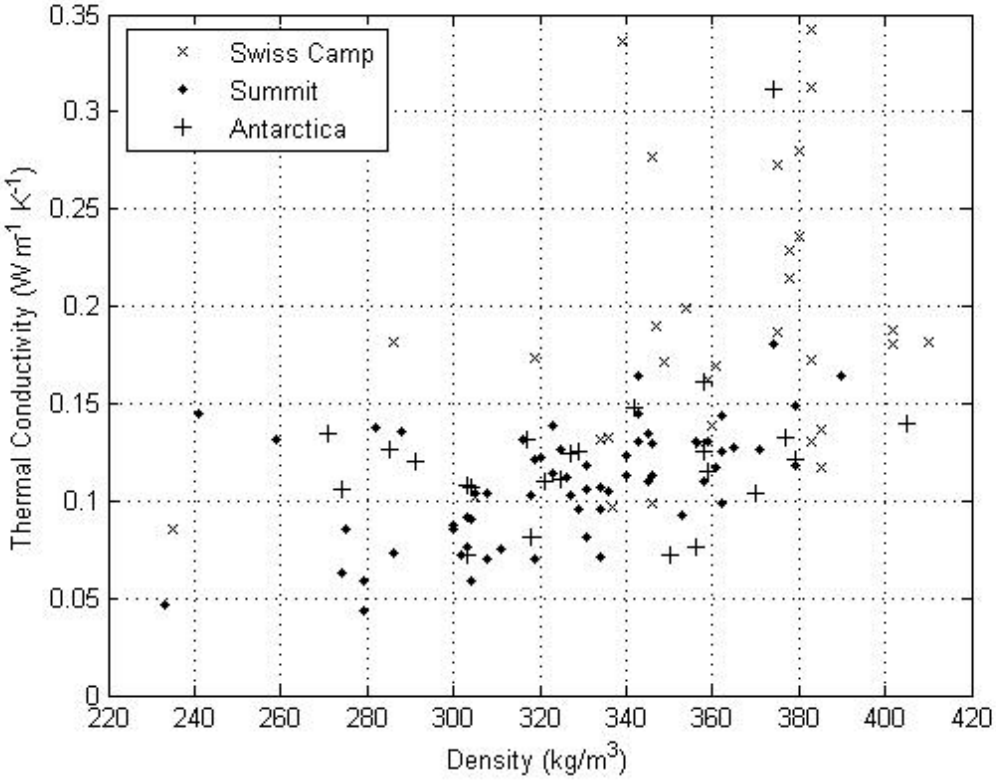

Figure 5.3 Scatter plot of thermal conductivity measurements to density. Measurements are demarcated by location. The Swiss Camp data cluster above the data from the dry-snow zone.

Table 5.2 Mean values for the thermal conductivity data set at each ice sheet location.

Location	Mean Temp (C)	Mean Depth (cm)	Mean Density (Kg/m^3)	Mean Grain Size (mm)	Mean Thermal Conductivity (W/mK)
Swiss Camp	-8.4	55	358	0.4	0.19
Summit	-26.3	66	325	0.8	0.11
Antarctica	-29.0	37	333	1.2	0.12

measurements had a statistically significant correlation with density at the 99% confidence interval. The samples sizes at the other locations are too small to obtain statistical significance with a linear fit. The Antarctic data was grouped with the Summit data to represent thermal conductivity measurements in dry polar firn. Combining these data sets increases the sample size and allows for a statically significant linear regression to be calculated.

Least squares linear regression was used to derive equations for the Summit and Summit/Antarctica thermal conductivity data. The regression equation for Summit is:

$$k_{eff} = 0.463\rho - 0.042, \qquad (5.5)$$

for ρ units of g/cm^3 and k_{eff} units of W/mK . The Summit regression equation has a very low coefficient of determination, adjusted $r^2 = 0.26$, meaning that only 26 % of the variance is explained by the linear equation.

The regression equation for the Summit and Antarctic data, or the dry polar firn is:

$$k_{eff} = 0.452\rho - 0.035, \qquad (5.6)$$

for ρ units of g/cm^3 and k_{eff} units of W/mK . The dry polar firn regression equation also has a very low coefficient of determination, adjusted $r^2 = 0.18$, meaning that only 18 % of the variance is explained by the linear equation.

The linear regression equations with density do not fit the thermal conductivity data well. This result is similar a finding by *Sturm* [1997] that density was not a good predictor of thermal conductivities in seasonal snow that contain faceted and hoar crystal. Because most crystals are facets or hoar in the top meters of firn, density is not expected to be a good predictor of thermal conductivity. A better predictor would be a measurement of grain bonding through which the heat is conducted. Nonetheless, the regression equations are presented here to show that they appear to be lower than those derived for seasonal snow and to reiterate that density is not a good predictor of thermal conductivity on ice sheets (Figure5.4).

5.5.2 Thermal conductivity variations with depth and stratigraphy

A main objective for collecting the thermal conductivity data in this study was to determine if thermal conductivity was correlated to depth in the top meters of polar firn. No statistically significant correlation was found between thermal conductivity and firn depth in the measurements presented here. Figure 5.5 shows a scatter plot of thermal conductivity with depth illustrating the lack of correlation.

Figure 5.6 shows a scatter plot of thermal conductivity to grain size. There appears to be a decrease in conductivity with increased grain size, however, no

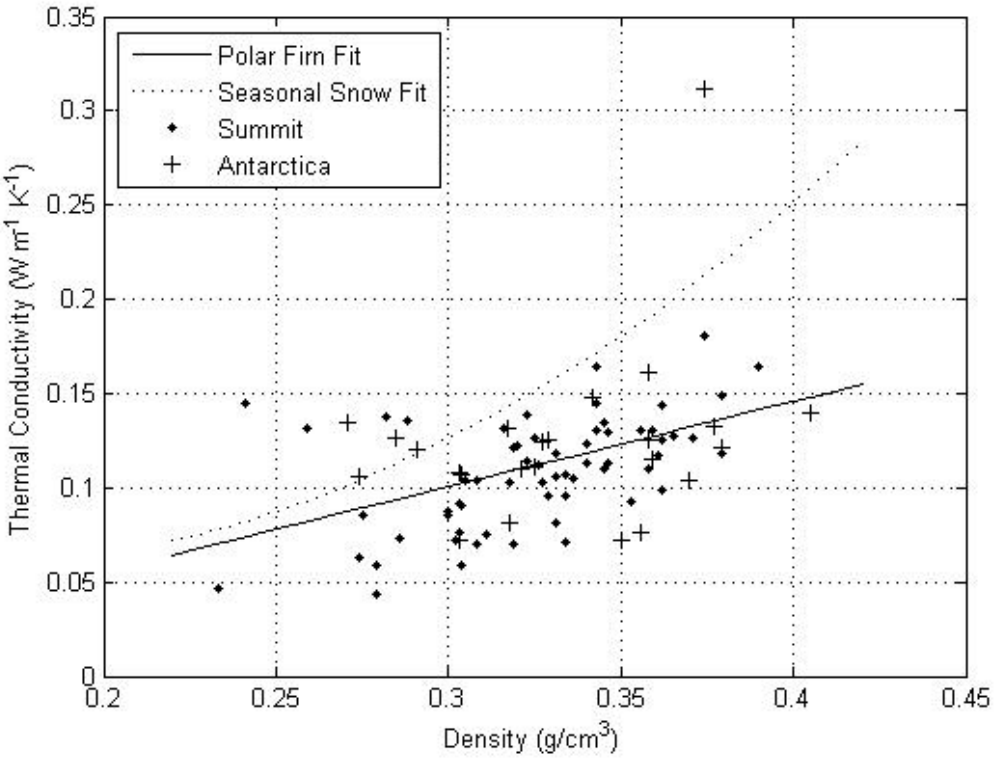

Figure 5.4 Scatter plot of density to thermal conductivity showing the fit line from the Summit and Antarcitica data (Polar Firn) and the regression equation given by *Sturm et al.* [1997] for seasonal snow. The Polar Firn equation is lower than that predicted by the seasonal snow equation.

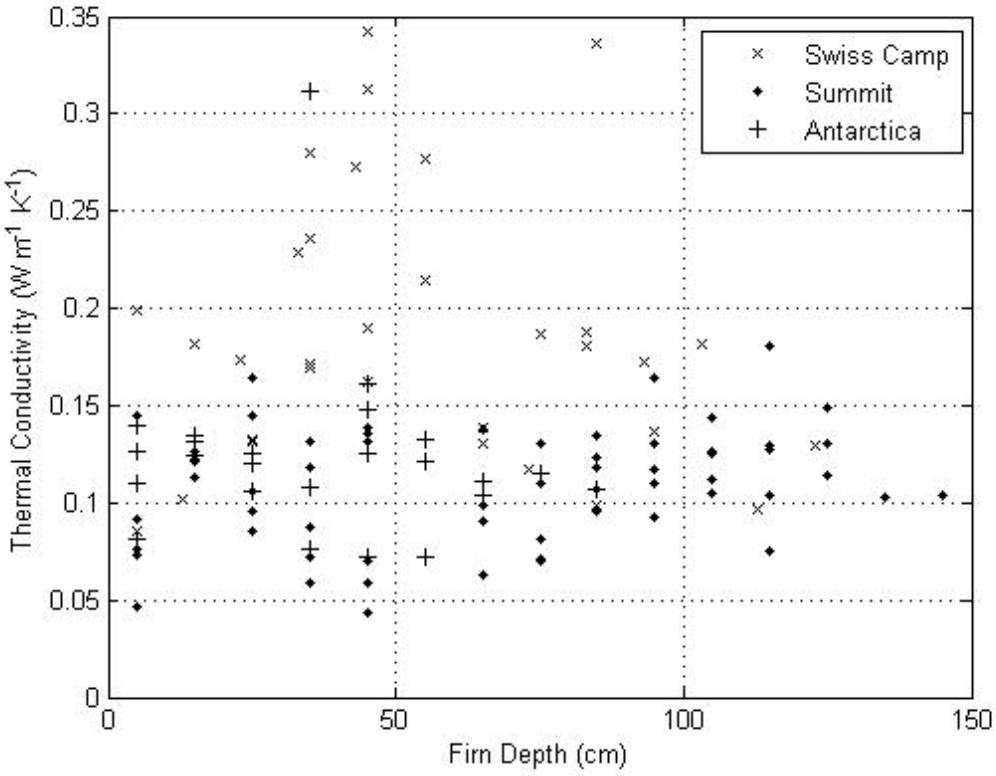

Figure 5.5 Scatter plot of thermal conductivity measurements to firn depth where the measurement was taken showing no correlation with depth.

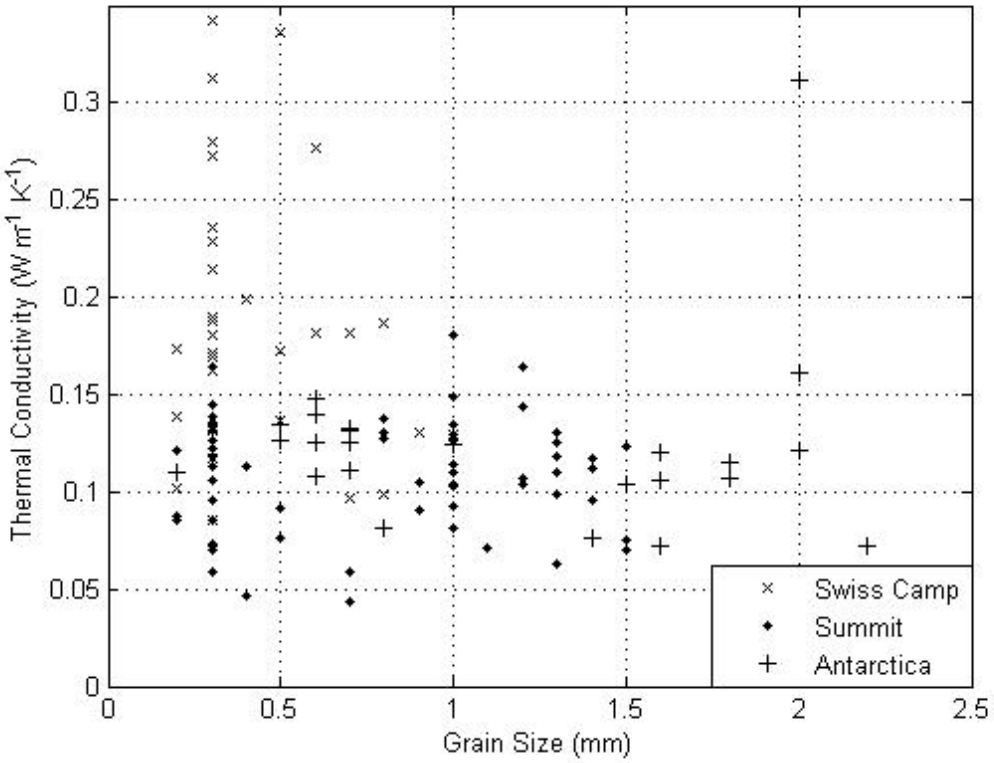

Figure 5.6 Scatter plot of thermal conductivity measurements with grain size showing no correlation with grain size.

statistically significance trend was found. In seasonal snow it has been shown that hoar crystals have a lower thermal conductivity than other snow grain types [*Sturm and Johnson*, 1992]. While the kinetically-grown large faceted crystals in polar firn are not the same as the hoar in seasonal snow, they nevertheless have a directionality and faceted nature that are consistent with the expectation of a lower thermal conductivity. All stratigraphy information, grain size, temperature, and density, was investigated as possible independent variables for a regression equation for thermal conductivity. Only density was found to be a statistically significant independent variable to determine individual thermal conductivity measurements but still had a very low coefficient of determination.

5.5.3 Comparison with other data

The thermal conductivity measurements taken in this study at Summit, Greenland in 2006 were compared to similar measurements taken by Courville and Albert [personal communication] at Summit, Greenland in 2006. The measurements from the two studies were taken in different pits at Summit and the measurements in this study were taken in mid-June approximately 3 weeks earlier than those by Courville and Albert taken in July. Courville and Albert's methods were slightly different from those in this study; Courville and Albert extracted firn cores from the pit and placed them in an insolated box protecting the sample from the wind. This method reduces errors in the measurements from wind pumping or advection of heat

away from the needle probe which can cause an underestimation of the thermal conductivity measurement.

The open pit measurements from this study was compared to the Courville and Albert measurements to see if the open pit measurements were statistically different from the wind isolated measurements. Student's t tests were conducted at a 0.05 significance level to test if the means of the samples were statistically different. The mean of the Courville and Albert data is 0.09 W/mK and the mean from this study is 0.11 W/mK. The means are not statistically different at a 0.05 significance level with a p-value of 0.09 and a t-stat(df=70) of 1.73. Additionally the mean of the pit data is higher than the wind isolated data which is opposite of the expected error if wind pumping was affecting the open pit measurements.

An additional test comparing the two data sets looks at the 95% confidence interval around the mean of each study. The 95% confidence interval for the Courville and Albert data, where the sample size n=10, is 0.08 to 0.11 W/mK and the 95% confidence interval for the data from this study at Summit, where n= 62, is 0.10 to 0.12 W/mK. The overlap in the confidence interval implies that the means are not significantly different. Comparison of the Courville and Albert wind isolated thermal conductivity measurements to the open pit measurements taken in this study implies that the errors associated with wind pumping were negligible at Summit.

T-tests were additionally performed to compare the means at all the Summit, Greenland pits. Table 5.3 shows the mean thermal conductivities and densities at each

pit. Summit pit 06-3 was the only pit that had a significantly different mean at a 0.05 significance level from all of the rest of the pit means, expect pit 06-2. Table 5.4 shows the p-values for t-test between each pit. The p-value or probability value is the probability of getting a test statistic at least as extreme as the calculated one from the sample data, assuming that the null hypothesis that the means of the two samples are the same is true. It is standard procedure to reject the null hypothesis if the p-value is less than 0.05.

Table 5.3 Mean Thermal Conductivity by Pit

Pit	Mean Density* (kg/m^3)	Mean Thermal Conductivity* (W/mK)
Courville and Albert	324	0.09
Summit 06-1	311	0.10
Summit 06-2	334	0.11
Summit 06-3	331	0.13
Summit 06-4	316	0.10
Summit 06-5	328	0.10

*This is the mean density and thermal conductivity at points where measurements of thermal conductivity, density and grain size were all measured. These means are slightly different than the pit averages as reported in Table 5.5 and is explained in section 5.3.

Table 5.4 P-values of T-test comparing pit means

	C and A	06-1	06-2	06-3	06-4	06-5
C and A	1.00	0.33	0.14	0.00	0.45	0.67
06-1	0.33	1.00	0.59	0.02	0.75	0.54
06-2	0.14	0.59	1.00	0.10	0.38	0.24
06-3	0.00	0.02	0.10	1.00	0.01	0.00
06-4	0.45	0.75	0.38	0.01	1.00	0.74
06-5	0.67	0.54	0.24	0.00	0.74	1.00

Density means were examined to explain why Summit pit 06-3 had a significantly higher mean thermal conductivity. Pit 06-3 did have the second highest density mean, however, none of the density means were statistically different from each other. And from previous results it was shown that density was not a good predictor of thermal conductivity in firn. Density cannot explain the higher thermal conductivity at Summit pit 06-3 but stratigraphy can.

Pit stratigraphy and hand hardness, a qualitative measurement of grain bonding, were compared between the Summit pits to explain the higher value at pit 06-3. The grain types found in Summit pit 06-3 starts to explain the higher thermal conductivity. The stratigraphy, shown in Appendix B Figure B.7, for pit 06-3 is different from the other pits, it has more rounded crystals. There are approximately 80 cm of layers containing rounded crystals in pit 06-3 where as the other pits have 20 cm or less of rounded crystals. This means that as a percentage pit 06-3 has about 40% rounded crystals where the other pits have 15% or less rounded crystals with the remaining crystals mainly facets or hoar crystals. Rounded crystals, form in a weaker temperature gradient and have, in general, a higher degree of bonding than the faceted or hoar crystals, which form in large temperature gradients where high vapor transport leads to kinetic grain growth [*Sturm*, 1997]. The larger amount of rounded crystals over faceted or hoar crystals suggests a higher degree of bonding and is a plausible explanation for the increase in thermal conductivity at pit 06-3.

Additionally the hand hardness test, which is a qualitative test of grain bonding, shows that pit 06-3 had the highest mean hand hardness of 3.4 for Summit (Table 5.5). This number should not be taken quantitatively; it is calculated by assigning a number to each hand hardness classification group with 1 being prescribed to the weakest category, fist, and a 5 being assigned to the hardest category, knife. This numbering allows for a way to compare the hardness between pits with higher number representing qualitatively harder firn. It is likely that Summit pit 06-3's higher thermal conductivity value is explained by the fact that the firn was hardest and contained more rounded crystals both pointing to relatively well bonded firn at this location.

The mean hand hardness was compared to the mean thermal conductivity at pits in both Antarctica and Greenland (Figure 5.7). This comparison can only be made between pits because the hand hardness measurement is taken at a larger scale than the 10 cm individual thermal conductivity measurements. There is a linear relation ship between the mean hand hardness value and the mean thermal conductivity with r^2=0.74. This correlation warrants further investigation where thermal conductivity measurements are compared to a more quantitative measurement of grain bonding at a smaller scale, like those from a snow micro-penetrometer. Figure 5.7 supports evidence that the degree of bonding will be the best predictor of thermal conductivity not the density, which supports previous findings by *Sturm* [1997, *Sturm et al.* 2002].

There is no way to directly compare the Antarctic thermal conductivity data from this study to other thermal conductivity data taken in Antarctica, specifically to the *Brandt and Warren* [1997] and *Courville et al*., [2007] measurements because they are too far separated in space and time. It is noted that the thermal conductivity measurements from this study taken in East Antarctica near Taylor Dome are about half of that measured by the other studies. Some of this difference could be attributed to errors associated with taking the measurements in an open pit, though the Summit data showed that this error is small to negligible at that site. A likely explanation for the difference in the thermal conductivity measurements is that the firn microstructure at Taylor Dome is less bonded than that at the South Pole or megadunes region. Since no measure of grain bonding is published for the other East Antarctic thermal conductivity measurements no comparison can be conducted.

Table 5.5 Thermal diffusivities and mean values at each pit.

Pit Name	Density (kg/m^3)	Hand Hardness	Temp (°C)	Thermal Conductivity (W/mK)	Thermal Diffusivity (10^{-7} m^2/s)
Swiss Camp	357	3.7	-11.5	0.179	3.59
Summit 06-1	323	3.1	-27.7	0.103	2.45
Summit 06-2	327	3.1	-28.1	0.110	2.51
Summit 06-3	312	3.4	-27	0.129	3.00
Summit 06-4	331	2.7	-27.2	0.099	2.45
Summit 06-5	315	2.9	-26	0.096	2.22
AP0601	333	4	-37.5	0.123	3.60
AP0602	356	3.3	-28.9	0.129	2.92
AP0603	319	3.7	-27.9	0.163	3.47
AP0604	357	3	-27.1	0.092	2.17

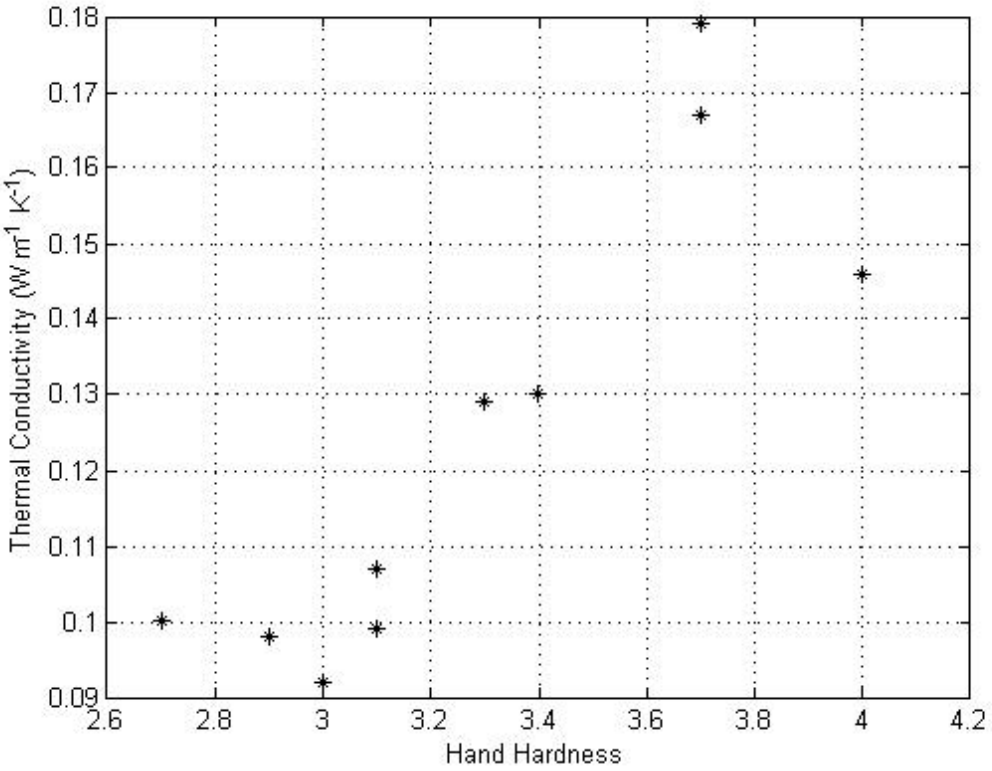

Figure 5.7 Scatter plot of hand hardness values to thermal conductivities showing a linear relation with r^2=0.74, the best correlation of any parameter with thermal conductivity.

The mean measured thermal conductivities along with the mean density and temperatures were used to calculate site specific thermal diffusivity for the Greenland and Antarctic pits. Table 5.5 shows the calculated thermal diffusivity at each site along with the density, temperature, hand hardness and thermal conductivity. The hand hardness, which was shown previously to be linearly correlated with thermal conductivity in Figure 5.7, is also linearly correlated with thermal diffusivity with r^2=0.88. This again suggests that the degree of bonding between snow grains is an important factor in determining the thermal conductivity and the thermal diffusivity in polar firn and will be one of the most important factors in determining heat transfer into firn.

5.6 Conclusions

A new dataset of thermal conductivity measurements were taken in Greenland and Antarctica with depth range to two meters. Thermal conductivities do not correlate with depth in the top few meters of polar firn. Statistically significant regression equations could be constructed using density but they only explain a small percentage, about 20%, of the variance in the thermal conductivities, showing that density is not a good predictor of thermal conductivity in firn.

At Summit, Greenland, where open pit and wind insulated thermal conductivities, taken from different pits approximately 3 weeks apart, were compared; there was no significant difference in the means of the thermal conductivity

measurements. There was a statistically significant difference in the mean thermal conductivity at one pit, Summit pit 06-3, which contained more rounded crystals and had a relatively high degree of grain bonding as shown by the hand hardness data. The average hand hardness, a qualitative measurement of grain bonding, appears to be the most significant predictor of thermal conductivity as well as thermal diffusivity at pit locations explaining 74% and 88% of the variations respectively. The hand hardness test, however, is only a qualitative measurement and additional quantitative measurement of grain bonding, such as micro-penetrometer measurements, should be taken along with thermal conductivity measurements. Results suggest that the degree of grain bonding in firn will be the most important predictor of thermal conductivity in firn.

This investigation was undertaken to understand how surface temperatures over ice sheets propagate into the firn creating a temperature profile that is recorded in the passive microwave signal. The thermal conductivities were used to calculate site specific thermal diffusivities at sites with different accumulation rates.

Chapter 6

A COMPARISON OF FIELD-CALCULATED AND SATELLITE-MODELED EXTINCTION-DIFFUSION TIMES OF MICRWOAVE EMISSION

6.1 Summary

The extinction-diffusion time model of microwave emission simulates passive microwave brightness temperature given a time series of surface temperature. This model depends on the characteristic time scale, the extinction-diffusion time of microwave emission, τ_0. τ_0, physically, is the microwave extinction length squared, adjusted for the satellite incident angle, divided by the firn thermal diffusivity and was shown to vary with accumulation rate in West Antarctica. A field investigation was conducted to measure microwave extinction lengths and firn thermal diffusivities at ice sheet locations with different accumulation rates. Field measurements at Summit, Greenland show that field-calculated τ_0's are approximately 2 times higher than satellite-modeled τ_0's. Radar-derived extinction lengths still have large uncertainties, but microwave extinction length appears to increase with accumulation rate and thermal diffusivity appears to decrease with accumulation rate at the dry-snow field locations. More precise extinction length data is needed to confirm results. Initial field investigations do not contradict nor confirm observations that τ_0 increases with increased accumulation in West Antarctica.

6.2 Introduction

Chapter 2 presented the extinction-diffusion time model of microwave emission [*Winebrenner, et al.,* 2004]. This model describes how surface temperature changes that occurred in the past, still recorded in the firn, influence current brightness temperatures through a convolution time scale, the extinction-diffusion time, τ_0. τ_0 is dependent upon firn microstructure controlling the microwave extinction length and thermal conductivity. τ_0 varies linearly with accumulation rate in West Antarctica, however, this variation does not hold over all of Antarctica [*Koenig et al.,* 2007]. The observed correlation between τ_0 and accumulation rate near Byrd Station, in West Antarctica, could be driven by changes in thermal diffusivity, in extinction length, or both.

Field investigations were undertaken to measure microwave extinction length and thermal diffusivity at sites with different accumulation rates (Chapter 3-5). Modeled results indicated West Antarctica as the ideal location for this investigation but field logistics did not allow for those measurements. Instead initial measurements were taken at sites in Greenland and East Antarctica. These sites provide initial observations on how microwave extinction lengths and thermal diffusivities vary with accumulation rate and firn microstructure. Measurements in West Antarctica will be left for future research.

The initial data allow for a comparison between the satellite-modeled τ_0's (presented in Chapter 2) and field-calculated τ_0's (calculated from data gathered in

Chapters 3 and 5) at Summit, Greenland. The data from East Antarctica are limited by errors in the radar-derived extinction length but are presented here as initial innovative data that need further refinement before making scientific conclusions.

6.3 Background

The extinction-diffusion time model of microwave emission is given by [*Winebrenner* et al., 2004, equation 9]:

$$T_B(t) = \varepsilon\overline{T} + \varepsilon\int_0^{\frac{t}{\tau_0}} T_f(t-\tau_0\tau')G(\tau')d\tau', \qquad (6.1)$$

where T_B is the microwave brightness temperature, $\overline{T}$ is the long-term (annual or longer) mean of surface temperature, ε is the time invariant emissivity, $T_f(t)=T(t)-\overline{T}$ is the fluctuating part of the surface temperature, G is the convolution kernel:

$$G(\tau') = \frac{1}{\sqrt{\pi\tau'}} - \exp(\tau')\mathrm{erfc}(\sqrt{\tau'}), \qquad (6.2)$$

erfc is the complimentary error function, and τ_0 is the characteristic time-scale of averaging over past surface temperature variations. τ_0 is referred to as the extinction-diffusion time:

$$\tau_0 = \frac{{L_\theta}^2}{K} \qquad (6.3)$$

where K is the thermal diffusivity of firn at depths commensurate with L_θ, the extinction length taking into account the satellite incident angle (also called the penetration depth) defined as:

$$L_\theta = \frac{\cos\theta}{k_e} \qquad (6.4)$$

where θ is the angle of transmission of the electromagnetic wave in the snow, using Snell's law, given the satellite incident angle from nadir and k_e is the total extinction coefficient.

To determine the extinction-diffusion time, τ_0, surface-temperature data are used to simulate passive microwave brightness temperature data for a large range of τ_0 values (see equation 6.1). The τ_0 value is determined by the optimizing the fit between simulated and observed T_B. The best fit is defined as the single minimum of the squared residuals between the fractional variation in the observed and simulated T_B's, following *Winebrenner et al.* [2004] (Figure 2.1). Uncertainty in the estimate of τ_0 is calculated by adding normally distributed random noise to the satellite T_B time series with a standard deviation of 2 K, based on the SSM/I sensor sensitivity [*Hollinger et al.*, 1990]. Typical error values are +/- 1 day.

Spatial and temporal variation in the extinction-diffusion time is expected to correlate with changes in firn properties that control firn thermal diffusivity and the microwave extinction length. Thermal diffusivity is controlled by changes in thermal conductivity, temperature and density, while extinction length in dry snow is controlled by changes in grain size, layering, and density. Thermal diffusivity will increase when thermal conductivity increases. Thermal conductivity increases when heat can travel easily through the ice lattice meaning the ice grains are well connected.

Grains that are more often found in higher accumulation areas, like rounded crystal, have been shown to have a higher thermal conductivity than grains found in lower accumulation areas, like hoar crystals, suggesting that thermal diffusivity may decrease with increased accumulation [*Sturm and Johnson*, 1992]. *Courville et al.* [2007] show further evidence of this trend from thermal conductivity and density measurements at two sites in East Antarctica, one with "high" accumulation (4.1 cm weq/yr) and the second with "low" accumulation (3.0 cm weq/yr). At these two sites the thermal diffusivity decreased with increased accumulation, consistent with the observed relationship between accumulation and τ_0.

Extinction length is also expected to correlate with accumulation because density and grain size variations from different accumulation regimes will influence the extinction length [*Gow*, 1969; *Surdyk*, 2002]. Snow grains at lower accumulation sites sit at the snow-air interface for longer periods of time relative to high accumulation sites. The low accumulation snow grains are exposed to larger temperature gradients at the snow-air interface, leading to constructive metamorphosis and hence larger snow grains. In general, extinction length will decrease as snow grain size increases; thus, extinction length should increase with accumulation rate consistent with the observed relationship between accumulation and τ_0.

6.4 Results and Discussion

Microwave extinction length and firn thermal diffusivity were measured at four ice sheet locations, Swiss Camp and Summit, Greenland and Taylor Dome (AP0601) and site AP0602, East Antarctica (Refer to Figure 5.1 and 5.2 for location maps). Table 6.1 summarizes the results listing the radiometer-measured and radar-

Table 6.1 Summary of the accumulation rate, extinction length, thermal diffusivity, satellite modeled τ_0 and field-calculated τ_0.

Location	Accum. (cm weq /yr)	37 GHz Extinction Length (L) (m)	37 GHz Satellite Penetration Depth (L_θ) (m)	Thermal Diffusivity (10^{-7} m^2/s)	Satellite-Modeled τ_0 (months)	Field-Calculated τ_0 (months)
Swiss Camp	44*1	$0.90 \pm^{?}_{0.08}$	0.54	3.59	na***	0.3±0.0
Summit 06-1	25*2	$1.79 \pm^{0.07}_{0.09}$	1.08	2.45	0.2-0.7	1.8±0.2
Summit 06-2	25	$1.59 \pm^{0.03}_{0.09}$	0.96	2.51	0.2-0.7	1.4±0.1
Summit 06-3	25	$1.67 \pm^{0.19}_{0.10}$	1.00	3.00	0.2-0.7	1.3±0.2
Summit 06-4	25	$1.52 \pm^{0.08}_{0.13}$	0.91	2.45	0.2-0.7	1.3±0.2
Summit 06-5	25	$1.56 \pm^{0.09}_{0.13}$	0.94	2.22	0.2-0.7**	1.5±0.2
Taylor Dome (AP0601)	7-9*3	0.66*	0.40	3.60	0.2	0.2
AP0602	~7-9*4	0.61*	0.37	2.92	0.1	0.2

*1 *Steffen*, personal communication
*2 *Dibb and Fahenstock*, 2004
*3 *Morse et al.*, 1999
*4 *Vaughan et al.*, 1999
* Estimated extinction length from 32-40 GHz from FMCW radar profile
** The satellite modeled τ_0 from a neighboring pixel is used. This pit is located at a pixel where ground temperature data was not available to run the model using satellite data. τ_0 has been shown to vary smoothly over Antarctica so the assumption is made that neighboring pixels will have similar τ_0's.
*** The passive microwave satellite signal for Swiss Camp contains a melt signal and cannot be used to model τ_0.

estimated 37 GHz microwave extinction length (L), the satellite penetration depth (L_θ), the firn thermal diffusivity, accumulation rate, the field-calculated and satellite-modeled τ_0's. The adjustment to penetration depth needs to be made to directly compare field-calculated and satellite-modeled τ_0's.

Swiss Camp, Greenland has the highest accumulation rate but is located at the equilibrium line of the ice sheet, where melt occurs, making the firn microstructure at this site different than at dry-snow zone sites. τ_0 can only be fit from satellite data in the dry-snow zone because liquid water, which has much higher dielectric constant than ice, dominates the passive microwave signal in wet firn. The Swiss Camp site is presented here to give a sample of extinction length and thermal diffusivity in a melt region of an ice sheet but will not be compared with the dry-snow zone sites in the following analysis.

Additionally the East Antarctic data has large uncertainties because the radar-derived extinction lengths were estimated from traverse data. These data are presented but no conclusions about τ_0 are made using these data. In the future these measurements should be retaken using the Luneberg lens method described in Chapter 3 or with a radiometer to get a better accuracy on the extinction length.

The thermal diffusivity data in East Antarctica may have some error associated with taking the thermal conductivities in an open pit where wind pumping can occur especially in low accumulation, porous firn. (Further explanation given in Section 5.4.) Wind pumping effects would lower the field-measured thermal diffusivity but no

quantitative error bar can be placed because no wind isolated measurements are available in this area. Thermal diffusivity calculations can be compared to calculations using data from the megadunes region and the South Pole to address possible errors [*Courville,* 2007; *Courville et al,* 2007; *Brandt and Warren,* 1997]. Comparing data assumes firn conditions are similar between sites, which is not entirely valid. In the top meter of firn, thermal diffusivities at 3 megadunes sites ranged from ~4.0 to $5.5*10^{-7}$ m^2/s which are larger than those measured at Taylor Dome and AP0602, 2.92 and $3.60*10^{-7}$ m^2/s, respectively [*Courville,* 2007]. (Accumulation rates in the megadunes ranged from 3.0-4.1 cm weq/yr.) In the top meter of firn at the South Pole, thermal diffusivity was calculated at ~$5.7*10^{-7}$ m^2/s which is also larger than Taylor Dome and AP0602 (Recent accumulation rate at South Pole is ~8 cm weq/yr [*Mosley-Thompson et al.,* 1999]). The difference in the thermal diffusivities is attributed to the natural spatial variation in thermal diffusivity dependant on firn structure, a possible underestimation of thermal conductivity at Taylor Dome and AP0602 due to the open pit thermal conductivity measurements or a combination of these factors.

6.4.1 Comparison of field-calculate and satellite-modeled τ_0's

The Summit field data are robust and can be compared to the satellite-modeled τ_0. Table 6.1 presents the satellite-modeled and field-calculated τ_0's. The extinction length measurements are converted to penetration depth using the satellite look angle of 53° for SSM/I data. The field-calculated τ_0's are double the satellite-modeled τ_0's at

Summit. Figure 6.1 shows the satellite-recorded T_B time series at Summit compared to the simulated T_B time series using surface temperatures and the best-fit or field-calculated τ_0 (equation 6.1). The best-fit τ_0 ranges from 0.2 to 0.7 months depending on the temperature time-series used and the average field-calculated τ_0 is 1.5 months for the satellite pixel containing Summit, Greenland. The root mean square error (RMSE) for the best-fit τ_0 is 2.76 K and for the field calculated 2.90 K (The normalized RMSE's are 0.0126 and 0.0132 for the best-fit and field-calculated τ_0's, respectively.) The fit obtained from the field-calculated τ_0 is remarkably good even if it is not the best-fit.

The field-calculated and best-fit τ_0 simulated T_B's both underestimate and lag the satellite measured T_B during the spring warming and overestimate and lag during fall cooling. These errors indicate that the convolution time scale is too long during seasonal changes, holding on to too much past temperature to reproduce the relatively rapid warming and cooling. This result suggests that τ_0 may vary slightly by season. Simulating T_B more accurately requires a shorter τ_0 in the spring, summer and fall, than in the winter. This seasonal variation in τ_0 would produce an opposite trend with accumulation as observed in West Antarctica; accumulation measurements at Summit in 2001 and 2002 show increased accumulation in summer months [*Dibb and Fahnestock,* 2004]. There is no data to determine whether or not thermal diffusivity

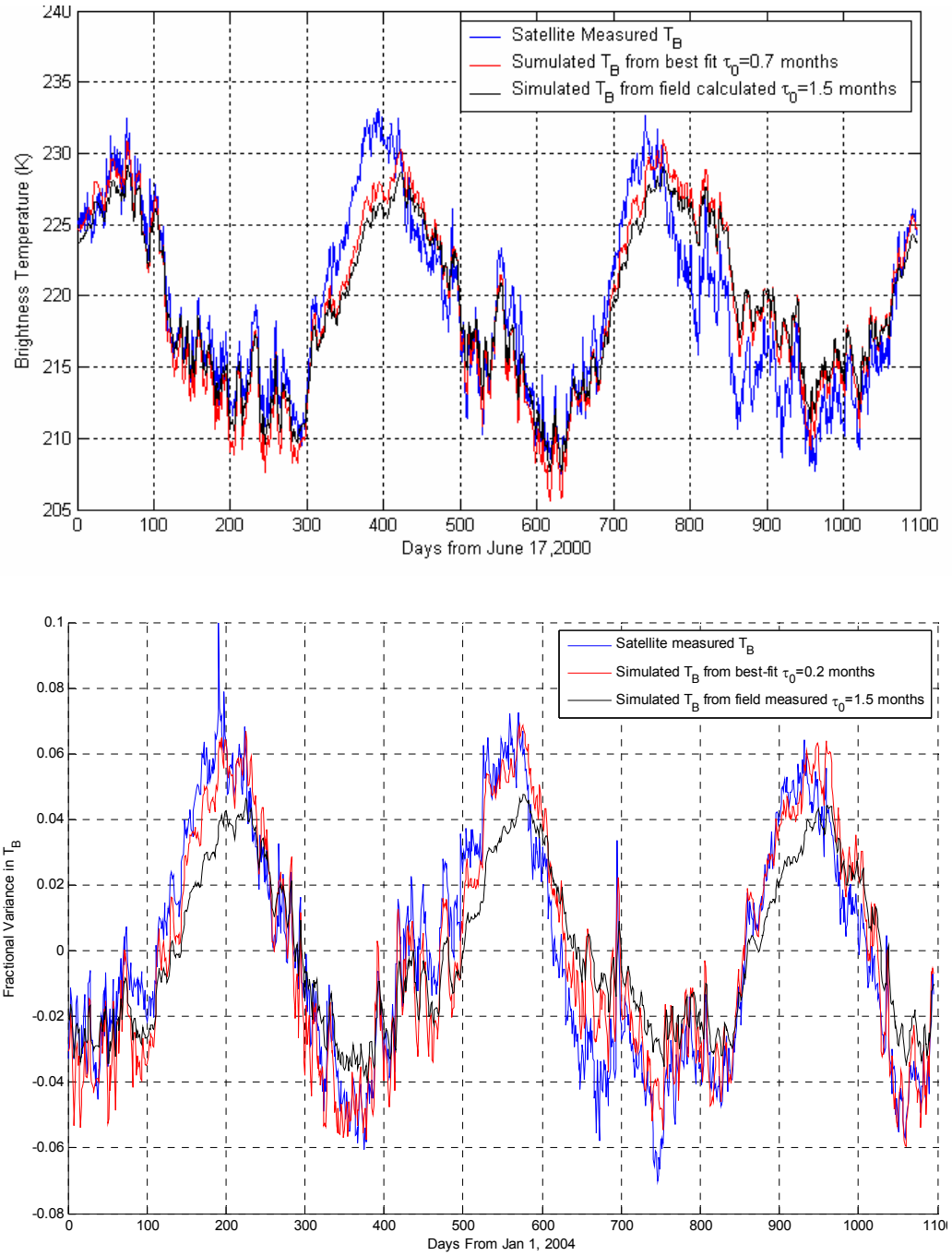

Figure 6.1 Satellite measured T_B compared to the simulated T_B using the best-fit τ_0 and the field-calculated τ_0 at Summit, Greenland. (Top) Time series from 2000 to 2002 best-fit τ_0 =0.7 months (Bottom) Time Series from 2004 to 2006 best-fit τ_0 =0.2 months

and extinction length vary seasonally but this should be investigated. Even though varying τ_0 seasonally may improve the fit with satellite measured T_B, using the best-fit τ_0 or the field-calculated τ_0 are still significantly better at simulating satellite T_B than previous methods (Figure 6.2).

The field-calculated τ_0's are approximately twice that of the satellite-modeled τ_0's. It is still unknown why the field-calculated τ_0 is twice that of the satellite modeled, however, it is possible to eliminate and suggest some causes. The discrepancy is probably not from an underestimation of thermal diffusivity. The thermal diffusivity would have to increase to twice the field-calculated number for the τ_0's to align which is unlikely because two different studies measured very similar thermal conductivities, temperatures and densities at Summit [*Albert and Courville*, Chapter 5]. The discrepancy is probably not from neglecting the multiple scattering term in the radiative transfer equation. The radiometer data points to negligible scattering at 37 GHz (Chapter 3).

A possible explanation for the discrepancy is that the extinction length with an incident angle of 53° is shorter than those measured at 0°, which were used in the calculations. Results in Chapter 3 show a decrease in extinction length of ~10 cm when using radiometer data with an incident angle of 30° compared to an incident angle of 0°. If this trend continues, a shorter extinction length at a 53° incident angle

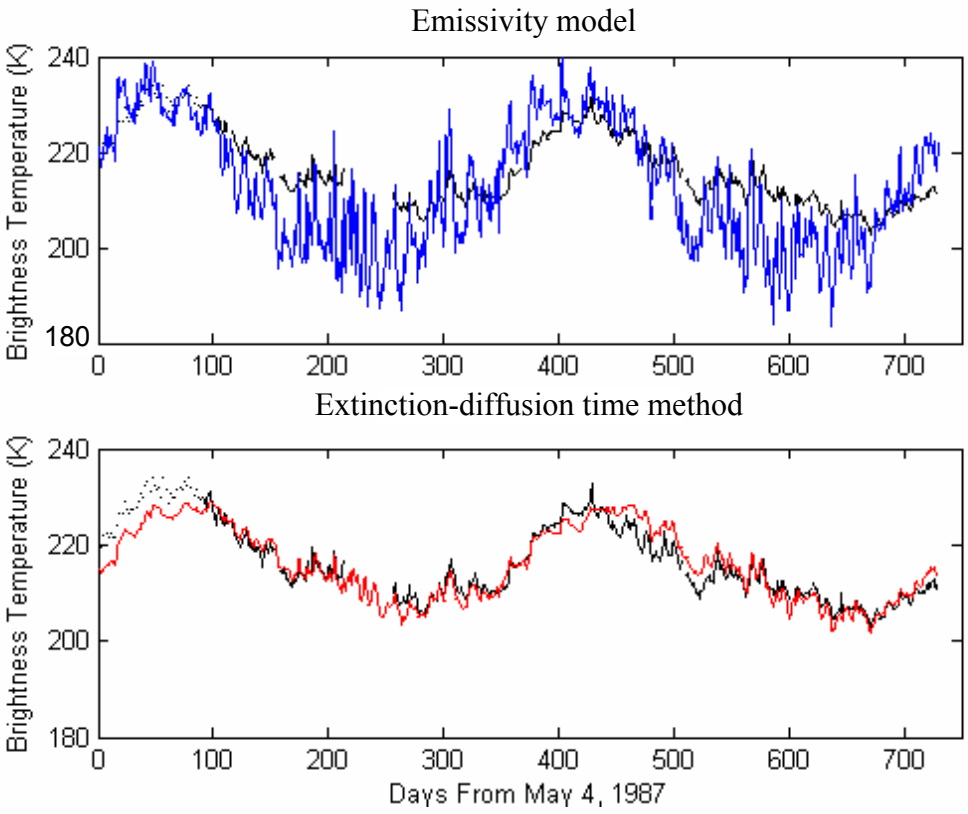

Figure 6.2 Top: Comparison of satellite brightness temperature (black) to the simulated brightness temperature (blue) using the emissivity model [*Shuman et al.*, 1995]. Bottom: Comparison of the satellite brightness temperature (black) to the simulated brightness temperature from the best-fit τ_0 (red) using the extinction-diffusion time model [*Winebrenner et al.*, 2004].

is expected. The shortening of the extinction length at higher incident angles is explained by increased reflection loss at interfaces. Theoretically, this effect is minimized using the vertically polarized channel near the Brewster angle; however, it should be investigated further with field measurements as a possible explanation of the discrepancy. In order to reproduce the modeled τ_0's an extinction length of 1.1 to 1.2 m is needed. This is a large decrease, probably too large for this proposed mechanism, suggesting that there will probably always be a small discrepancy between the best-fit and field-calculated τ_0's.

6.4.2 Effects of extinction length and thermal diffusivity variations on τ_0

The variations in extinction length and thermal diffusivity are investigated to determine if a variation in one constituent dominates τ_0 variations. The averaged extinction length for the Summit region is ~1.5 m with an accumulation rate of 25 cm weq/yr. The Summit region extinction lengths have a range of 27 cm, or 18%, over an area with similar accumulation rates.

The estimated extinction length at Taylor Dome is 0.66 m with an accumulation rate of 7-9 cm weq/yr. Site AP0602 has a slightly shorter estimated extinction length than Taylor Dome at 0.61 m with approximately the same estimated accumulation rate. The accumulation rate at Site AP0602 is determined by stake measurements made approximately 40 km away. The stake measurements are the closest measurements and are listed as the approximate accumulation rate. In general

accumulation rates are slightly decreasing from Taylor Dome in the direction of site AP0602, similar to the extinction lengths.

It is interesting to note that measured extinction length values at Summit when compared to the estimations in East Antarctica follow predictions that locations with higher accumulation rates have longer extinction lengths. More spatially extensive extinction length measurements and better data from East Antarctica are needed to confirm this result.

Thermal diffusivity decreases with increased accumulation as predicted in each dry-snow case except Summit 06-3. Table 6.2 summarized the data used to calculate the thermal diffusivity at each pit. Summit 06-3 has a higher thermal conductivity than the other sites which is attributed to more rounded and probably more bonded grains at this site (Chapter 5). Thermal diffusivity ranges over the Summit pits from 2.22 to 3.00 10^{-7} m^2/s a range of 0.78 10^{-7} m^2/s, or 35%, with an average of 2.53 10^{-7} m^2/s. The average Summit thermal diffusivity gives the lowest thermal diffusivity at the dry-snow site with the highest accumulation rate. Taylor Dome has the highest thermal diffusivity. The range in thermal diffusivity between AP0602 and Taylor Dome is 0.68 10^{-7} m^2/s, or 23% with an average of 3.26 10^{-7} m^2/s. The range in thermal diffusivities between the Summit data and the East Antarctic data is similar and gives an idea of the natural variation in thermal diffusivity over a range of tens of kilometers at sites with similar accumulation rates and firn structure.

Table 6.2 Summary of the temperature, density, thermal conductivity and thermal diffusivity at field locations.

Pit	Temperature (C)	Density (kg/m^3)	Thermal Conductivity (W/mK)	Thermal Diffusivity (10^{-7} m^2/s)
Swiss Camp	-11.5	357	0.179	3.59
Summit 06-1	-27.7	309	0.099	2.45
Summit 06-2	-28.1	323	0.107	2.51
Summit 06-3	-27.1	327	0.130	3.00
Summit 06-4	-27.1	312	0.100	2.45
Summit 06-5	-26.1	331	0.098	2.22
AP0601	-37.5	315	0.146	3.60
AP0602	-28.9	333	0.129	2.92

Comparison of thermal diffusivities from studies by *Courville et al.* [2007] and *Brandt and Warren* [1997] show a continued increase in thermal diffusivity with decreases in accumulation at the megadunes sites but the relationship breaks down using the South Pole data. The South Pole data uses a different method of measuring thermal conductivity than this study and the megadunes study, which may explain the discrepancy. Studies of the differences between the methodologies are needed for further comparison of the thermal conductivity measurements.

At Summit thermal diffusivities have a larger variation range, 35%, than extinction lengths, 13%. Thermal diffusivities appear to have a larger natural variation than extinction length measurements. Taking into account thermal diffusivities calculated from previous studies at the South Pole and the megadunes region in East Antarctica shows that thermal diffusivities can nearly double over a large spatial extent [*Courville et al.*, 2007; *Brandt and Warren,* 1997]. Figure 6.3 and Figure 6.4 investigate how changes in penetration depth, which is related to extinction

length by equation 6.1, and thermal diffusivity affect the calculated τ_0. Figure 6.3 shows the calculated τ_0 given the range of penetration depths measured at Summit, Greenland and a large range of reasonable thermal diffusivity measurements for polar firn. Figure 6.3 shows τ_0 calculations, in general, are most sensitive to changes in penetration depth or extinction length and not thermal diffusivity. τ_0 is equally sensitive to extinction length and thermal diffusivity when extinction lengths are high and thermal diffusivities are low. Figures 6.4 mimics Figure 6.3 but for penetration depth in the range estimated for Taylor Dome, Antarctica. At shorter penetration depths τ_0 has very little dependence on thermal diffusivity illustrated by the penetration depth curves being close to horizontal. Figure 6.3 and 6.4 use the same axis for direct comparison.

Figure 6.3 and 6.4 point to two different regimes for variations in τ_0. In the first regime, when extinction lengths are short and thermal diffusivities are high, τ_0 variations are driven by changes in extinction length. In the second regime, when extinction lengths are long and thermal diffusivities are low, τ_0 variations are equally sensitive to changes in extinction length and thermal diffusivity.

The field-calculated τ_0's are compared to the West Antarctic data where the initial variation with accumulation rate was found. Figure 6.5 presents a scatter plot of accumulation to satellite-model (West Antarctic) and field-calculated (Summit and

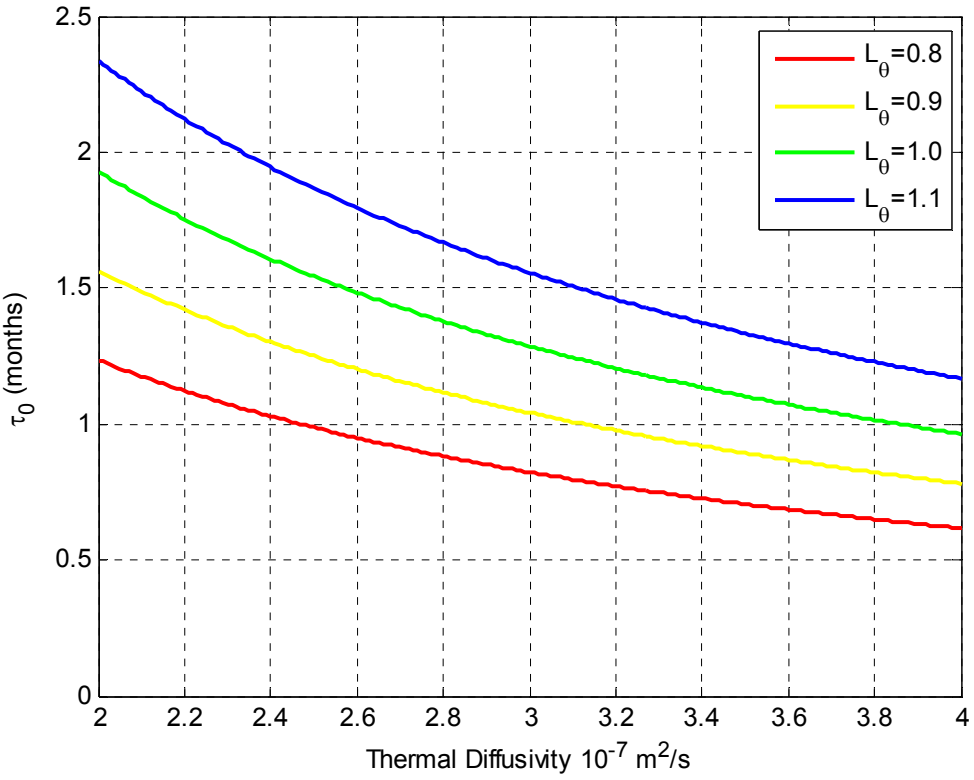

Figure 6.3 Variations in τ_0 given a range of thermal diffusivities and penetration depths, which are directly related to the extinction lengths, similar to Summit, Greenland. In general τ_0 is most sensitive to changes in penetration depth which is related to extinction length. For high long penetration depth and small thermal diffusivities, τ_0 is equally sensitive to changes in penetration depth and thermal diffusivity.

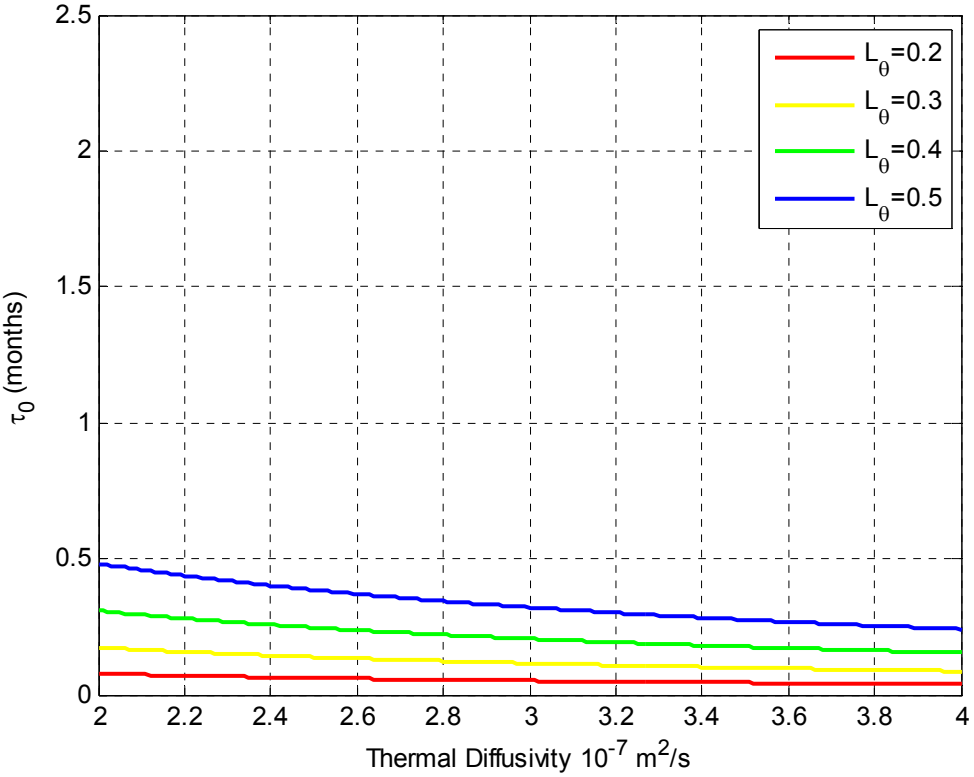

Figure 6.4 Variations in τ_0 given a range of thermal diffusivities and penetration depths similar to East Antarctica. τ_0 is most sensitive to changes in penetration depth with is directly related to extinction length.

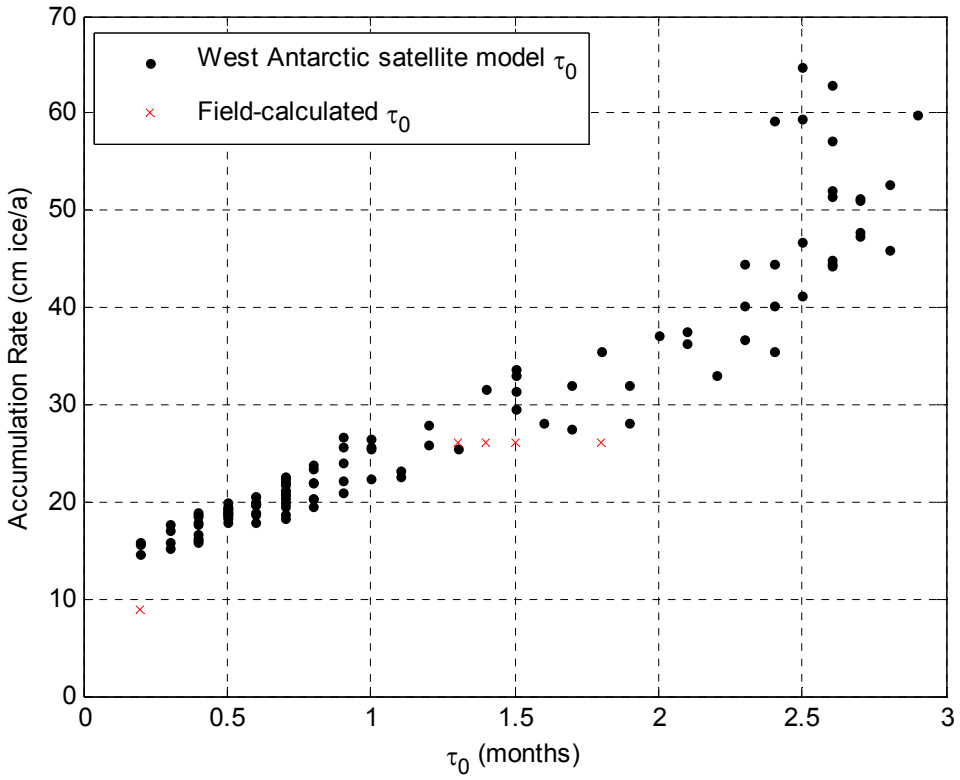

Figure 6.5 Scatter plot of τ_0 and accumulation rate for the field measurements and the modeled τ_0's from West Antarctica.

East Antarctic) τ_0's. In this comparison it is again noted that the East Antarctic extinction length estimations are probably low so τ_0 is expected to increase with a more reliable measurement. The field-calculated τ_0's from Summit are similar to satellite-modeled τ_0's in West Antarctica for similar accumulation rates. The field-calculated τ_0's from East Antarctica appears slightly high for the low accumulation rate. It is difficult to compare the East Antarctic data to the West Antarctic data because the regions are different and the East Antarctic data does have errors as explained above. Given these problems it is surprising that the data lines up so well.

6.5 Conclusions

Initial field investigations of firn thermal diffusivity and microwave extinction length suggest a relationship with accumulation rate in the dry-snow zones of ice sheets. More and better field-measurements of extinction length are needed to confirm this relationship, but initial data look promising. This data does not explain why τ_0, the extinction-diffusion time of microwave emission, varies with accumulation rate in West Antarctica, but it does point to variations of both thermal diffusivity and extinction length with accumulation. The observed correlation between τ_0 and accumulation rate is probably driven by changes in both thermal diffusivity and extinction length, though τ_0 was shown to be more sensitive to changes in extinction length.

Field-calculated τ_0's were double the satellite modeled best-fit τ_0's at Summit, Greenland. Summit data shows that modeling work and field measurements both are able to simulate satellite brightness temperature well and better than previous methods. The field-measured τ_0's at Summit compare well with satellite-measured τ_0's in West Antarctica at similar accumulation rates.

The extinction length, thermal diffusivity and extinction-diffusion time, $\tau_{0,}$ all appear to have a relationship with accumulation rate. The link between extinction length, thermal diffusivity and accumulation rate warrants further investigation, hopefully leading to a new method of monitoring accumulation rate from space-borne satellites.

Chapter 7

CONCLUSIONS AND FUTURE WORK

The focus of this dissertation is the application of an improved model of microwave emission from polar firn and a comparison to field measurements of polar firn properties. The results largely validate the model and represent one of the most comprehensive data sets available of firn thermal diffusivity and microwave extinction length. This chapter summarizes these results and poses questions for future work.

7.1 Field measurements

The data presented in Chapters 3-5 are new field measurements of firn properties relevant to passive microwave remote sensing. Many previous studies used passive microwave data to estimate accumulation rates on ice sheets [*Vaughan et al*., 1999; *Winebrenner et al.*, 2001; *Zwally and Giovinetto*, 1995; *Zwally*, 1977]. These studies met with limited success because the passive microwave signal is related to firn properties and temperature within the depth-range corresponding to the microwave extinction length. Firn property data along with corresponding extinction length data are rare. Such data are necessary to assess the influence of firn properties on passive microwave measurements, and to make progress in the use of microwave sensors to monitor firn properties – including accumulation rate – through time.

Chapter 3 presented methods for obtaining direct measurements of extinction length in polar firn, using a radiometer and a high frequency radar. These methods improve upon previous attempts to measure extinction length because the firn column is left intact and measurements can be repeated at a variety of locations. A radar extinction length estimate taken at Summit, Greenland is shorter than radiometer measurements taken a year earlier. The error is largely explained by errors in the radar data but may also suggest temporal changes in the extinction length. Both methods appear to be valid means of measuring extinction length, though the radiometer measurements are currently the preferred method for accuracy. Extinction lengths were gathered in tandem with detailed firn microstructure data. The firn microstructure data was used to model the extinction lengths using strong fluctuation theory. Modeled extinction lengths are significantly shorter than measured extinction lengths using field grain size measurements. Measured extinction lengths were shown to be less sensitive to grain size changes than expected from theory; radiative transfer equations only reproduced measurements with a negligible scattering coefficient. The discrepancy between the extinction length measurements and the model persisted with different grain-size measurements including the volume-to-surface ratio. The discrepancy emphasizes: 1) the need for more quantitative and easy methods to measure grain size and 2) extinction length measurements in tandem with modeling data to validate models.

Chapter 4 presents a method to estimate extinction length from radar profiles. This method is necessary to expand the amount of extinction length data; radar profiles in the microwave region are more common than direct extinction length measurements.

Chapter 5 presents data on the thermal properties of firn relevant to passive microwave remote sensing. A new data set of thermal conductivity was collected. Thermal conductivity was shown to have no correlation with depth in the top 2 meters of firn. Firn thermal conductivities are lower than conductivity measurements in seasonal snow. Firn thermal diffusivities were calculated from the conductivity measurements at field sites to compare with the extinction-diffusion time.

7.2 The extinction- diffusion time of microwave emission

Chapter 2 presents the extinction-diffusion time model of microwave emission developed by *Winebrenner et al.* [2004], and examines its application to the assessment of spatial and temporal accumulation rate variations. This model is able to simulate passive microwave brightness temperature from a surface-temperature time series better than any previous model. The physics of this model pointed to two relevant firn properties for passive microwave remote sensing, the microwave extinction length and the firn thermal diffusivity. The time scale of this model, the extinction-diffusion time was shown to vary in space and time and with accumulation rate in West Antarctica.

Initial model results from the extinction-diffusion time predicted that the extinction length increased with accumulation rate, while thermal diffusivity decreased with accumulation rate. Field measurements presented in Chapter 6 do not contradict the initial model results; at three dry-snow ice sheet locations thermal diffusivity decreases with increased accumulation rate. The lack of direct measurements of extinction length at the East Antarctic sites limited conclusions about the variation of extinction length with accumulation rate but the estimated extinction lengths did follow the expected trend with accumulation rate. Field-measured extinction-diffusion times are ~2 times higher than model results but also follow the same trend. Both the field-measured and modeled extinction-diffusion times simulate brightness temperatures well. Modeled and field results show that the extinction-diffusion time of microwave emission still may be a viable means to monitor accumulation rate in specific ice sheets regions because it varies with firn parameters sensitive to accumulation rate.

7.3 Future work

The ultimate goal of this research is to use passive microwave remote sensing to accurately monitor temperature and accumulation rates on polar ice sheets, starting with the initial measurements taken in 1978. The extinction-diffusion time model highlighted two very important firn parameters relevant to passive microwave remote sensing, the microwave extinction length and the thermal diffusivity. Remarkably, the

microwave extinction length had rarely been carefully measured on ice sheets. Models exist but were validated by only a few points. The question of how deep passive microwave sensors record firn information is still uncertain over large portions of the ice sheet but this work is starting to reduce the uncertainty in extinction lengths by measuring it directly at Swiss Camp and Summit, Greenland and estimating it at two locations in East Antarctica. Future work needs to focus on taking extinction length measurements along with firn microstructure information at a greater number of ice sheet locations. Specifically, measurement of extinction length and thermal diffusivity should be taken in a traverse across a major accumulation divide like the West Antarctic divide. Initially, future work should focus on the 37 GHz frequency because extinction lengths are on the same order as readily-obtained pit depths, making the collection of firn microstructure relatively straightforward. The next frequency to be explored should be 19 GHz, where there are more existing Frequency-Modulated Continuous Wave (FMCW) radars to collect data.

Extinction-diffusion time maps of Antarctica show a significant correlation with accumulation rate in West Antarctica, suggesting that further research of this relationship in West Antarctica may prove fruitful. Additionally, a site where the extinction-diffusion time does not vary with accumulation rate should be investigated to get a better understanding of other controls on the microwave signal. There are divides in East Antarctica where the extinction-diffusion time varies for reasons that remain unclear. However, addressing this will be difficult because existing data is

very sparse and unreliable in these areas. This investigation should be conducted along with airborne radar survey to obtain direct accumulation rate estimates.

This research showed that very-high-frequency radars provide useful information on ice sheets. Their utility should be used to help validate space-borne instruments, monitor firn structure in the top 1-10 m of firn and to turn layer information into recent accumulation rate measurements.

The new research directions suggested will generally involve large-scale projects to gather new information. There is, however, considerably more that could be done with the field dataset presented in this dissertation. In particular, the discrepancies between field-measured extinction lengths and modeled extinction lengths warrant further examination. Field-grain-size measurements have a much larger range than is reasonable for the modeled range of extinction lengths. Field-grain-size measurements often overestimate and the volume-to-surface area ratio has been shown previously to be a better grain-size measurement for electromagnetic models, but neither worked well in this study. New methods to quantify grain size, such three-dimensional scanning, may be helpful in determining the appropriate grain size for modeling, but the models should also be reevaluated as more measured extinction length data becomes available.

Finally, it is suggested that extinction-diffusion time maps should be created for Greenland and updated for Antarctica as new satellite and ground-based accumulation rate data become available. Monitoring extinction-diffusion time maps

over the ice sheet may lead to a viable method for monitoring accumulation rate over large ice sheet areas.

LIST OF REFERENCES

Arthern, R. J., Winebrenner, D. P., and Vaughan, D. G. (2006). Antarctic snow accumulation mapped using polarization of 4.3-cm wavelength microwave emission. *Journal of Geophysical Research-Atmospheres*, 111(D6).

Beaven, S. (1995). Sea Ice Radar Backscatter Modeling, Measruemetns and the Fusion of Active and Passive Microwave Data. Dissertation, University of Kansas, Department of Electrical Engineering and Computer Science.

Bindschadler, R. (1998). Monitoring ice sheet behavior from space. *Reviews of Geophysics*, 36(1), 79-104.

Brandt, R. E., and Warren, S. G. (1993). Solar-Heating Rates and Temperature Profiles in Antarctic Snow and Ice. *Journal of Glaciology*, 39(131), 99-110.

Brandt, R. E., and Warren, S. G. (1997). Temperature measurements and heat transfer in near-surface snow at the South Pole. *Journal of Glaciology*, 43(144), 339-351.

Bromwich, D. H., and A. N. Rogers. (2001). The El Nino– Southern Oscillation modulation of West Antarctic precipitation. *The West Antarctic Ice Sheet: Behavior and Environment, Antarct. Res. Ser.* Editors R. B. Alley and R. A. Bindschadler, 77(AGU, Washington, D. C.), pp. 91– 103.

Chapman, W. L., and Walsh, J. E. (2007). A synthesis of Antarctic temperatures. *Journal of Climate*, 20(16), 4096-4117.

Colbeck, S., Akitaya, E., Armstrong, R., Gubler, H., Lafeuille, J., Lied, K., McClung, D., and Morris, E. (1990). The International Classification for Seasonal Snow on the Ground. Boulder ,CO. International Commission on Snow and Ice and World Data Center A for Glaciology.

Comiso, J. C. (2000). Variability and trends in Antarctic surface temperatures from in situ and satellite infrared measurements. *Journal of Climate*, 13(10), 1674-1696.

Comiso, J. C. (2003). Warming Trends in the Arctic from Clear Sky Satellite Observations. *Journal of Climate*, 16, 3498-3510.

Conway, H., and Wilbour, C. (1999). Evolution of snow slope stability during storms. *Cold Regions Science and Technology*, 30(1-3), 67-77.

Courville, Z. R. (2007). Gas Diffusivity and Air Permeability of the Firn from Cold Polar Sites. Dissertation, Dartmouth College, Thayer School of Engineering.

Courville, Z. R., Albert, M. R., Fahnestock, M. A., Cathles, L. M., and Shuman, C. A. (2007). Impacts of an accumulation hiatus on the physical properties of firn at a low-accumulation polar site. *Journal of Geophysical Research-Earth Surface*, 112(F2).

Davis, C. H., and Poznyak, V. I. (1993). The Depth of Penetration in Antarctic Firn at 10 Ghz. *Ieee Transactions on Geoscience and Remote Sensing*, 31(5), 1107-1111.

Davis, R. E., Dozier, J., and Chang, A. T. C. (1987). Snow Property Measurements Correlative to Microwave Emission at 35 Ghz. *Ieee Transactions on Geoscience and Remote Sensing*, 25(6), 751-757.

Dibb, J. E., and Fahnestock, M. (2004). Snow accumulation, surface height change, and firn densification at Summit, Greenland: Insights from 2 years of in situ observation. *Journal of Geophysical Research-Atmospheres*, 109(D24).

Doran, P. T., Priscu, J. C., Lyons, W. B., Walsh, J. E., Fountain, A. G., McKnight, D. M., Moorhead, D. L., Virginia, R. A., Wall, D. H., Clow, G. D., Fritsen, C. H., McKay, C. P., and Parsons, A. N. (2002). Antarctic climate cooling and terrestrial ecosystem response. *Nature*, 415(6871), 517-520.

Gloerson, P., D. Cavalieri, W.J. Campbell, and J. Zwally. (1990). Nimbus-7 SMMR polar radiances and Arctic and Antarctic sea ice concentrations. National Snow and Ice Data Center, Boulder, CO.

Gow, A. J. (1969). On the Rates of Growth of Grains and Crystals in South Polar Firn. *Journal of Glaciology*, 8(3), 241-252.

Grenfell, T. C., and Lohanick, A. W. (1985). Temporal Variations of the Microwave Signatures of Sea Ice During the Late Spring and Early Summer near Mould Bay Nwt. *Journal of Geophysical Research-Oceans*, 90(NC3), 5063-5074.

Grenfell, T. C., and Warren, S. G. (1999). Representation of a nonspherical ice particle by a collection of independent spheres for scattering and absorption of radiation. *Journal of Geophysical Research-Atmospheres*, 104(D24), 31697-31709.

Hall, D. (1987). Influence of depth hoar on microwave emission from snow in Northern Alaska. *Cold Regions Science and Technology*, 13, 225-231.

Hall, D. K., and Martinec, J. (1985). Remote sensing of ice and snow, Chapman and Hall, London; New York.

Hallikainen, M. T., Ulaby, F. T., and Vandeventer, T. E. (1987). Extinction Behavior of Dry Snow in the 18-Ghz to 90-Ghz Range. *Ieee Transactions on Geoscience and Remote Sensing*, 25(6), 737-745.

Hollinger, J. P., Peirce, J. L., and Poe, G. A. (1990). SSM/I Instrument Evaluation. *IEEE Tansactions on Geoscience and Remote Sensing*, 28(5), 781-790.

Hörhold, M. W. (2006). Microstructure and Air Transport Properties of Polar Firn. Dissertation, University of Bremen, Alfred Wegener Institute for Polar and Marine Research.

IPCC. (2007). Intergovernmental Panel on Climate Change Forth Assessment Report Climate Change 2007:Synthesis Report.

Jackson, R., and Taylor, S. (1986). Thermal Conductivity and Diffusivity, Chapter 39 in *Methods of Soil Analysis, Part 1. Physical and Mineralogical Methods.*

Kaspari, S., Mayewski, P. A., Dixon, D. A., Spikes, V. B., Sneed, S. B., Handley, M. J., and Hamilton, G. S. (2004). Climate variability in West Antarctica derived from annual accumulation-rate records from ITASE firn/ice cores. *Annals of Glaciology*, 39, 2005, 585-594.

King, J. C. (1994). Recent Climate Variability in the Vicinity of the Antarctic Peninsula. *International Journal of Climatology*, 14(4), 357-369.

Koenig, L. S., Steig, E. J., Winebrenner, D. P., and Shuman, C. A. (2007). A link between microwave extinction length, firn thermal diffusivity, and accumulation rate in West Antarctica. *Journal of Geophysical Research-Earth Surface*, 112(F3).

Lange, M. A. (1985). Measurements of Thermal Parameters in Antarctic Snow and Firn. *Annals of Glaciology*, 6, 100-104.

Legarsky, J. (1999). Synthetic-aperture Radar (SAR) Processing of Glacial-Ice Depth-Sounding Data, Ka-Band Backscattering Measurements and Applications. . Dissertation, University of Kansas, Department of Electrical Engineering and Computer Science.

MacGregor, J. A., Winebrenner, D. P., Conway, H., Matsuoka, K., Mayewski, P. A., and Clow, G. D. (2007). Modeling englacial radar attenuation at Siple Dome, West Antarctica, using ice chemistry and temperature data. *Journal of Geophysical Research-Earth Surface*, 112(F3).

Marshall, H. P., Koh, G., and Forster, R. R. (2004). Ground-based frequency-modulated continuous wave radar measurements in wet and dry snowpacks, Colorado, USA: an analysis and summary of the 2002-03 NASA CLPX data. *Hydrological Processes*, 18(18), 3609-3622.

Marshall, H. P., Schneebeli, M., and Koh, G. (2007). Snow stratigraphy measurements with high-frequency FMCW radar: Comparison with snow micro-penetrometer. *Cold Regions Science and Technology*, 47(1-2), 108-117.

Maslanik, J., and J. Stroeve. (1990). DMSP SSM/I daily polar gridded brightness temperatures. National Snow and Ice Data Center.

Matsuoka, T., Fujita, S., and Mae, S. J. (1996). Effect of temperature on dielectric properties of ice in the range 5-39 GHz. *Journal of Applied Physics*, 80(10), 5884-5890.

Mätzler, C. (1987). Applications of the interaction of microwaves with the natural snow cover. *Remote Sensing Reviews*, 2, 259-387.

Mätzler, C. (2002). Relation between grain-size and correlation length of snow. *Journal of Glaciology*, 48(162), 461-466.

Mätzler, C., and Wegmüller, U. (1987). Dielectric-Properties of Fresh-Water Ice at Microwave-Frequencies. *Journal of Physics D-Applied Physics*, 20(12), 1623-1630.

Mayewski, P. A., Meeker, L. D., Twickler, M. S., Whitlow, S., Yang, Q. Z., Lyons, W. B., and Prentice, M. (1997). Major features and forcing of high-latitude northern hemisphere atmospheric circulation using a 110,000-year-long glaciochemical series. *Journal of Geophysical Research-Oceans*, 102(C12), 26345-26366.

Monaghan, A. J., Bromwich, D. H., Chapman, W., and Comiso, J. C. (2008). Recent variability and trends of Antarctic near-surface temperature. *Journal of Geophysical Research-Atmospheres*, 113(D4).

Monaghan, A. J., Bromwich, D. H., Fogt, R. L., Wang, S. H., Mayewski, P. A., Dixon, D. A., Ekaykin, A., Frezzotti, M., Goodwin, I., Isaksson, E., Kaspari, S. D., Morgan, V. I., Oerter, H., Van Ommen, T. D., Van der Veen, C. J., and Wen, J. H. (2006). Insignificant change in Antarctic snowfall since the International Geophysical Year. *Science*, 313(5788), 827-831.

Monaghan, A. J., Bromwich, D. H., Powers, J. G., and Manning, K. W. (2005). The climate of the McMurdo, Antarctica, region as represented by one year of forecasts from the Antarctic Mesoscale Prediction System. *Journal of Climate*, 18(8), 1174-1189.

Morse, D. L., Blankenship, D. D., Waddington, E. D., and Neumann, T. A. (2002). A site for deep ice coring in West Antarctica: results from aerogeophysical surveys and thermo-kinematic modeling. *Annals of Glaciology*, 35, 36-44.

Morse, D. L., Waddington, E. D., Marshall, H. P., Neumann, T. A., Steig, E. J., Dibb, J. E., Winebrenner, D. P., and Arthern, R. J. (1999). Accumulation rate measurements at Taylor Dome, East Antarctica: Techniques and strategies for mass balance measurements in polar environments. *Geografiska Annaler Series a-Physical Geography*, 81A(4), 683-694.

Mosley-Thompson, E., Paskievitch, J. F., Gow, A. J., and Thompson, L. G. (1999). Late 20th Century increase in South Pole snow accumulation. *Journal of Geophysical Research-Atmospheres*, 104(D4), 3877-3886.

Paterson, W. S. B. (1994). *The Physics of Glaciers*, Butterworth-Heinemann, Oxford.

Perla, R. (1978). Failure of snow slopes in Rockslides and Avalanches,1, editor B. Voight, pp. 731-751.

Perla, R. (1982). Preparation of section planes in snow specimens. *Journal of Glaciology*, 28(98), 199-204.

Rott, H. (1989). Multispectral microwave signatures of the Antarctic ice sheet, Microwave radiometry and remote sensing application. *In: P. Pampaloni (Ed.), Proceedings of the specialist meeting, Florence, Italy.*

Rott, H., Sturm, K., and Miller, H. (1993). Active and passive microwave signatures of Antarctic firn by means of Antarctic firn by means of field measurements and satellite date. *Annals of Glaciology*, 17, 337–343.

Schneider, D. P. (2005). Antarctic climate of the past 200 years from an integration of instrumental, satellite, and ice core proxy data, University of Washington, Seattle.

Schneider, D. P., and Steig, E. J. (2002). Spatial and temporal variability of Antarctic ice sheet microwave brightness temperatures. *Geophysical Research Letters*, 29(20).

Schneider, D. P., Steig, E. J., and Comiso, J. C. (2004). Recent climate variability in Antarctica from satellite-derived temperature data. *Journal of Climate*, 17(7), 1569-1583.

Scott, J. B. T., Mair, D., Nienow, P., Parry, V., and Morris, E. (2006). A ground-based radar backscatter investigation in the percolation zone of the Greenland ice sheet. *Remote Sensing of Environment*, 104(4), 361-373.

Shi, J., Davis, R. E., and Dozier, J. (1993). Stereological determination of dry-snow parameters for discrete-scatterer microwave modeling. *Annals of Glaciology*, 17, 295-299.

Shuman, C. A., and Alley, R. B. (1993). Spatial and Temporal Characterization of Hoar Formation in Central Greenland Using Ssm/I Brightness Temperatures. *Geophysical Research Letters*, 20(23), 2643-2646.

Shuman, C. A., Alley, R. B., Anandakrishnan, S., and Stearns, C. R. (1995). An Empirical Technique for Estimating near-Surface Air-Temperature Trends in Central Greenland from Ssm/I Brightness Temperatures. *Remote Sensing of Environment*, 51(2), 245-252.

Shuman, C. A., and Comiso, J. C. (2002). In situ and satellite surface temperature records in Antarctica. *Annals of Glaciology*, 34, 2002, 113-120.

Shuman, C. A., and Stearns, C. R. (2001). Decadal-length composite inland West Antarctic temperature records. *Journal of Climate*, 14(9), 1977-1988.

Shuman, C. A., Zwally, H. J., Schutz, B. E., Brenner, A. C., DiMarzio, J. P., Suchdeo, V. P., and Fricker, H. A. (2006). ICESat Antarctic elevation data: Preliminary precision and accuracy assessment. *Geophysical Research Letters*, 33(7).

Spikes, V. B., Hamilton, G. S., Arcone, S. A., Kaspari, S., and Mayewski, P. A. (2005). Variability in Accumulation Rates from GPR Profiling on the West Antarctic Plateau *Annal of Glaciology*, 39(Preprint).

Stogryn, A. (1974). Electromagnetic Scattering by Random Dielectric-Constant Fluctuations in a Bounded Medium. *Radio Science*, 9(5), 509-518.

Stogryn, A. (1986). A Study of the Microwave Brightness Temperature of Snow from the Point-of-View of Strong Fluctuation Theory. *Ieee Transactions on Geoscience and Remote Sensing*, 24(2), 220-231.

Stove, A. G. (1992). Linear Fmcw Radar Techniques. *Iee Proceedings-F Radar and Signal Processing*, 139(5), 343-350.

Sturm, M., Holmgren, J., Konig, M., and Morris, K. (1997). The thermal conductivity of seasonal snow. *Journal of Glaciology*, 43(143), 26-41.

Sturm, M., and Johnson, J. B. (1992). Thermal-Conductivity Measurements of Depth Hoar. *Journal of Geophysical Research-Solid Earth*, 97(B2), 2129-2139.

Sturm, M., Perovich, D. K., and Holmgren, J. (2002). Thermal conductivity and heat transfer through the snow on the ice of the Beaufort Sea. *Journal of Geophysical Research-Oceans*, 107(C21).

Surdyk, S. (2002). Using microwave brightness temperature to detect short-term surface air temperature changes in Antarctica: An analytical approach. *Remote Sensing of Environment*, 80, 356-271.

Surdyk, S., and Fily, M. (1995). Results of a Stratified Snow Emissivity Model-Based on the Wave Approach - Application to the Antarctic Ice-Sheet. *Journal of Geophysical Research-Oceans*, 100(C5), 8837-8848.

Surdyk, S., and Fujita, S. (1995). Microwave Dielectric-Properties of Snow - Modeling and Measurements. *Geophysical Research Letters*, 22(8), 965-968.

Ulaby, F. T., Moore, R. K., and Fung, A. K. (1982). *Microwave Remote Sensing: Active and Passive, Vol II: Radar Remote Sensing and Surface Scattering and Emission Theory*, Addison-Wesley Publishing Company, Inc.

van den Broeke, M. R., and van Lipzig, N. P. M. (2004). Changes in Antarctic temperature, wind and precipitation in response to the Antarctic Oscillation. *Annals of Glaciology*, 39, 2005, 119-126.

Vaughan, D. G., Bamber, J. L., Giovinetto, M., Russell, J., and Cooper, A. P. R. (1999). Reassessment of net surface mass balance in Antarctica. *Journal of Climate*, 12(4), 933-946.

Vaughan, D. G., Marshall, G. J., Connolley, W. M., Parkinson, C., Mulvaney, R., Hodgson, D. A., King, J. C., Pudsey, C. J., and Turner, J. (2003). Recent rapid regional climate warming on the Antarctic Peninsula. *Climatic Change*, 60(3), 243-274.

Weller, G. E., and Schwerdtfeger, P. (1971). New data on the thermal conuctivity of natural snow. *Journal of Glaciology*, 10(59), 309-311.

Winebrenner, D. P., Arthern, R. J., and Shuman, C. A. (2001). Mapping Greenland accumulation rates using observations of thermal emission at 4.5-cm wavelength. *Journal of Geophysical Research-Atmospheres*, 106(D24), 33919-33934.

Winebrenner, D. P., Smith, B. E., Catania, G. A., Conway, H. B., and Raymond, C. F. (2003). Radio-frequency attenuation beneath Siple Dome, West Antarctica, from wide-angle and profiling radar observations. *Annals of Glaciology*, 37, 226-232.

Winebrenner, D. P., Steig, E. J., and Schneider, D. P. (2004). Temporal co-variation of surface and microwave brightness temperatures in Antarctica, with implications for the observation of surface temperature variability using satellite data. *Annals of Glaciology,* 39, 2005, 346-350.

University of Wisconsin,. (2006). Automatic Weather Station Project.

Zwally, H. J., and Giovinetto, M. B. (1995). Accumulation in Antarctica and Greenland derived from passive-microwave data: a comparison with contoured compilations. *Annals of Glaciology*, 21, 123-130.

Zwally, J. H. (1977). Microwave emissivity and accumulation rate of polar firn. *Journal of Glaciology*, 18(79), 195-215.

Appendix A

LOCATION OF FIRN PITS

This appendix summarizes the locations and dates of firn pits and the data collected at each site.

Lat	Long	Pit Name	Location	Date	Data Collected
69.573	-49.295	GLP1	Swiss Camp	5/10/2006	S, TC
69.573	-49.295	GLP2	Swiss Camp	5/12/2006	S, TC
69.573	-49.295	GPL3	Swiss Camp	5/14/2006	S, TC
69.585	-48.254	GLP4	Swiss Camp 7.6 km East	5/17/2006	S, TC
69.748	-48.130	Swiss Pit	Swiss camp, 50 km East	5/19/2006	S, TC, PR
72.579	-38.504	Summit 06-1	Summit, near weather station	5/26/2006	S, TC, PR, DC
72.612	-38.660	Summit 06-2	Summit, 7.6 km West	5/28/2006	S, TC, PR, DC
72.508	-38.568	Summit 06-3	Summit, end of ATM line	6/2/2006	S, TC, PR
72.690	-38.690	Summit 06-4	Summit, 14 km North	5/30/2006	S, TC, PR
72.753	-38.073	Summit 06-5	Summit, 24 km North	6/1/2006	S, TC, PR, DC
72.579	-38.504	Summit 07-1	Summit Camp, Swiss port	6/15/2007	S, AR
72.579	-38.504	Summit 07-2	Summit Camp, off skiway	6/12/2007	S, AR, TR
72.594	-38.625	Albert	Core Site of Mary Albert's Core	6/18/2007	TR
72.636	-38.458	Steig	Core Site of JEMS2 Core	6/18/2007	TR
72.579	-38.504	Skiway	Summit, on skiway	6/18/2007	TR
-77.783	158.716	AP0601	Taylor Dome	11/22/2006	S, TC, TR, DC
-76.767	153.367	AP0602	Itase Traverse Route	12/16/2006	S, TC, TR, DC
-79.035	149.687	AP0603	Itase Traverse Route	12/26/2006	S, TC, DC
-80.308	144.691	AP0604	Itase Traverse Route	1/8/2007	S, TC, DC

Data Collected Key:
S- Pit stratigraphy including layers, grain type, grain size, density and hand hardness,
TC- Thermal conductivity and temperature profile
PR- 37 GHz Radiometer measurements
AR- 32-40 GHz FMCW radar measurements with reflector
TR- 32-40 GHz FMCW radar profile/transect data
DC- Dimethyl phthalate cast of the firn
Lat- Positive numbers are North latitudes and negative numbers are South latitudes
Long- Positive numbers are East Longitudes and negative numbers are West longitudes

.

Appendix B

INDIVIDUAL PIT DATA FROM GREENLAND

This appendix presents the field data collected at each radiometer pit conducted in Greenland and the pit stratigraphy for Summit pit 07-1 and Summit pit 07-2. The snow pit stratigraphy includes layer thickness, hand hardness, grain type, temperature and density. Each firn layers is represented by a rectangular box where the height of the box is the layer thickness and corresponds to the y-axis of the graph. The length of the box shows the hand hardness and corresponds to the bottom x-axis of the graph. The temperature profile is shown by the solid line and corresponds to the top axis of the graph. The density profile is shown by the dashed line and corresponds to the bottom axis of the graph. The grain type is defined using the international classification of seasonal snow and is given for each layer [Colbeck, et al., 1990]. The second figure compares the thermal conductivity, grain size, density, measured extinction length, the imaginary part of the complex dielectric constant and the modeled extinction length by pit depth. The exact location and date for each pit is given in Appendix A.

B.1 Swiss Camp Pit

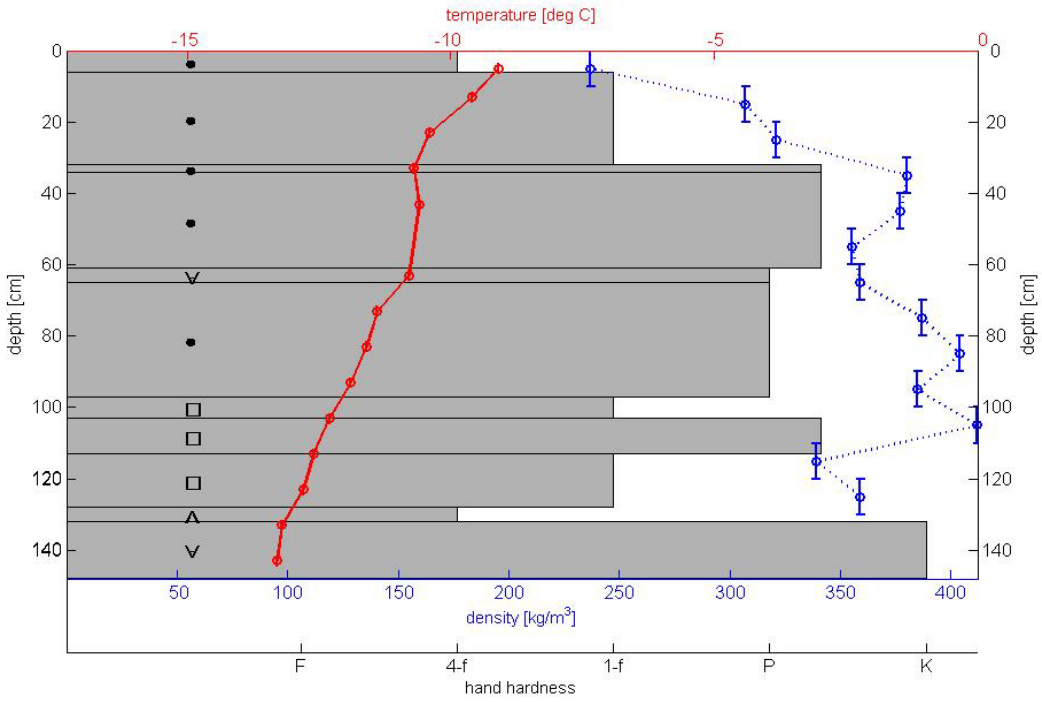

Figure B. 1 Snow pit stratigraphy for Swiss Camp Pit.

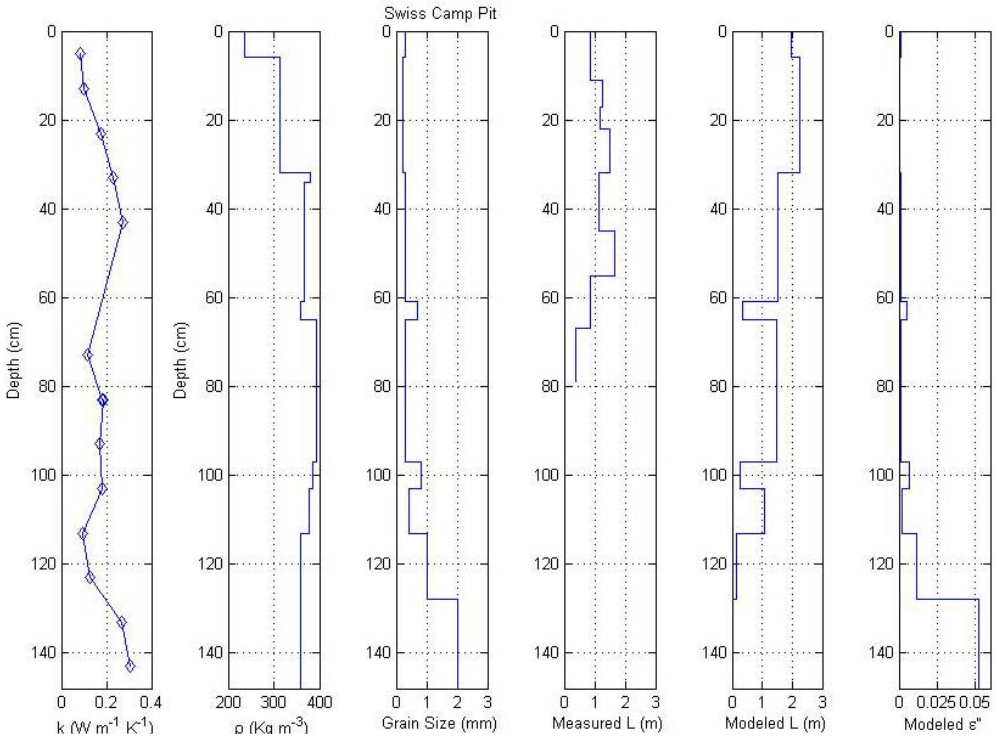

Figure B. 2 Thermal conductivity, density, grain size, measured extinction length, modeled extinction length and the imaginary part of the SFT modeled dielectric constant for Swiss Camp Pit.

B.3 Summit Pit 06-1

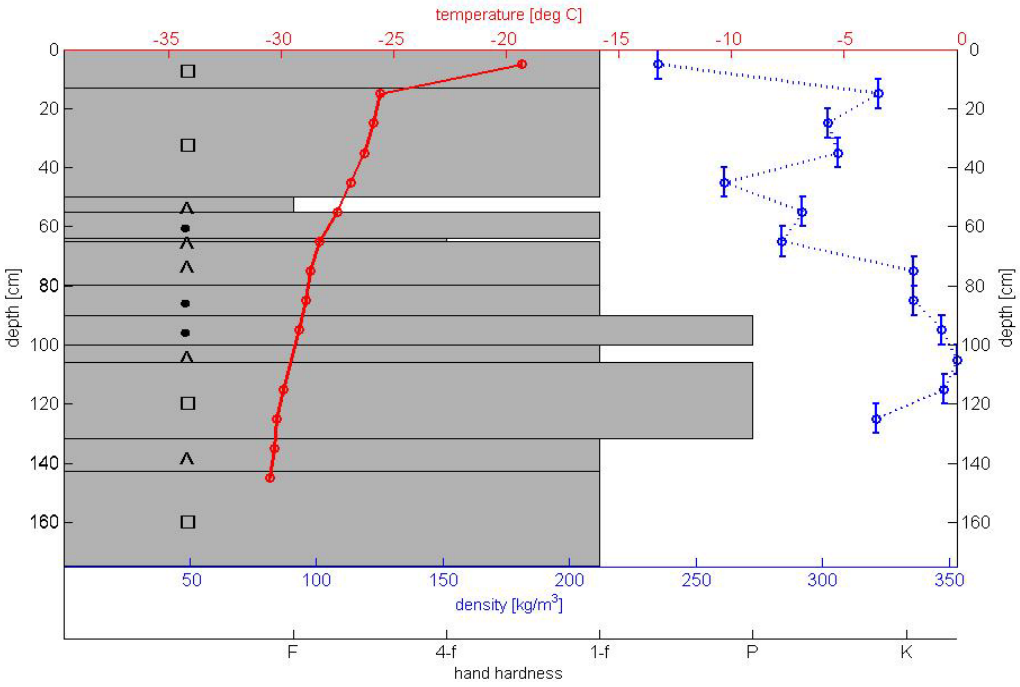

Figure B. 3 Snow pit stratigraphy for Summit 06-1.

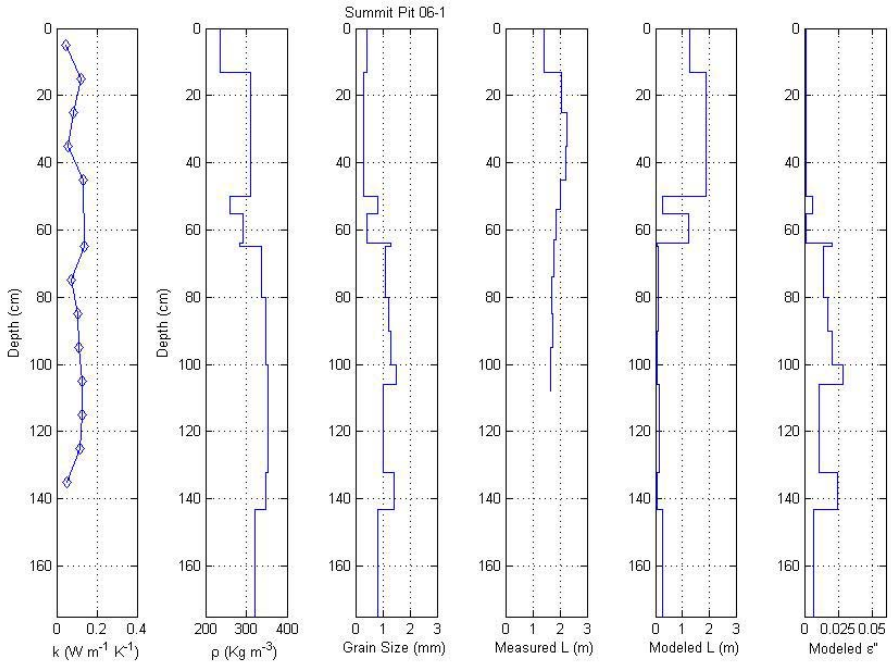

Figure B. 4 Thermal conductivity, density, grain size, measured extinction length, modeled extinction length and the imaginary part of the SFT modeled dielectric constant for Summit 06-1.

B.3 Summit Pit 06-2

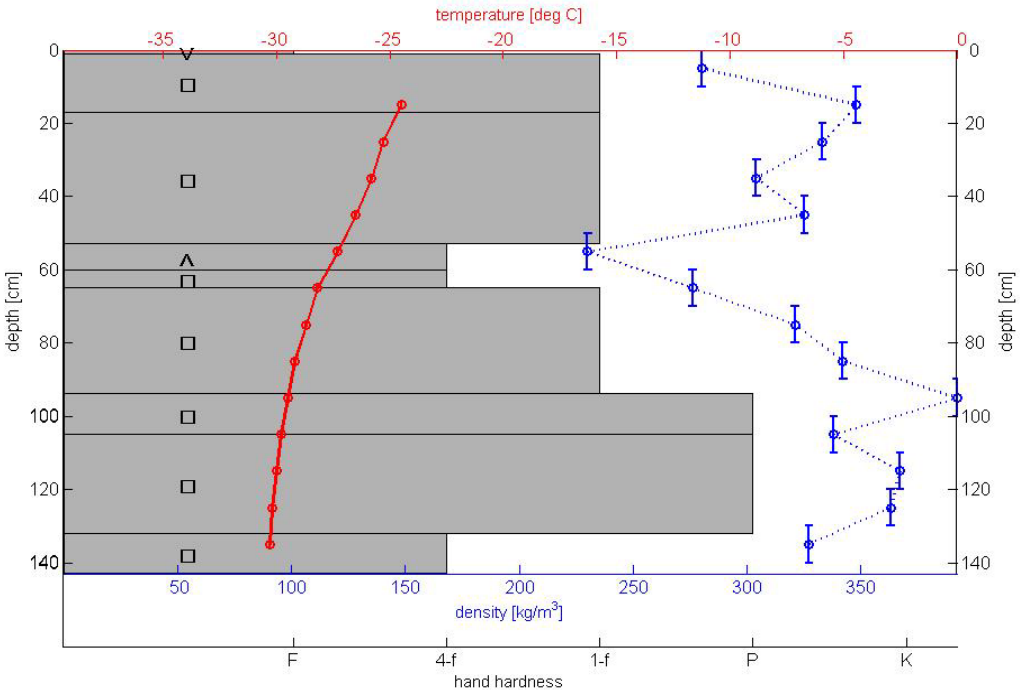

Figure B. 5 Snow pit stratigraphy for Summit 06-2.

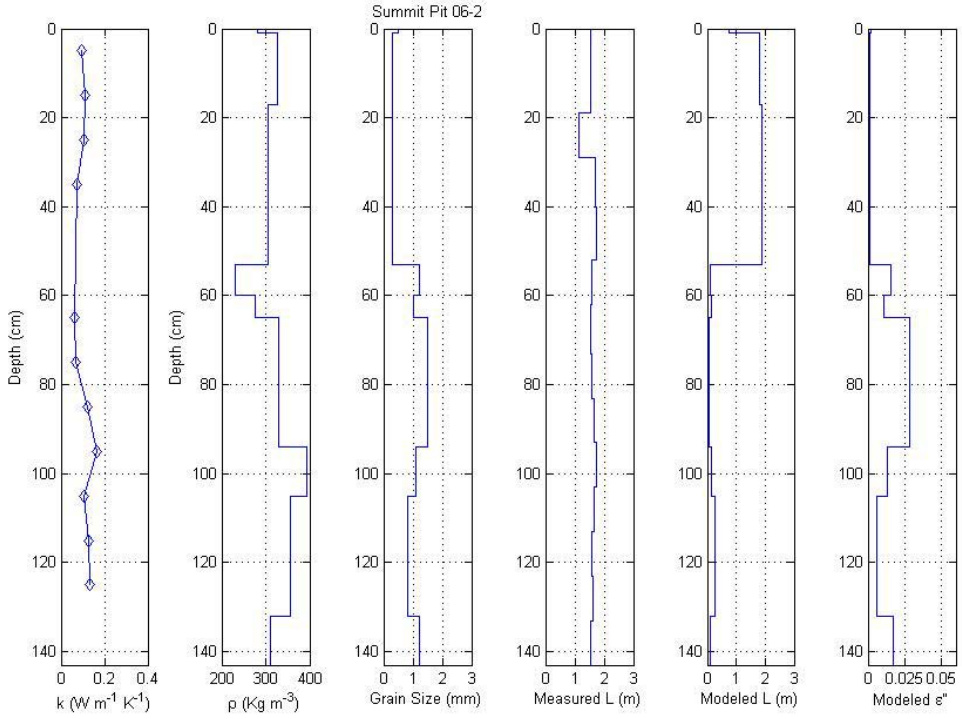

Figure B. 6 Thermal conductivity, density, grain size, measured extinction length, modeled extinction length and the imaginary part of the SFT modeled dielectric constant for Summit 06-2.

B.4 Summit Pit 06-3

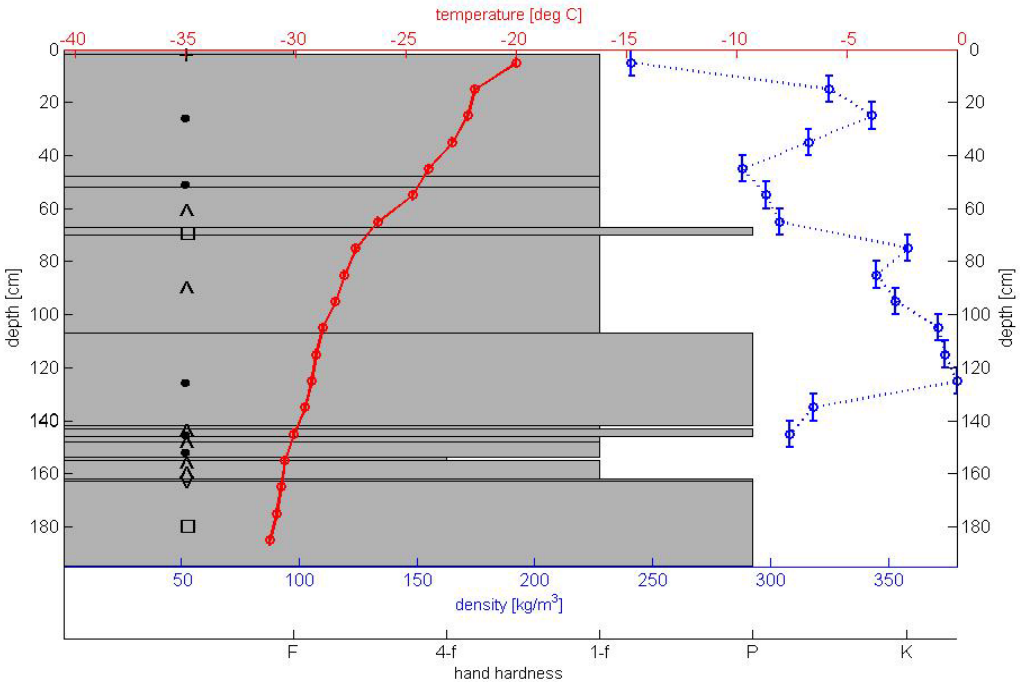

Figure B. 7 Snow pit stratigraphy for Summit 06-3.

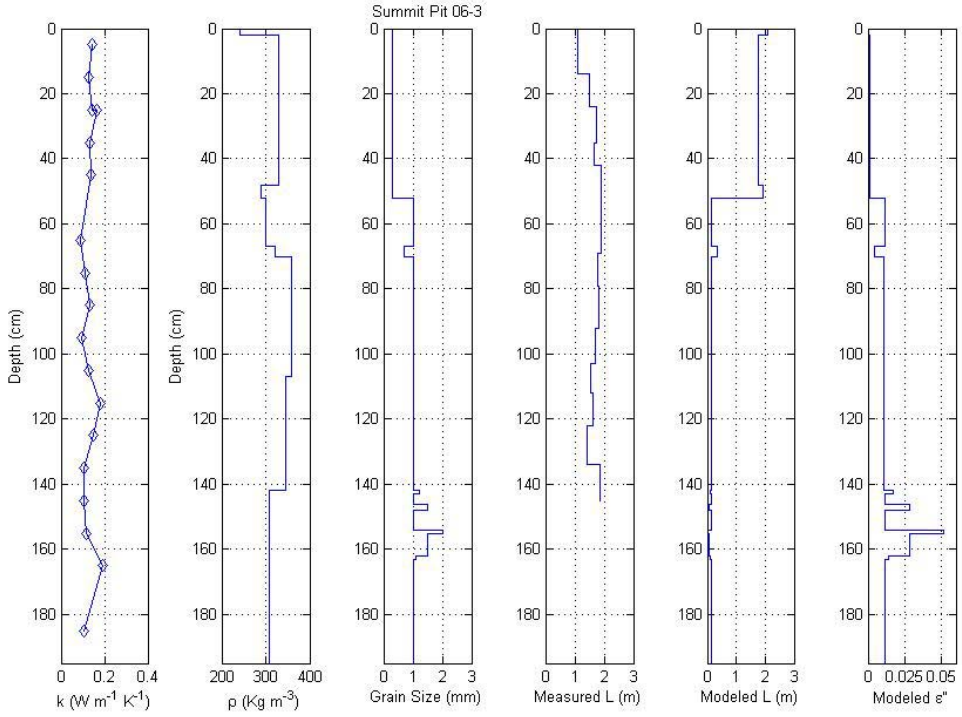

Figure B. 8 Thermal conductivity, density, grain size, measured extinction length, modeled extinction length and the imaginary part of the SFT modeled dielectric constant for Summit 06-3.

B.5 Summit Pit 06-4

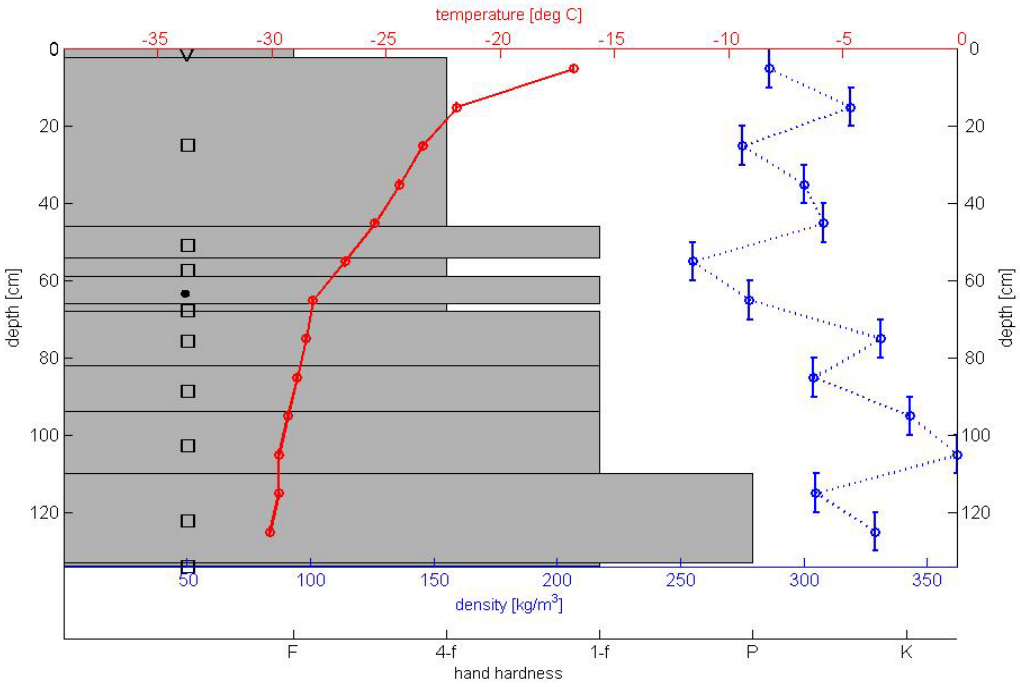

Figure B. 9 Snow pit stratigraphy for Summit 06-4.

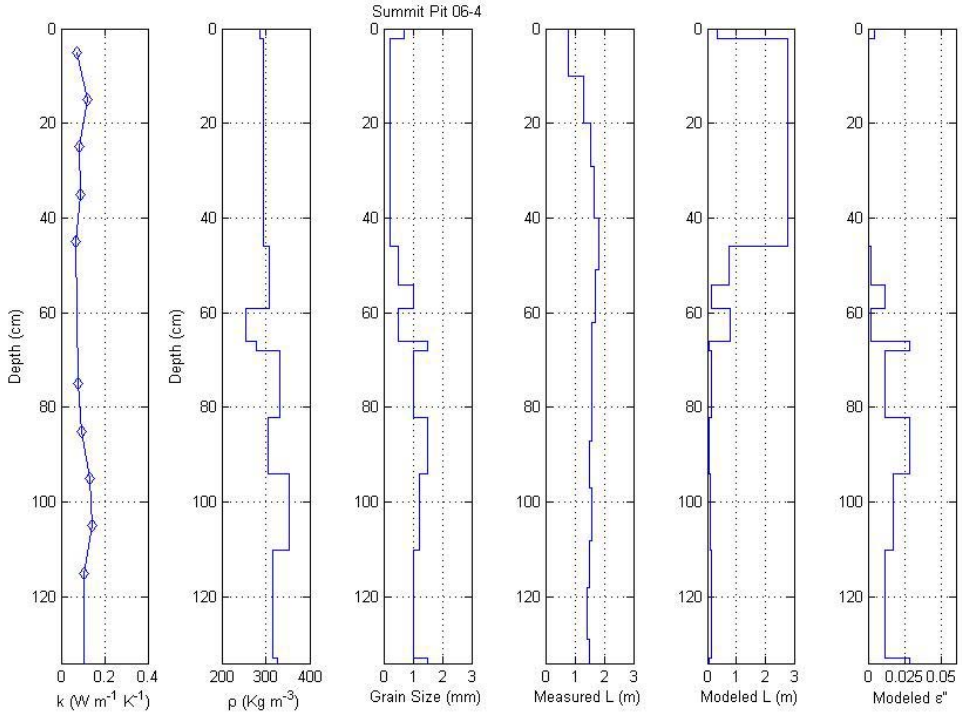

Figure B. 10 Thermal conductivity, density, grain size, measured extinction length, modeled extinction length and the imaginary part of the SFT modeled dielectric constant for Summit 06-4.

B.6 Summit Pit 06-5

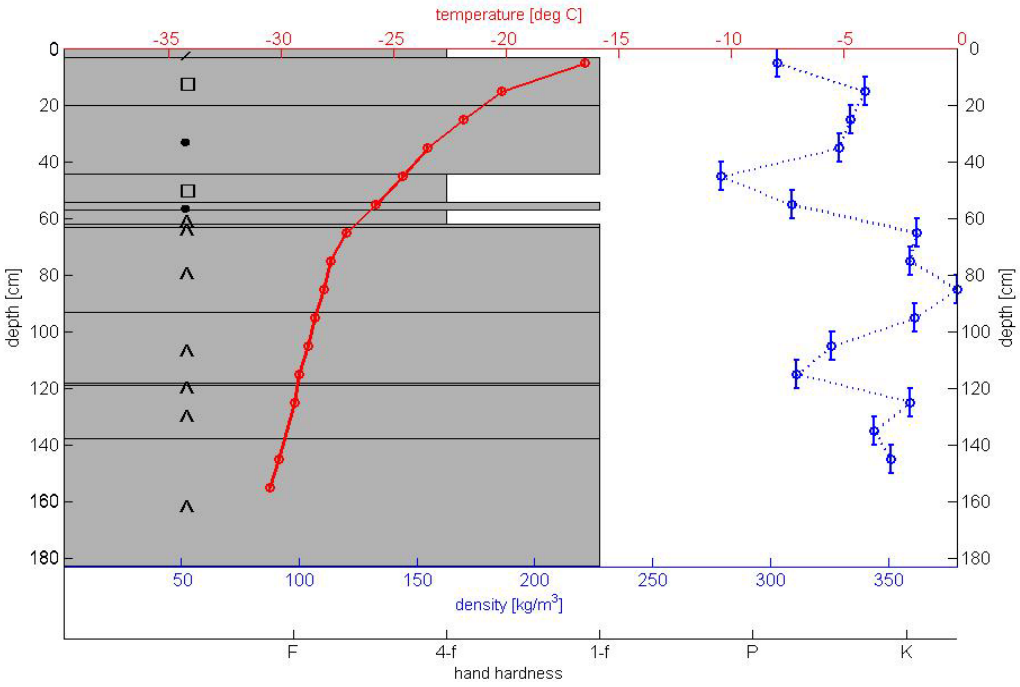

Figure B. 11 Snow pit stratigraphy for Summit 06-5.

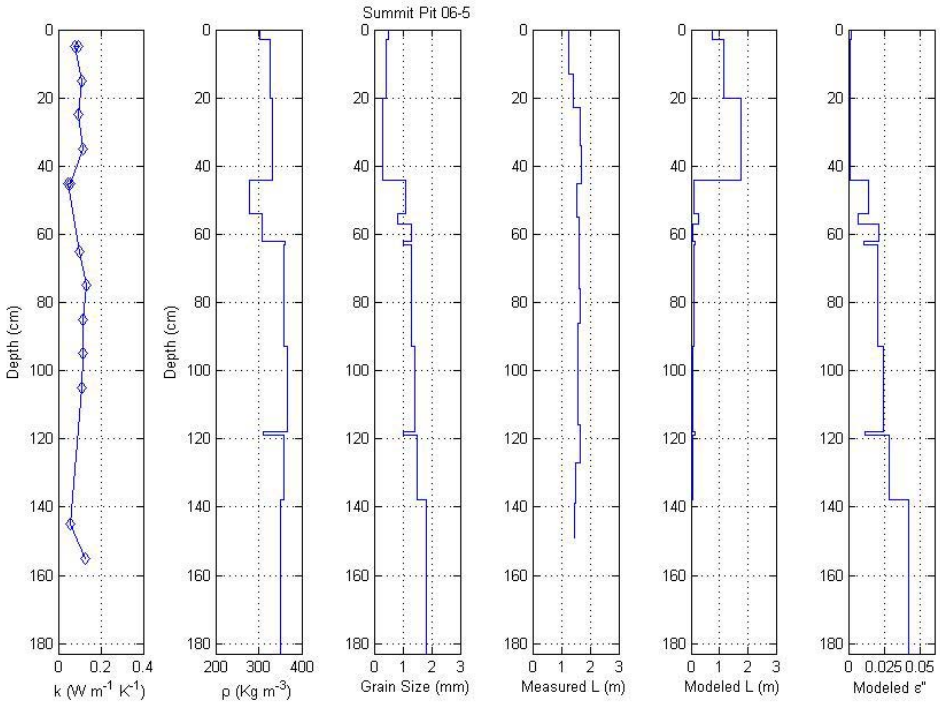

Figure B. 12 Thermal conductivity, density, grain size, measured extinction length, modeled extinction length and the imaginary part of the SFT modeled dielectric constant for Summit 06-5.

B.7 Summit Pit 07-1

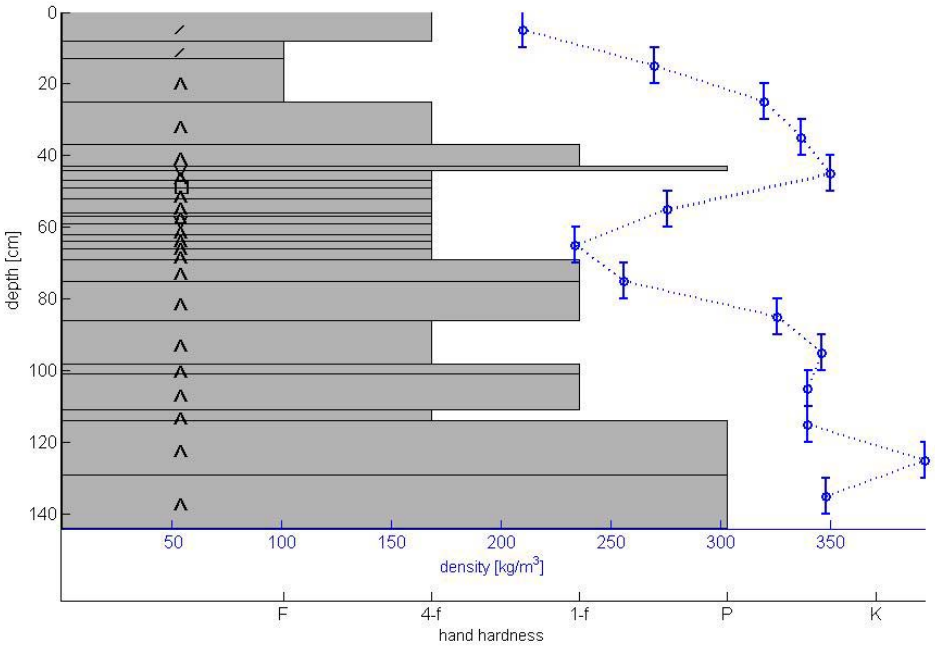

Figure B. 13 Snow pit stratigraphy for Summit 07-1.

B.8 Summit Pit 07-2

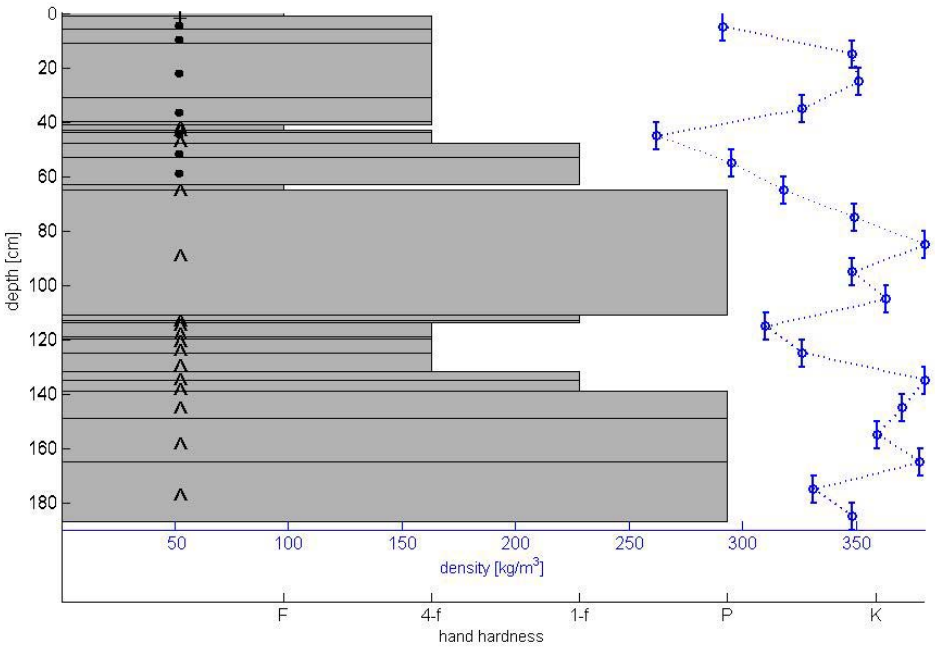

Figure B. 14 Snow pit stratigraphy for Summit 07-2.

Appendix C

INDIVIDUAL PIT DATA FROM ANTARCTICA

This appendix presents the field data collected at each pit conducted in Antarctica. The snow pit stratigraphy includes layer thickness, hand hardness, grain type, temperature and density. Each firn layers is represented by a rectangular box where the height of the box is the layer thickness and corresponds to the y-axis of the graph. The length of the box shows the hand hardness and corresponds to the bottom x-axis of the graph. The temperature profile is shown by the solid line and corresponds to the top axis of the graph. The density profile is shown by the dashed line and corresponds to the bottom axis of the graph. The grain type is defined using the international classification of seasonal snow and is given for each layer [Colbeck, et al., 1990]. The second figure compares the thermal conductivity, grain size, density, measured extinction length, the imaginary part of the complex dielectric constant and the modeled extinction length by pit depth. The exact location and date for each pit is given in Appendix A.

C.1 AP0601

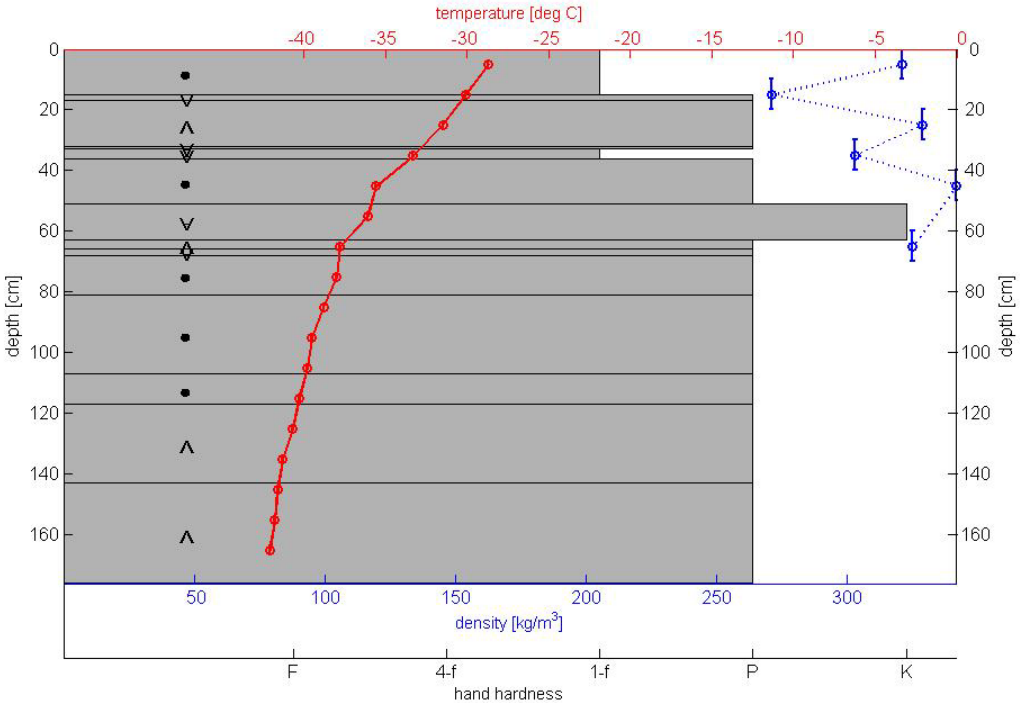

Figure C. 1 Snow pit stratigraphy for AP0601.

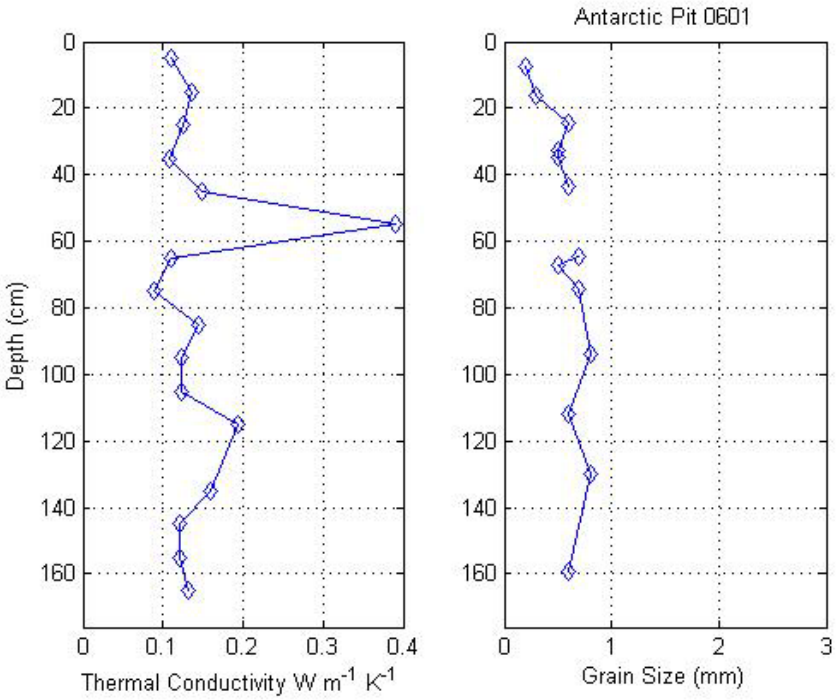

Figure C. 2 Thermal conductivity and grain size for AP0601.

C.1 AP0602

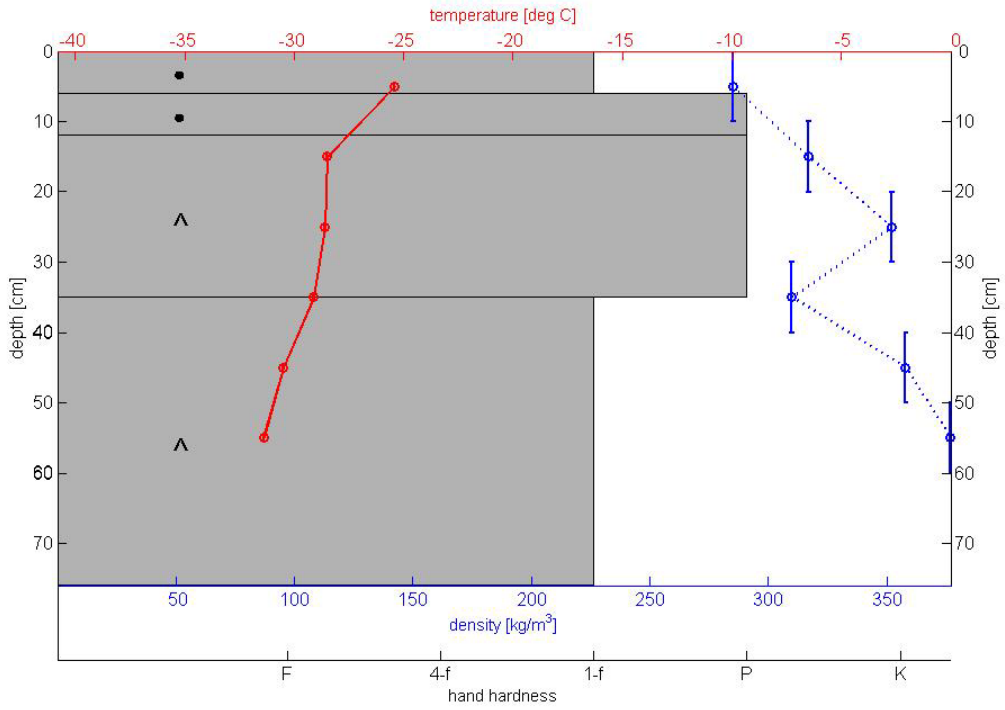

Figure C. 3 Snow pit stratigraphy for AP0602.

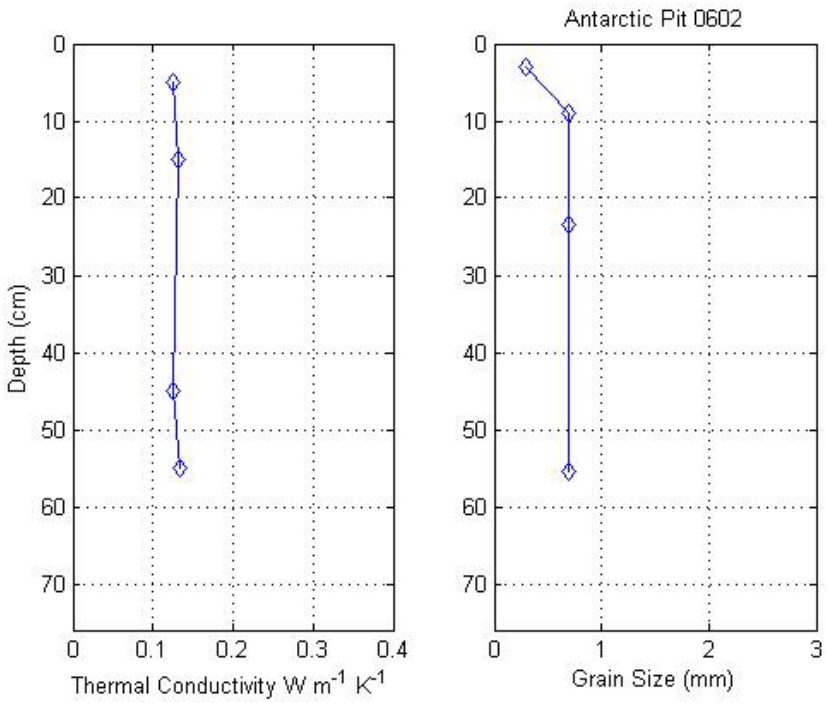

Figure C. 4 Thermal conductivity and grain size for AP0602.

C.1 AP0603

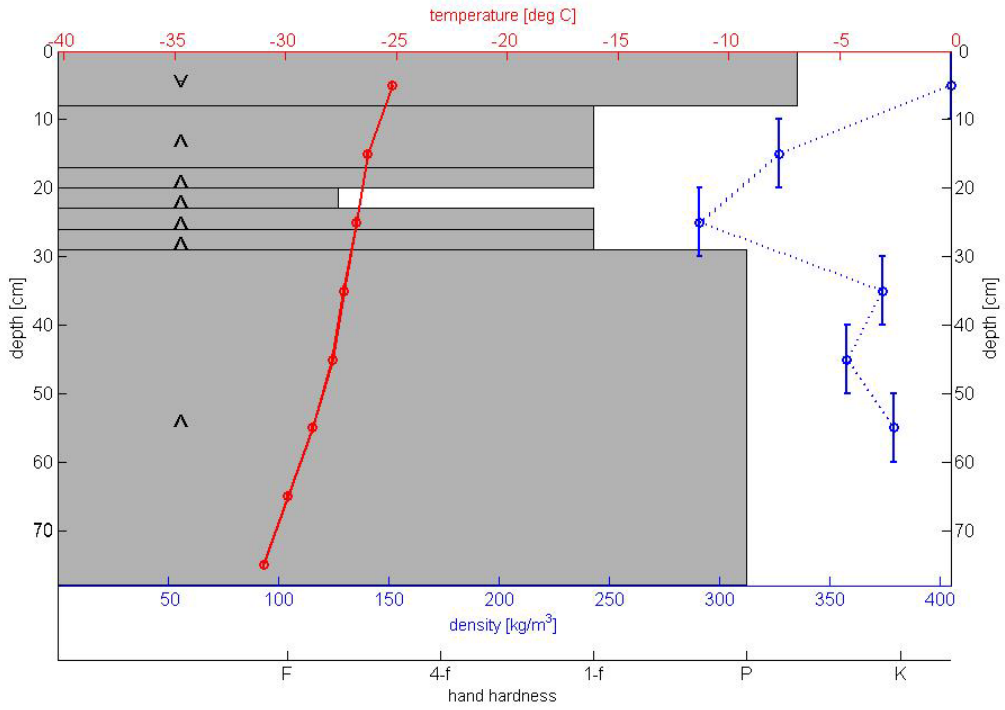

Figure C. 5 Snow pit stratigraphy for AP0603.

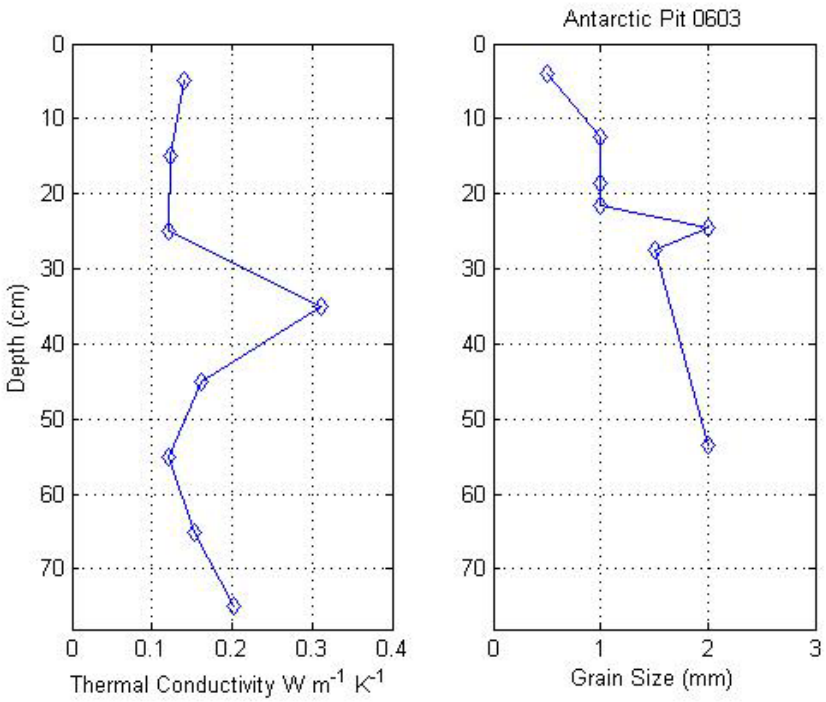

Figure C. 6 Thermal conductivity and grain size for AP0603.

C.1 AP0604

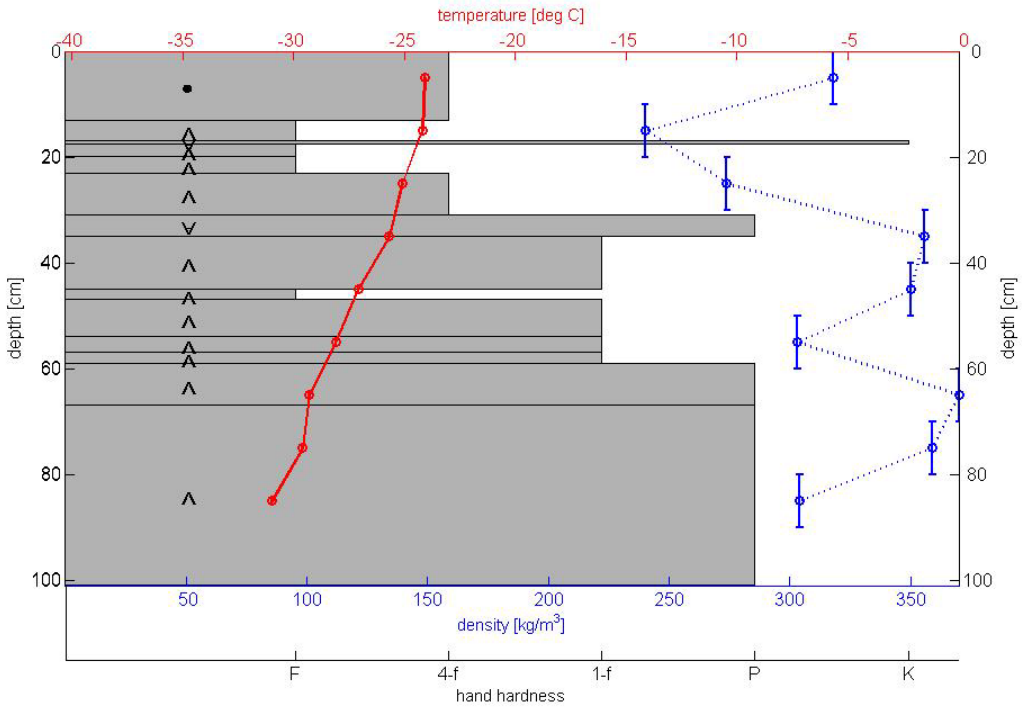

Figure C. 7 Snow pit stratigraphy for AP0604.

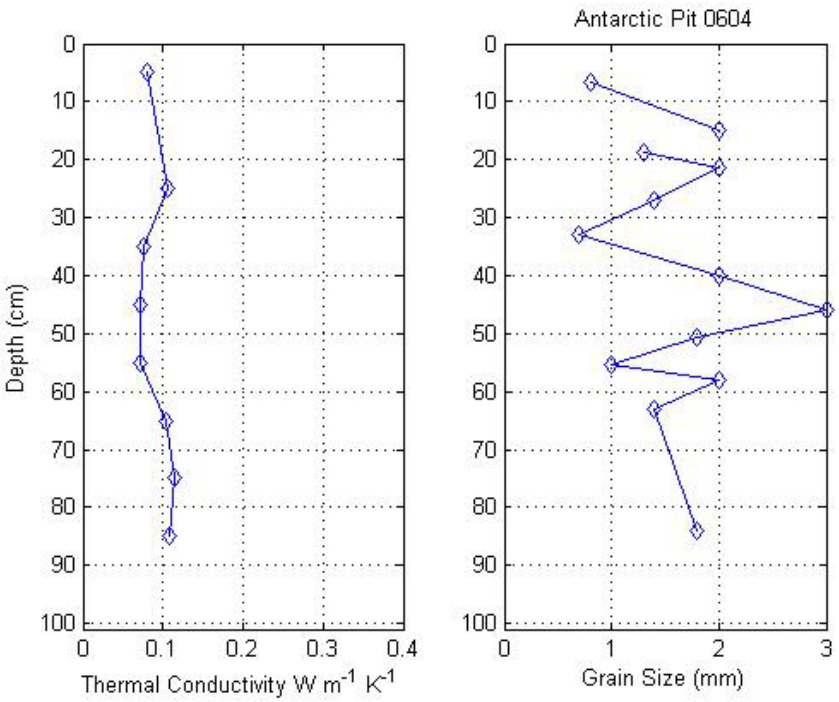

Figure C. 8 Thermal conductivity and grain size for AP0604.

VITA

LORA S. KOENIG

Education

Ph.D. Geophysics, University of Washington, 2008
Dissertation Title: *Firn Properties Relevant to Passive Microwave Remote Sensing*

M.S. Geography, University of Utah, 2002
Thesis Title: *The Evaluation and Development of Passive Microwave Snow Water Equivalent Algorithms in the Kuparuk River Watershed, Arctic Alaska, USA*

B.A. Mathematics, Linfield College, 1999

Publications

Koenig, L.S., E.J. Steig, D.P. Winebrenner and C.A. Shuman (2007), A link between microwave extinction length, firn thermal diffusivity and accumulation rate in West Antarctic. *Journal of Geophysical Research*, 112(F3), F03018.

Koenig, L.S. and R.R. Forster (2004), Evaluation of Passive Microwave Snow Water Equivalent Algorithms in the depth hoar dominated snowpack of the Kuparuk River Watershed, Alaska, USA. *Remote Sensing of Environment*, 93(4), 511-527.

Forster, R.R., K.C. Jezek, **L.S. Koenig**, E. Deeb (2003), Measurements of Glacier geophysical properties form InSAR wrapped phase. *IEEE Trans. Geosci. Remote Sensing*, 41(11), 2595-2604.

Conference Abstracts

Koenig, L.S, (2008) "Effects of Firn Microstructure on Passive Microwave Remote Sensing." *Workshop on the Microstructure and Properties of Firn*, Hanover, NH, March 10-11, 2008.

Koenig, L.S., T.C. Grenfell, D.P. Winebrenner, and E.J. Steig (2007) "Field-based Measurements of Microwave Extinction Length 37 GHz near Summit Greenland." *American Geophysical Union Conference*, San Francisco, CA, December 2007.

Koenig, L.S. (2006) "Field Measurements of Microwave Extinction Length." *Northwest Glaciology Meeting*, Fairbanks, AK, September 2006.

Koenig, L.S., E.J. Steig, and D.P. Winebrenner (2006) "Estimate of past Climate Information in Passive Microwave Emission." *Association of American Geographers Meeting*, Chicago, IL, March 2006.

Koenig, L.S., H. Conway, and H.P. Marshall (2005) "GISSNOSS Avalanche Model." Northwest Glaciology Meeting, Vancouver, B.C., October 2005.

Koenig, L.S. (2005) "Antarctic Accumulation: Passive Microwaves have Something to Say." NASA NAFP/JPFP/CIPA Symposium, San Jose, CA, July 2005

Koenig, L.S., E.J. Steig, and D.P. Winbrenner (2004) "Relationship of the Passive Microwave Characteristic Time Scale of Emission to Accumulation Rate in Antarctica." *American Geophysical Union Conference*, San Francisco, CA, December 2004.

Koenig, L.S., E.J. Steig, and D.P. Winbrenner (2004) "Using Passive Microwave Sensors to Determine Surface Temperature and Accumulation Rates." *Northwest Glaciology Meeting*, Seattle, WA, October 2004.

Koenig, L.S. (2002) "Determining Snow Water Equivalent using Passive Microwave Remote Sensing." *Utah Geographical Society Annual Conference*, Salt Lake City, UT, November 2002.